Mechanical etching of glass by powder blasting

DOI:

Document status and date:
Published: 01/01/1999

Document Version:
Publisher's PDF, also known as Version of Record (includes final page, issue and volume numbers)

Please check the document version of this publication:

Mechanical Etching of Glass by Powder Blasting

Peter Jan Slikkerveer
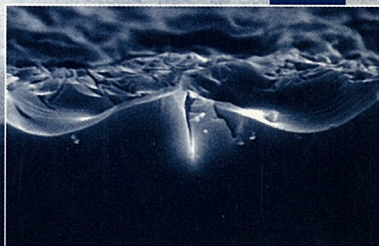
Mechanical etching of glass

by powder blasting

Mechanical etching of glass

by powder blasting

PROEFSCHRIFT

ter verkrijging van de graad van doctor
aan de Technische Universiteit Eindhoven,
op gezag van de Rector Magnificus, prof.dr. M. Rem,
voor een commissie aangewezen door het College voor Promoties
in het openbaar te verdedigen
op woensdag 27 oktober 1999 om 14.00 uur

door

Peter Jan Slikkerveer

geboren te Brielle

Dit proefschrift is goedgekeurd door de promotoren:

prof.dr. G. de With
en
prof.dr. J.E. Field

Aan mijn ouders

Samenvatting

Voor de massaproductie van een nieuw type vlak beeldscherm is er behoefte ontstaan aan een proces om nauwkeurig miljoenen gaatjes te maken in dunne glasplaten. Uit een inventarisatie blijkt poederstralen een veel belovend proces te zijn. Om de ontwikkeling van poederstralen tot een kwalitatief hoogwaardige etstechniek te ondersteunen, is onderzoek gestart naar de grondbeginselen van dit proces. Een gedeelte van de resultaten van het onderzoek is in dit proefschrift verzameld.

Allereerst richt de studie zich op het erosiemechanisme van brosse materialen wanneer ze uniform worden blootgesteld aan harde en hoekige deeltjes onder loodrechte inval. Vanuit de quasi-statische indentatietheorie worden kwantitatieve vergelijkingen afgeleid voor de erosiesnelheid, de ruwheid en de reductie in breuksterkte van het gestraalde substraat. De experimenten bevestigen de theorie dat de invloed van het poeder beperkt is tot haar kinetische energie.

Om de invloed van de deeltjesvorm te onderzoeken wordt de schade bestudeerd, veroorzaakt door de inslag van ronde deeltjes. Voor deze deeltjes bestaat naast het plastische inslagregime, zoals aanwezig bij scherpe deeltjes, een tweede – elastisch - regime met eigen scheurpatronen. Met de kwantitatieve vergelijkingen afgeleid voor de overgangen tussen de verschillende gebieden kan een erosiekaart worden geconstrueerd. Inslagexperimenten met individuele deeltjes tonen inderdaad de verschillende regimes, met de overgangen bij benadering op de voorspelde plaatsen. Voor het erosieproces zelf zijn de modellen minder succesvol. Geen van de modellen correleert met de experimentele resultaten. De oorzaak ligt waarschijnlijk in mechanismen die niet in de modellen zijn verwerkt, zoals de inslag van een rond deeltje op een ruw oppervlak en de interactie tussen een inslag en de al aanwezige schade in het substraat.

Bij scheve inval bevestigen experimenten de empirische "sin(θ)-regel", die erosie relateert aan de snelheidscomponent loodrecht op het substraat. Op basis van symmetrie-overwegingen wordt hiervoor een verklaring gegeven.

Voor patroonmatige erosie wordt het substraat lokaal bedekt met een erosie-bestendig masker. In dit poefschrift worden modellen opgesteld voor zowel de substraat-erosie als de maskerslijtage.

De patroonmatige erosie van glas laat zien dat de vorm van patronen hoofdzakelijk wordt bepaald door de hoekafhankelijkheid van erosie. Ondiepe structuren hebben in het midden een vlakke bodem waar de erosie vergelijkbaar is met die van homogene blootstelling van het substraat. Langs de maskerranden ontstaan invloedsgebieden met holle hellingen. De breedte van deze zones neemt lineair toe met de diepte van de structuur. In diepe structuren ontmoeten de hellingen elkaar wat leidt tot enigszins gepunte vormen. Vorm de verkregen vorm zijn in mindere mate van belang het afketsen van deeltjes op de steile hellingen, de geometrische hindering door de deeltjesgrootte en de maskerslijtage.

Als maskermaterialen blijken fotogevoelige polyurethaanrubbers zeer geschikt vanwege de hoge erosiebestendigheid en het gemak waarmee ze te patroneren zijn. Voor hun slijtagemechanisme, gebaseerd op vermoeiing, is in de literatuur geen constitutief model beschikbaar. Om maskerslijtage te bestuderen is het erosiegedrag van een drietal materialen bepaald en is met deze gegevens een erosiemodel voor maskerpatronen opgesteld. De resultaten laten zien dat zijwaartse slijtage van het masker de beperkende factor is voor de haalbare resolutie. De selectie van maskermaterialen zou daarom moeten gebeuren op basis van hun bestendigheid tegen erosie onder scherende inval.

Voor een poederstraalproces zijn grote hoeveelheden poeder nodig. Om een betaalbaar proces te verkrijgen, moet het poeder vele malen hergebruikt kunnen worden. Poederstraalexperimenten laten zien dat poederdegradatie kan worden beschreven met "survival of the fittest". Kraakexperimenten van individuele deeltjes bevestigen dit gedrag. Met röntgendiffractie is het mogelijk gebleken de oorzaak hiervan aan te tonen. Ongebruikte deeltjes blijken schade opgelopen te hebben tijdens hun productieproces. Bij de botsing met het glas breken ze op deze bestaande schade zonder dat de botsing nieuwe schade introduceert.

Tenslotte wordt de interactie tussen aankomende en terugkaatsende deeltjes onderzocht. Dit zogenaamde "flux effect" vermindert de effectiviteit van het erosieproces. Een studie met drie straalmonden van verschillende grootte resulteerde in een correlatie die kan worden gebruikt bij interpolatie tussen verschillende procesomstandigheden.

Al met al blijkt het poederstraalproces een waardevolle aanvulling te zijn voor de huidige abrasieve bewerkingsprocessen van brosse materialen.

Summary

Placed for the task of accurately making millions of holes in thin glass sheets in a process suitable for the mass production of a new kind of flat display, powder blasting was selected as the most promising process. To support the development of powder blasting into a high quality etching technique, the fundamental mechanisms behind the process were studied. Parts of the results from these studies are collected in the present work.

First the material removal mechanism is studied when brittle materials, like glass, are exposed homogeneously to streams of hard, sharp particles at normal impact. Based on quasi-static indentation theory, quantitative relations are derived for the rate of erosion, the surface roughness of the eroded substrate and its reduction in strength. Experiments confirm the theoretical findings that the influence of the erodent is limited to its kinetic energy.

To test the effect of particle shape, the solid particle impact of spherical particles is investigated. For these particles besides the plastic impact regime present for sharp particles, a second -elastic impact- regime exists with specific crack patterns. With quantitative equations derived for the transitions between the regimes, an erosion map is constructed. Verification experiments using single particle impact experiments show the presence of these different regimes with the location of the transitions roughly in the predicted position. The models derived for the erosion process (multiple impact) are less successful. None of the derived models correlate with the experimental results. Possible causes for this deviation are factors that are not incorporated in the theory like the impact of spherical particles on rough surfaces or interaction between particle impacts and the cracks already present in the substrate.

At oblique impact, experiments confirm the empirical "sin(θ)-rule", which relates erosion to the velocity component perpendicular to the substrate surface. An explanation based on symmetry considerations is presented.

To enable patterned erosion the substrate was covered locally with an erosion resistant mask. For this process, models are presented for both the erosion of the glass substrate and that of the mask itself.

The patterned erosion of the glass substrate shows that it is governed by its oblique impact behaviour. Shallow structures display a central zone with a flat bottom where the erosion corresponds with that of homogeneous (unmasked) erosion. Along the mask edges, zones of mask influence are found with concave slopes, the width of which grows linearly with the increasing depth. For deep structures the slopes meet giving a tipped geometry. Secondary effects on the obtained shape are the ricocheting of particles from the steep slopes, the geometrical hindering by particle size and mask wear.

Photosensitive polyurethane elastomers are suitable mask materials combining high erosion resistance and ease to pattern. For the fatigue based erosion mechanism currently no constitutive model is available in the literature suitable for assisting material selection. Therefore for three materials the erosion resistance was measured as a function of impact angle. From these data an erosion model for mask patterns was constructed. The results reveal the lateral erosion of mask patterns to be the limiting factor on mask resolution. To cover this, mask materials must be selected at their erosion resistance at glancing impact.

Since the erosion experiments revealed that large quantities of erodent material are needed, the abrasive powders must be reused many times to obtain an economical process. An experimental degradation study showed that a large part of the particle degradation follows the "survival of the fittest". Single particle crushing tests confirm this. With X-ray diffraction it has been possible to hint at the origin of the effect. Apparently, damage is still present from the manufacturing (crushing) process and impact on glass results in fracturing the particles at the flaws already present without introducing new.

Finally the particle interaction is studied between rebounding particles and impacting particles. This so-called flux effect decreases the efficiency of the erosion process. A study with three sizes of nozzles between 1.5 and 12 mm showed an universal fit that can be used for interpolation.

Reviewing the characteristics of the powder blasting process assembled in this thesis shows the powder-blasting process to be a worthy addition to the abrasive processes for brittle materials currently available.

Table of Contents

1 Introduction

1.1 Problem setting

Within fifty years the television (TV) has developed into an important consumer electronics product. In that time the TV-image changed from black and white to colour, the picture quality improved considerably while the size increased. The display principle, however, remained that of the cathode ray tube (CRT) making the displays, especially the larger ones, bulky and heavy.

Many research efforts have been directed towards finding light-weight, flat and thin displays [for a review see e.g. 1]. Only some types of liquid crystal displays (LCD's) have found a solid position in the market for smaller displays in e.g. calculators and notebook personal computers. In the television segment no type of displays has met the price/performance ratio of the CRT. One of the main reasons for this is found in the advantages of the display principle of a CRT. This principle, based on the excitation of phosphors with high energetic electrons, does not have any viewing-angle effect like the LCD displays and produces a high contrast and efficacy.

To use these advantages several flat and thin display concepts have been investigated based on the CRT principle, see e.g. [2] and [3]. Although these displays were flat and relatively shallow, they still were very heavy since they all

require thick front-plates to bear the vacuum stresses. It was experienced that the only way to solve this dilemma was to use a system of internal vacuum supports. These vacuum supports, however, will hinder the electron transport. The insight that the supports could also be actively used for the transport of electrons to the screen laid the foundation of a new type of display, the Zeus display [4, 5]. The issues arising from the fabrication of this display motivated the work presented here.

To put the work in perspective, section 1.2 will first summarise the display principle of the Zeus display. It will introduce the technological problem to produce important parts of the display for which the powder blasting process finally has been selected. The powder blasting process itself is introduced in section 1.3. Here the process knowledge at the start of the project is summarised and the driving questions are derived for the research presented in this thesis. Finally, section 1.4 outlines the structure of the thesis to meet these questions.

1.2 The Zeus display

Although the way the picture is generated is similar for a CRT and a ZEUS display, their structures are very different, as is shown in Figure 1-1, reflecting the distinctive way the electrons are transported to the screen. In both displays electrons are generated at a thermal cathode and transported to a screen covered with phosphors. The electrons, being accelerated by the presence of an electrostatic field during transport, excite the phosphors that emit visible light during decay.

The method of transport of the electrons differs between the two types of displays and so does the method of selection of the different phosphor dots on the screen. In a CRT the beam of electrons is directly attracted towards the screen by the electrostatic field between cathode and screen. During its travel the beam is deflected periodically by an additional electromagnetic field to scan the full screen. For each of the three colours therefore one electron beam is needed.

In the Zeus display the electrons are inserted into vertical canals positioned behind the screen. Since the size of the canals is limited, the electrons will soon hit the wall of the canal. When the wall is coated with a material with a high secondary electron emission coefficient for each electron hitting the wall a secondary electron is emitted. By applying an electric potential difference over the length of the canal the electrons will then start hopping along the canal walls.

The selection of the phosphor dots is obtained by using a perforated sheet at the screen side of the canals with electrodes around each hole. Negatively charged these electrodes force the electrons to hop along the backside of the canal, while

positively charged they will extract the electrons from the canal and lead them to the screen. In the last step to the screen the electrons are accelerated to the energy they need for excitation of the phosphors.
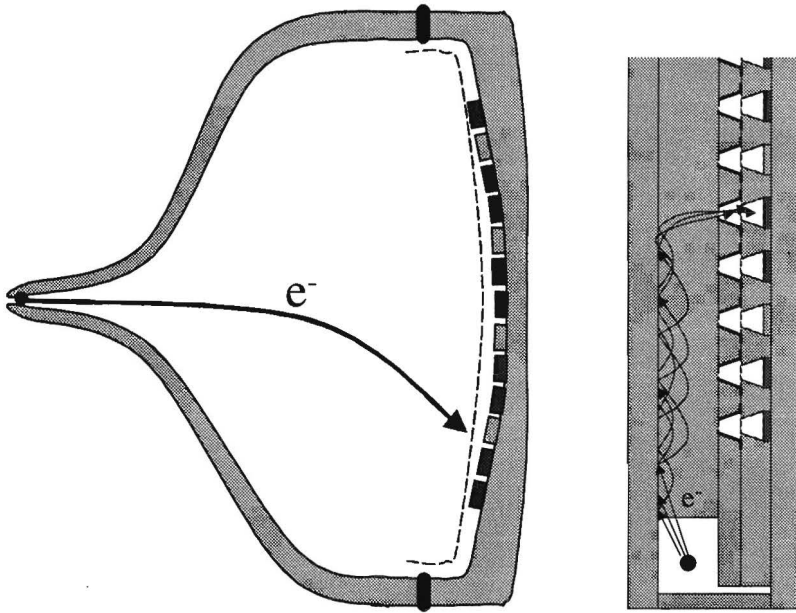
Figure 1-1: A comparison of the cathode ray tube (CRT, left) and the Zeus display (right).

Although the structure of the Zeus display sketched in Figure 1-1 is highly simplified, it already contains two perforated plates, each having three holes per pixel (one for each colour). In the actual Zeus display four to six perforated plates were used, partly to overcome weaknesses in the simplified design (see [6]) and partly to use the potency of the Zeus display of multiplexing the pixel addressing, which reduces the amount of electronic drivers considerably.

The fabrication of these perforated plates has been one of the major issues in the Zeus project. To enable mass production of the display a technique was needed that is able to produce these plates at low cost and at high accuracy.

The material itself must be dielectric, cheap, resistant to electrons, applicable in vacuum and preferably of the same material as the vacuum proof envelope of the display. It must be patterned with up to 1.000.000 holes per plate with a size down to 150 μm in size and at a high positional accuracy. Since the displays needs a stack of plates were the holes should be on top of each other over the full surface of the display, the position of the holes should be accurate to within 50 μm, even for

displays with a meter in diagonal. The method of production must be fast, cheap and upscalable to millions of displays per year.

Directed by its availability for LCD's, finally borosilicate glass was selected as the material for both the envelope and the perforated plates. For the structuring of the 420 μm thick glass sheets several processes were considered. The high geometrical specifications ruled out processes using high temperatures like hot pressing and laser drilling, while the desired process speed eliminated "slow" processes like ultrasonic drilling and chemical etching. The process comparison showed mechanical etching by powder blasting to be the most promising process. The identification of the process fundamentals has been the motivation of the research presented in this thesis.

1.3 The powder blast process

Sand blasting is an old technique for removing paint and corrosion from surfaces and for decorating glass doors or barbershop mirrors. In the last application the areas of the glass surface eroded by the abrasive particles give a scattering effect nicely contrasting the transparent properties of the glass or mirror itself. The process needed for the production the perforated glass sheets, compares closely with this decorative use of powder blasting. As for any etching process it contains three basic process steps: The application of the mask, the actual powder blasting of the masked substrate and the removal of the mask afterwards. In Figure 1-2 the process flow is sketched.
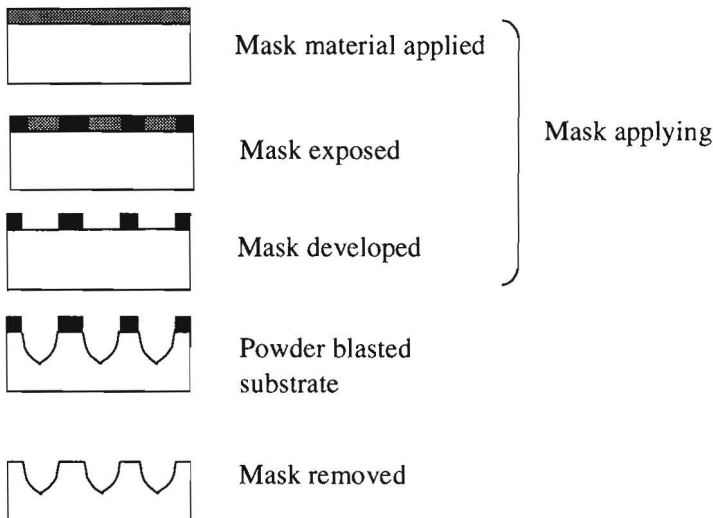
Figure 1-2: Schematic process flow of the mechanical etching process by powder blasting.

Application of a mask

To protect the areas of the surface that should not be etched by the abrasive particles a mask material is needed that is considerably more resistant to erosion than the glass. For certain larger structures metal masks can be used. Since thin metal masks tend to deform plastically by the impacts of the particles, metal masks should have a considerable thickness. For finer structures a photo-patternable rubber mask is the best choice. Here the masking material is applied in a continuous layer for example by laminating after which the layer is exposed through a mask by an UV source. In the exposed areas the rubber crosslinks, while the material in the unexposed areas can be removed in the development step. This technique has the great advantage that the pattern is actually transferred to the glass in the exposure step. Since the compliant mask is attached to the glass it will follow its deformation induced, for example by thermal effects during powder blasting, meanwhile accurately exposing the same areas of the glass surface.

Powder blasting

In the actual powder-blasting step the complete substrate surface is exposed to a high-velocity stream of hard, angular abrasive particles (see Figure 1-3). With the mask protecting part of the surface only the desired parts of the surface are eroded. The size of the particle beam is not related to the size of the structures to be etched and is usually considerably larger. As sketched in Figure 1-3 one or more abrasive jets scan across the substrate surface with the intention to cover the surface homogeneously with abrasive particles. The powder-blasting machine in this process is thus only used for distributing powder homogeneously over a wide surface at a constant velocity and constant flow rate.
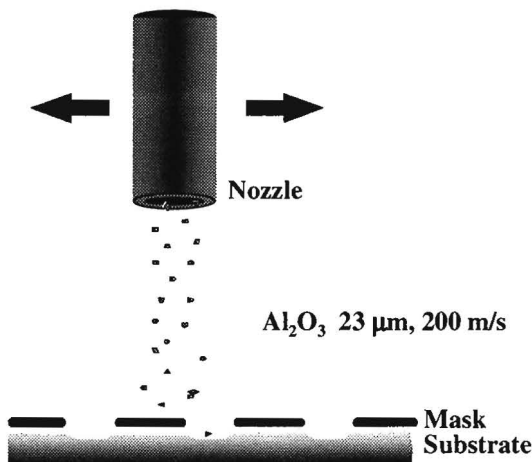
Figure 1-3: The principle of powder blasting etching.

After powder blasting the substrates are cleaned and the mask is stripped. The masks are usually removed chemically.

Although the process has been in use for many years, the decorative application did not need fundamental understanding. The erosion mechanism that is at the basis of the powder blasting process, namely solid particle erosion, has been studied scientifically primarily as the unappreciated phenomenon damaging aircraft and rocket parts [7]. Since this effort was primarily directed towards preventing erosion, little was known about the implications of using solid particle erosion as a high accuracy mass-production process. To assess the implications three main questions had to be answered:

1. What are the parameters controlling the process (e.g. the processing speed and reproducibility) and its results (e.g. the surface structure and the shape of the patterns)?
2. What are the essential process costs and what can be done to decrease those (e.g. machine, abrasive)?
3. What scaling rules for the process should be used when upscaling from a small laboratory set-up to full mass production?
   The work presented in this thesis has been directed towards finding the answers to those questions.

1.4 Outline

The investigation of the powder blasting process starts with a study of the fundamental event where a hard, angular abrasive particle hits the glass substrate in chapter 2. Starting from quasi-static indentation theory already available, the study derives relations for the rate of material removal, the resulting surface roughness and the substrate strength reduction in the case of erosion of flat (unmasked) substrates at normal impact. Experiments compare well with the theoretical relations, confirming the scaling rules obtained.

To study the influence of particle shape on the erosion process, in chapter 3 the focus is directed on the erosion by spherical particles. Since hard spherical particles permit extra erosion regimes, they are also of fundamental interest. Using the approach that was successfully applied to sharp particles, this section derives theoretical relations for the transitions between the different erosion regimes building so-called erosion maps. It also derives relations for the rate of material removal and the resulting surface roughness. The derived erosion maps and models are tested experimentally.

Since in masked erosion not all particles will hit the surface perpendicularly even when the abrasive jet is directed at right angles to the substrate surface, in chapter 4 the erosion at oblique impact is studied. Experimentally the simple correlation found in the literature is verified for the materials used in this study and a qualitative explanation is given for the background of the correlation.

Using the description of the erosion process derived in the previous chapters, in chapter 5 a mathematical model for patterned erosion is obtained. The basic mechanisms described by the model are confirmed by experimental results. They show the shape of the structures to be almost independent of process conditions and give simple scaling rules for the shape.

Because no material is completely insensitive for solid particle erosion, chapter 6 focuses on the wear of photosensitive rubbers that can be used as masking material for powder blasting. It demonstrates that the erosion behaviour of these materials is considerably more complex than that of brittle materials like glass. The chapter derives a model for the erosion of mask structures. This model shows the importance of differences in the erosion behaviour of different materials at oblique impact for the erosion resistance of the mask. Experiments confirm the model results of the model.

For the erosive etching of material, large quantities of erodent particles are needed. To obtain a cost efficient process it is necessary to reuse the abrasives several times. For this, the powders should not degrade significantly. In chapter 7, the degradation behaviour is investigated, displayed by the alumina abrasives used in this work trying to identify the cause for this specific behaviour.

For the step from laboratory to large-scale production machines, it is important to account for the influence of the powder being removed from the abrasive jet after impact. Since it shields the surface from incoming particles, the rebounding powder can reduce the material removal rate dramatically. This so-called flux effect is studied in chapter 8 to find a scaling rule that can be used for upscaling.

Finally chapter 9 summarises the conclusions of the separate sections and answers the technological questions raised in section 1.3. It concludes with a reflection on the future for powder blasting as an etching process for brittle materials.

1.5 Literature

1   L.E. Tannas Jr, *Flat panel displays and CRT's*, Van Nostrand Reinhold, New York (1985).

2   A.W. Woodhead, D. Washington, D.L. Lamport, A.G. Knapp, J.R. Mansell and K.G. Freeman, *The channel multiplier cathode ray tube*, Philips J. Res. 41 (1986) 325-342.

3   H.J. Ligthart, G.G.P. van Gorkom and A.M.E. Hoeberechts, *A flat CRT based on an array of p-n emitters,* Optoelectronics-Devices and Technologies 7 (1992) 163-178.

4   G.G.P. van Gorkom, T.S. Baller, B.H.W. Hendriks, N. Lambert, H.J. Ligthart, E.A. Montie, G.E. Thomas, P.H.F. Trompenaars, S.T. de Zwart, *Flat thin CRT based on controlled electron transport through insulated surfaces*, Appl. Surf. Sci., 111 (1979) 276-284.

5   M.H. Vincken (ed), *Special Issue on a new flat thin display technology*, Philips J. Res. 50 no 3-4 (1996).

6   G.G.P. van Gorkom, *Introduction to Zeus Displays*, Philips J. Res. 50 no 3-4 (1996) 269-280.

7   I.M. Hutchings, *Tribology,* Section 6.4, Edward Arnold, London (1992).

2 Erosion and damage by sharp particles[*]

Solid particle impact is fundamental to the erosion process of brittle materials. Hard angular particles hit a surface at a considerable speed provoking deformation and damage in the target material. The induced micro-cracks may remove chips of material, which is the intended effect in powder blasting.

From the single particle event this chapter derives quantitative relations for the erosion rate of the powder blast process. Models are also derived for the resulting surface roughness and strength reduction of eroded surfaces by the inflicted damage. The model reveals that the kinetic energy of the particles acts as a global scaling parameter for the erosion process.

The theoretical findings are verified by an extensive series of experiments where erosion rate, surface roughness and strength reduction are measured for borosilicate glass at a wide variety of erosion conditions, i.e. particle sizes and impact velocities.

2.1 Introduction

Solid particle erosion is mainly of interest in two types of fields. It is an unwanted phenomenon in aeronautical engineering and in the hydro-pneumatical transport of particles where the erosion results in wear and damage of the structure. It is, however, also used for decoration of window glass and mirrors, where the damage generates an optical effect on the glass surface. In a new development the latter method is extended for generating technical patterns such as holes and canals in brittle substrates. In this area well controllable solid particle erosion is a desired phenomenon.

In both types of fields there is a need for a thorough understanding of the mechanisms behind solid particle erosion. Several models were published describing the proportionality between erosion rate, substrate material parameters like hardness and process conditions like particle size and velocity [e.g. 1, 2, 3, 4]. Most models are based on the analogy between solid particle impact and indentation, using the indentation theory of Marshall, Lawn and Evans [5, 6, 7] for hard angular particles. For brittle materials, Hutchings [8] drew so-called erosion maps based on the same theory, enabling easy categorisation of erosion processes.

This paper studies the potential of the models to assist the industrialisation of solid particle erosion of brittle materials by hard angular particles. This is done by reworking the modelling based on the indentation theory of Marshall, Lawn and Evans, quantifying the models derived earlier. In this procedure we focus on the important parameters for industrialisation: erosion rate, resulting surface roughness and surface damage (strength reduction).
After describing the experimental procedures we show the results of validation experiments of this theory showing the applicability of the models. We conclude with a discussion on the validity of the quantified models.

2.2 Indentation modelling of Marshall, Lawn and Evans

2.2.1 Fundamental aspects

Beneath a sharp indenter the high principle stress differences lead to plastic deformation of the brittle substrate. The indentation hardness (H) is defined here as the ratio between indenter force (P) and projected surface of the indentation (A_{ind}) [9].

$$H = \frac{P}{A_{\text{ind}}} \tag{2.1}$$

In the theory following, the indentation hardness is taken to be a constant.

An increase in indentation force leads to a growth of the plastic zone. At larger indentation loads, radial/median cracks and lateral cracks are formed (Figure 2-1, see [9]).
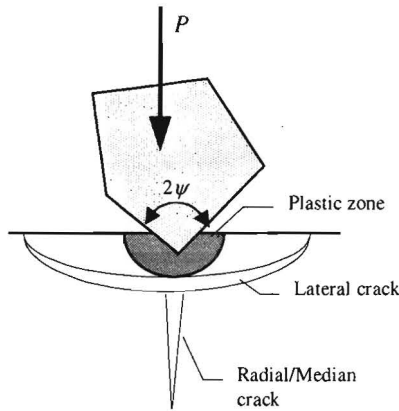
Figure 2-1: A schematic representation of the crack patterns obtained with a sharp indenter.

The development of the crack systems was modelled by Marshall, Lawn and Evans [5, 6, 7 and 10] using, what they called, the theory of "well-developed plasticity". They assumed that the stress field around an indenter tip depends only locally on its shape, so the shape dependence does not extend beyond the plastic zone. Since the stress at the outside border of the plastic zone is assumed to be equal to the materials hardness, the stress field outside the plastic zone is governed by the size of that zone.
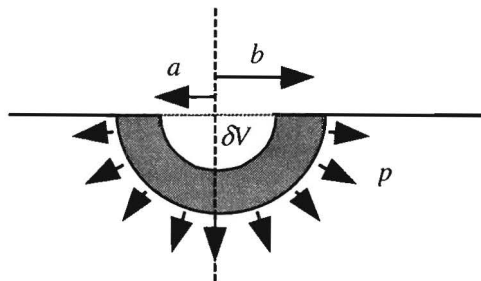
Figure 2-2: The simplification of the indented volume as is used in the inflated-hole theory.

Chiang et al. [10] show that the global stress field around an indenter is determined by the indentation volume (δV, see Figure 2-2), which is the volume the indenter

penetrated into the substrate. Since the shape of the indented volume is not important for the stress field outside the plastic zone, the models for the crack systems of Marshall et al. suppose the indented volume to be hemispherical. Hill's inflated hole theory (e.g. [11]) now gives a relation between the indent size and the size of the plastic zone. This implicit relation is usually approximated by a power law according to

$$\frac{b}{a'} \cong \mu \left(\frac{E}{H} \right)^m . \tag{2.2}$$

In this equation the parameters μ and m are fitted constants. E is the Young's modulus of the substrate while b and a' are respectively the radius of the plastic zone and that of the indented volume ($\delta V = 2\pi/3a'^3$). The value 0.5 of the exponent m is commonly used in the literature. Although appendix A shows this value gives only a moderate fit, we will use $m = 0.5$ since we will later make use of fit data of crack lengths obtained in this way. The value of μ obtained by fitting equation 2.2 to Hill's equation is 0.63 (see Appendix A).

In the stress field originating from the radial stresses (p, see Figure 2-2) lateral and radial/median crack patterns are formed. For the calculation of crack size, Marshall et al. use the theory of penny-shaped cracks. In this they consider the crack opening force to be a point load, which is only a good approximation for well-developed cracks (for longer crack sizes).

2.2.2 Crack lengths

Radial cracks

Marshall [7] finds the equilibrium crack length for radial/median cracks (c_{rad}), satisfying the following relation

$$c_{rad} = \beta^{2/3} E^{1/3} H^{1/3} \frac{\delta V^{4/9}}{K_{Ic}^{2/3}} \tag{2.3}$$

with δV the indentation volume, K_{Ic} the fracture toughness of the substrate and E and H its Young's modulus and hardness, respectively. The parameter β is, according to Marshall, "a dimensionless constant independent of material properties and indenter shape (within the limit set by the requirement for a hemispherical plastic zone)". Since this limit is the basis of the theory we assume it to be so. This means that we can use the value of $\beta = 0.096$, Marshall calculated from fits of crack lengths measured by Anstis et al. [12] covering a wide range of materials.

Lateral cracks

Marshall et al. [5] derive a relation for the crack length of the lateral cracks for sharp indenters. This relation contains two parameters ζ_0 and ζ_L which are fitted on experiments with Vickers indenters to $\zeta_0 = 1.2 \cdot 10^3$ and $\zeta_L = 25 \cdot 10^{-3}$, respectively.

The equations obtained by Marshall et al. can be rewritten into ones containing the indentation volume δV by substituting the indentation force (P) by its representation in indentation volume for sharp indenters

$$P = \left(3 \frac{\delta V}{\cot \psi} \right)^{2/3} \alpha^{1/3} H \tag{2.4}$$

with α the shape factor of the indenter (2 for Vickers) and 2ψ the top angle of the indenter (see Figure 2-1). The crack length relation now changes to one expressed in terms of the indentation volume

$$c_{lat} = c_{lat}^L \sqrt{1 - B} \tag{2.5}$$

with

$$c_{lat}^L = 3^{5/12} \frac{\alpha^{5/24} \sqrt{\zeta_L}}{A^{1/4}} \frac{E^{3/8} H^{1/8} \delta V^{5/12}}{\sqrt{K_{Ic}}} \tag{2.6}$$

and

$$B = \frac{1}{3^{1/6}} \frac{\zeta_0^{1/4}}{\alpha^{1/12} \sqrt{A}} \frac{E^{1/4} K_{Ic}}{H^{5/4} \delta V^{1/6}} \tag{2.7}$$

where the factor A describes the shape of the chip of material above the lateral crack. Marshall et al. [5] concluded that the quarter plate model was the most appropriate giving $A = 0.75$. The coefficients c_{lat} and B can be interpreted as the crack size for long cracks and an "apparent threshold" for lateral cracks ($B = 1$).

Note that along with the indentation force, the top angle of the indenter (ψ) has disappeared from the relations 2.5 to 2.7, demonstrating that the deformation pattern is completely governed by the indentation volume δV. The theory, however, remains correlated with Vickers indentations by for example the crack pattern assumed in the quarter plate model.

2.2.3   Transitions

The large difference in the principal stresses beneath the indenter tip always gives rise to a zone of plastic deformation with predominant compressive stress. At higher loads, the tensile stresses around the plastic zone will exceed the fracture

limit and cracks will start occurring. The initiation of these cracks can be expressed in a threshold value of the indentation volume (δV).

A quantitative estimate of the threshold can be made by equalling the crack length to the size of the plastic zone (b). This estimate might be interpreted physically as the point where the crack becomes visible outside the plastic zone. Although this is not a fracture-mechanical threshold and the crack size equations are only valid for larger cracks, it is indicative of the position of the transition.

The crack threshold for the radial/median cracks results in

$$\delta V = \left(\frac{3}{2\pi}\right)^3 \frac{\mu^6}{\beta^6} \frac{E^{3/2} K_{Ic}^6}{H^{15/2}} \tag{2.8}$$

and for the lateral cracks in

$$\delta V = \frac{1}{2^6 3} \frac{\left(2\zeta_0^{1/4}\alpha^{1/3}\zeta_L\pi^{2/3} + 2^{1/3}\mu^2 A\right)^6}{A^3\alpha^{5/2}\zeta_L^6\pi^4} \frac{E^{3/2} K_{Ic}^6}{H^{15/2}}. \tag{2.9}$$

For lateral cracks another threshold relation originates from the "apparent threshold" ($B = 1$ in equation 2.5)

$$\delta V = \frac{1}{3} \frac{\zeta_0^{3/2}}{\alpha^{1/2} A^3} \frac{E^{3/2} K_{Ic}^6}{H^{15/2}} \tag{2.10}$$

Note that all threshold equations have the same dependence on substrate parameters, giving a schematic threshold equation

$$\delta V = C \frac{E^{3/2} K_{Ic}^6}{H^{15/2}} \tag{2.11}$$

where the value of the constant C depends on the origin of the threshold.
Please note that the threshold criteria are not based on a fracture mechanical principle but were chosen pragmatically. The fracture mechanical values are, however, comparable as the threshold value for median cracks (P^*, [13] and [14]) shows in paragraph 2.3.2.

2.3 Particle impact

2.3.1 Towards particle impact

The theory of quasi-static indentation can be used for solid particle impact. Although impact speeds of some hundreds of meters per second do not seem quasi-

static, they still are, since they are much smaller than the velocity of elastic and plastic waves of deformation in brittle materials. As a guideline for quasi-static impact the deformation waves should be able to travel several times through the deformed area during the contact time of the particle [15, 16].

On impact the deceleration of the particle generates the indentation force on the substrate. It is, however, more convenient to use an energy consideration where the kinetic energy is equated with the work done during impact. In this consideration the elastic part of the work is usually neglected, since it is estimated to be only 1 to 4 % of the total work.

With the definition of constant indentation hardness equating the kinetic energy of the particle with the plastic work done gives

$$U_{kin} = \int_0^{\delta_m} P(\delta)d\delta = H\int_0^{\delta_m} A_{ind}(\delta)d\delta = H\,\delta V \tag{2.12}$$

with $P(\delta)$ the indentation force at a certain indentation depth δ and δ_m the maximum indentation depth. So the translation from indentation to impact is obtained by substituting the indentation volume with the ratio between kinetic energy of the particle and the hardness of the target.

$$\delta V = \frac{U_{kin}}{H} \tag{2.13}$$

Note that particle shape is not included in this relation. Remembering that the equations in the previous section only depended on the indentation volume (δV), the particle shape is apparently not important for impacting particles. Within the limitations of the model (long cracks, "well-developed plasticity") the results should apply for all kinds of angular particles and even for spherical particles.

2.3.2   Transitions and erosion map

Equation 2.11 can easily be rewritten into the threshold energy equation for lateral and radial fracture where $C_{\delta V}$

$$U_{kin} = C_{\delta V}\frac{E^{3/2}K_{Ic}^6}{H^{13/2}} \tag{2.14}$$

Table 2-1 summarises the values of the pre-factors for the different thresholds. It shows a difference of up to two orders of magnitude in the values between the threshold for radial and lateral cracks. This suggests the presence of a zone with dominant radial cracks. Considering the quality of the transition models, no value should be attributed to the size of this zone suggested by the values of $C_{\delta V}$.

Table 2-1: The pre-factors ($C_{\delta v}$) for the crack threshold (relation 2.14).

	crack length = plastic zone	"apparent threshold"
Radial cracks	$2.2 \ 10^3$	-
Lateral cracks	$2.4 \ 10^5$	$2.3 \ 10^4$

Table 2-2: The material parameters of AF 45 boro-silicate glass used in the theoretical model.

Parameter		Value	
Young's modulus	E	66.1 ± 0.12	GPa
Hardness	K	5.13 ± 0.09	GPa
Fracture toughness	K_{Ic}	0.89 ± 0.12	MPa·m$^{1/2}$
Specific mass	ρ_t	2727 ± 2	kg/m^3

Using the material parameters of the AF 45 glass (Table 2-2), the threshold values for the kinetic energy are obtained in Table 2-3. For comparison: the threshold energy for median cracks calculated by converting the P^* value [13] and [14], is $1.5 \cdot 10^{-8}$ J.

The thresholds can be plotted in an erosion map giving a quantitative version of the map Hutchings [8] drew. This paper prefers a one-dimensional representation using the kinetic energy of the particle as the single independent variable.

Table 2-3: The theoretical threshold energies for AF 45 glass.

	crack length = plastic zone	"apparent threshold"
Radial cracks	$6.0 \ 10^{-9}$ J	-
Lateral cracks	$6.5 \ 10^{-7}$ J	$6.4 \ 10^{-8}$ J

2.3.3 Practical parameters

In addition to the thresholds, some process parameters are of interest for describing a practical powder blasting process.

Erosion rate and efficiency

The rate of material removal is one of the important parameters for an industrial process. Classically, in erosion literature, this parameter is expressed in the erosion rate: the ratio of removed material weight and the weight of impacting particles.

We introduce a second parameter: the erosion efficiency. Since the kinetic energy of the particles is the primary process parameter and not their weight, we define the erosion efficiency as the amount of removed target per amount of energy in the

incoming particles. As we will demonstrate, the erosion efficiency is a better parameter for comparison of erosion processes with different particle sizes.
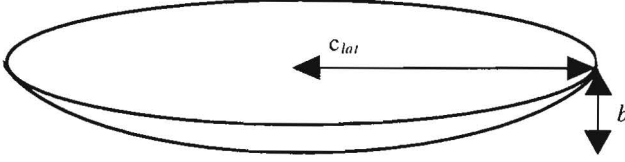
Figure 2-3: The volume modelling the erosion per particle.

We estimate the amount of removed material per particle impact as the weight of the sphere cap with the radius of the length of the lateral crack and depth of the plastic zone (b, see Figure 2-3). Since each particle is supposed to remove the same amount of material, interaction between an impact and cracks or surface roughness remaining from preceding impacts is effectively neglected. The volume of the sphere cap is approximately $\frac{1}{2}\pi b c_{\text{lat}}^2$.

The erosion rate is now defined as:

$$E_{rate} = \frac{Volume \times \rho_t}{m_p} = \frac{\pi}{2} \frac{bc_{lat}^2 \rho_t}{m_p} \tag{2.15}$$

and the erosion efficiency

$$E_{eff} = \frac{Volume \times \rho_t}{U_{kin}} = \frac{\pi}{2} \frac{c_{lat}^2 b \rho_t}{U_{kin}} \tag{2.16}$$

with ρ_t the specific mass of the substrate and m_p the mass of a particle. Substituting the equations (2.2, 2.5/2.7, 2.13) leads to the following relations:

$$E_{rate} = \tfrac{1}{2} E_{eff} v_p^2 \tag{2.17}$$

$$E_{eff} = \frac{3^{1/6}\pi^{2/3}}{2^{4/3}} \frac{\mu \zeta_L \alpha_0^{1/3}}{A} \frac{\rho_t E^{5/4}}{H^{5/2} K_{lc}} \left(3A^{1/2} H^{13/12} \alpha^{1/12} U_{kin}^{1/6} - 3^{5/6} \zeta_0^{1/4} K_{Ic} E^{1/4} \right)$$

$$\tag{2.18}$$

with v_p the particle velocity. Note that the erosion efficiency is a function of the particle kinetic energy only, whereas the erosion rate also depends on the particle velocity. Since theory shows the erosion being governed by the kinetic energy of particles only, we feel that the erosion efficiency is the parameter best suited to describe erosion processes, especially for comparing results obtained with different particle sizes and velocities or different erodent materials.

The current model for erosion rate differs from those in the literature mainly in two ways. As Buijs [1] showed, the erosion models commonly use a pillbox shape for the volume, the dimensions of which differ per model. Like Buijs we correlate the size with length of the lateral crack and the depth of the plastic zone, but we use a sphere cap since it enables us to calculate an estimate for a surface roughness.

A second difference is that this paper uses the full equation for the length of the lateral crack (including apparent threshold) in the erosion model, whereas most papers use the relation for long cracks. These equations can be obtained from our results by setting the second term to zero in equation 2.18 (i.e. replacing ζ_0 with zero).

Surface roughness
Surface roughness can be expressed in several integral measures. This paper chooses to use the R_a value. To enable a comparison between theory and experiment, the R_a value is calculated for a surface that is fully covered with single impacts such as the one in Figure 2-3. By assuming that no crack interaction occurs and that the surface is fully covered with impact sites, the surface roughness can be calculated over one impact site only.

Using the definition of the surface roughness, the R_a value is obtained, after determining the average surface position (y_0, see Figure 2-4), by adding the volume of the substrate above this position and that of the hole below it and dividing it by its projected surface (A). This gives an approximate solution for R_a.

$$R_a = \frac{1}{A}\int_A |y - y_0|\, dA \approx \frac{b}{4} = \frac{\mu}{4}\left(\frac{E}{H}\right)^{1/2}\left(\frac{3}{2\pi}\right)^{1/3}\frac{U_{kin}^{1/3}}{H^{1/3}} \qquad (2.19)$$
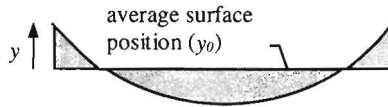
Figure 2-4: Cross-section of the sphere cap. The shaded areas contribute to the surface roughness.

The R_a value of a single impact obtained in this way is a moderate estimate of the surface roughness. Crack interaction in the actual situation might either increase or reduce the roughness. Successive impacts at the same impact position enlarge the depth of the pattern increasing surface roughness, while slightly overlapping crack patterns remove the ridges between the sites reducing the roughness.

Strength

For calculating the strength of the eroded substrate, we assume that the radial cracks from the particle impacts determine the strength of a substrate, acting as flaws for crack initiation. In indentation theory [9], the stress concentration factor K_I is described by the sum of a contribution of the applied stress (σ) and a contribution of the equilibrium stress around the crack already present

$$K_I = Y\sigma\sqrt{c} + \beta E^{1/2}H^{1/2}\frac{\delta V^{2/3}}{c^{3/2}} \qquad (2.20)$$

with Y ($2/\pi^{1/2} \approx 1.28$, [9]) the shape factor for penny-shaped cracks. The second term contains the contribution of the residual stress field at the crack tip from the indentation event, where we neglect the eventual stress relieve by removal of the plastic zone by lateral cracks. The first term describes the influence of the external applied stresses (σ). For the indentation volume, the kinetic energy can be substituted using equation 2.13.

Failure occurs when d K_I/dc=0 [17]. With this the crack size at failure (c_m) can be derived to

$$c_m = \left(4\beta\right)^{2/3}\frac{E^{1/3}}{K_{Ic}^{2/3}H^{1/9}}U_{kin}^{4/9} \qquad (2.21)$$

Substitution in equation 2.20 gives the failure stress

$$\sigma_f = \frac{3}{4Y}\left(\frac{1}{4\beta}\right)^{1/3}\frac{K_{Ic}^{4/3}H^{1/18}}{E^{1/6}}U_{kin}^{-2/9} \qquad (2.22)$$

2.4 Experimental procedures

Powder sizing

All experiments were performed with standard alumina abrasives with a mean particle size ranging from 9 to 200 µm. Most powders were FEPA classified F80 to F600 by Starck. Figure 2-5 shows a SEM photograph of the typical shapes for these particles.

For each powder, the size was measured using a Sedigraph 5100 sedimentometer. As an example Figure 2-6 shows the size distribution of a number of these powders. In our interpretation we will replace the size distribution of a powder with its mass-averaged particle size. Since all distributions were found to have the

same relative width, as Figure 2-6 illustrates, changing from mass-averaged to number-averaged particle size would mean a change with a constant factor.
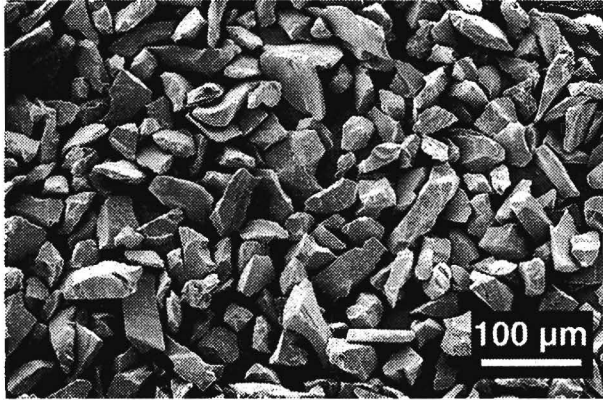
Figure 2-5: A characteristic SEM picture of abrasive Al_2O_3 powders used (here F320, 29 µm).
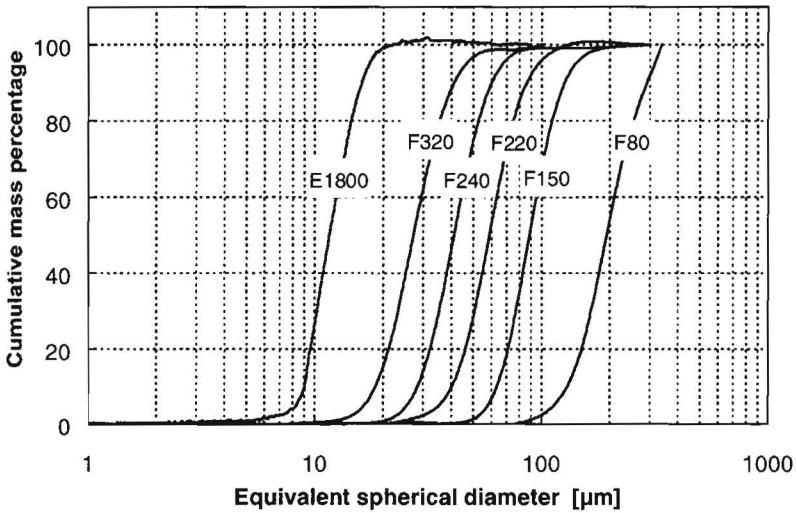
Figure 2-6: The cumulative size distribution for a number of the powders used.

Velocity measurement

Two types of velocity measurement technique were used: a double disk (DD) and a Laser Doppler anemometer (LDA).

In the earlier erosion experiments the velocity was measured using a double disk technique. The measurement procedure consisted of the measurement of velocity before and after each measurement series with equal particle velocity. The erosion data were accepted only if the velocity had not changed over an experiment.

Each velocity measurement consisted of four separate measurements. At two rotation velocities of the disk, two registrations were made. In this way the variation in the measured values was found to be within 8% of the average value.

Later erosion experiments use a one-dimensional Laser Doppler system (FlowLite and BSA, Dantec, Skovlunde, Denmark). By changing the erosion set-up to fixed jet, the velocity could be measured during the actual erosion experiments. Since the Laser Doppler technique measures the velocities of individual particles, it also gives insight into the variation of particle velocities in an abrasive jet (see Figure 2-7). Although the width of the velocity distribution is considerable, our interpretation uses the number-averaged mean velocity only.
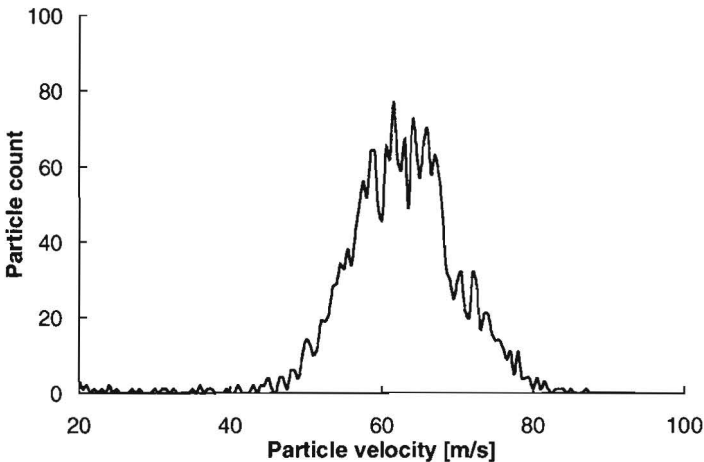
Figure 2-7: A characteristic velocity distribution as measured with the LDA system ($v_{mean} = 62.5$ m/s).

To enable the combination of results obtained with the two different measurement techniques, the DD method was calibrated against the LDA one, giving a calibration factor that was used for translating the DD data into LDA data. The procedure is described in Appendix B.

Target material
All experiments were performed on AF 45, a boro-silicate glass from Schott. The material parameters were determined at our laboratory and compared with data from the supplier. The values were found to differ only marginally, except for the fracture toughness. In that case we used our value, since we preferred our testing method (three point bending with an initial crevice of 10%). The values used in the theoretical model are given in Table 2-2.

Erosion experiments
The erosion experiments were performed using a Texas Airsonics abrasive jet machine type HP-1. In this apparatus the powder is dosed by a vibration feeder to compressed air and transported by it to the nozzle. The nozzle was an alumina cylinder with inner diameter of 1.5 mm and a length of 16 mm.
In an earlier set-up this nozzle scanned over a glass substrate. The later set-up scans the sample beneath a fixed nozzle.
Our samples had dimensions of 5 cm × 5 cm wide and 1.9 mm thick. The scan stroke was adjusted so that all the powder from the nozzle actually hits the substrate.

We measured the material removal from the sample by weighing it using a Satorius analytical balance type 1801.
The amount of powder used was measured by placing the abrasive jet machine on a scale (Mettler PM 30-K) and monitoring the weight loss over time with a PC and LabView software.

Surface roughness
The surface roughness was measured with an AlphaStep profilometer, using a needle with tip-radius of 12.5 μm. Although this rather large tip-radius might fail to record some of the finer details of the surface structure, a comparison with experiments performed using a 5 μm tip radius showed this effect to be within the scatter common to roughness measurements. The data from this instrument were sent to a personal computer, where they were filtered according to the norm DIN 4777.

Strength
For the strength tests, 1.9-mm thick glass sheets were uniformly eroded at known process conditions, which removed a layer of about 50 μm. From the eroded sheets, test samples (length 40 mm, width 20 mm) were cut for the three-point bend test (3PB, span 30.0 mm).
These samples were tested at a crosshead speed of 2 mm/min which gave the nominal stress rate was about 15 MPa/s. To have a reproducible slow crack growth

during the strength test, the temperature and humidity in the test laboratory were constant (20±1 °C, 50±5 % RH).

In the calculation of the fracture stress σ_f, for the three-point bend test, a correction for wedging stresses resulting from the loading roller is applied. This results in [18]

$$\sigma_{f,3PB} = \frac{3F_f l}{2w\,h^2}\left(1 - 0.266\,\frac{2h}{3l}\right)$$

(2.23)

with h and w respectively the height and the width of the sample, l the span of the test and F_f the force at failure of the sample. For each test series for a particular condition, 30 samples were broken to obtain reliable statistics. The data are processed using Weibull statistics. The failure probability is approximated by the estimator $P_f = (i-0.5)/n$ (i is the rank, n is the number of samples). Weibull slope and characteristic strength were determined in a least-squares regression analysis in combination with a weight function [19]. The strength is defined as the mean fracture stress of a test series. The strength tests were supported by fractography in order to ascertain that the fracture origins were cracks resulting from powder blasting process.

2.5 *Results*

2.5.1 Surface structure

For several erosion conditions the eroded surface was photographed with a SEM (operating at 30kV) both at 45° oblique to the surface and perpendicular to a fracture surface. Figure 2-8 shows a selection of these. A weak HF etch was used to open the cracks improving their visibility.

The SEM photographs show both radial cracks and the results of chipping by the lateral cracks. The chip size and the size of the lateral cracks can be seen increasing with increasing impact velocity.

From the SEM pictures it is obviously difficult to obtain an absolute value of the radial crack size. We have the general impression that the radial crack lengths are rather small and less than expected by theory.

The surface structure is generally unstructured. A clear mark showing the structure of the lateral/radial crack system, such as the one in Figure 2-8 d), is uncommon. Generally no structure can be detected.
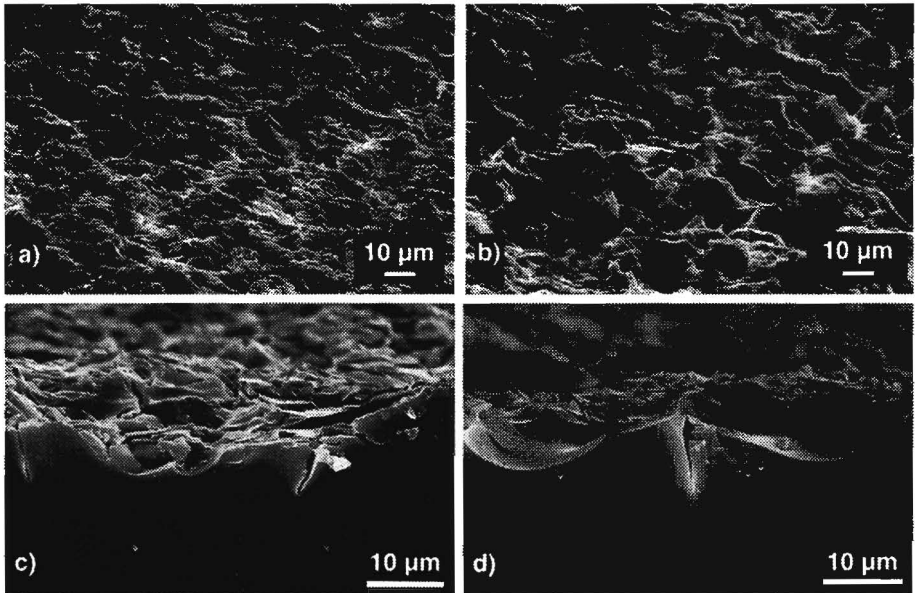
Figure 2-8: A selection of SEM photographs of eroded surfaces with 29 μm alumina particles (a) 63 m/s top view, (b) 211 m/s top view, (c) 141 m/s side view, (d) 211 m/s side view.
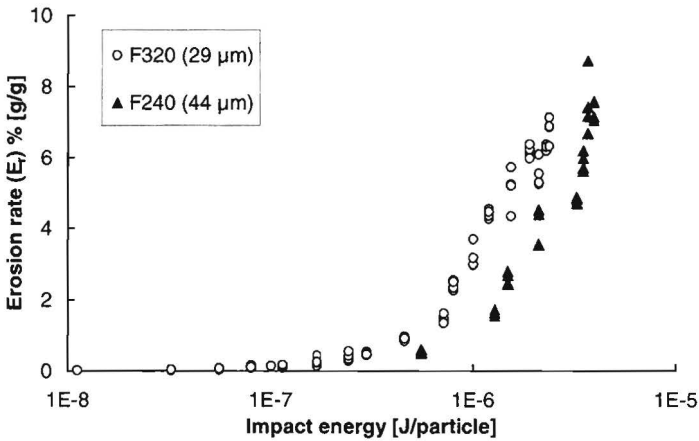
Figure 2-9: The erosion rate plotted against the particle kinetic energy for the F320 (29 μm) and F240 (44 μm) powder.

2.5.2 Erosion rate and efficiency

According to the theory, the erosion rate has limited power for describing the erosion process for different powder sizes. This is illustrated in Figure 2-9, where the erosion rate is plotted as a function of kinetic energy of the particles for powders of respectively 29 and 44 μm mean size. The erosion rate gives a smooth curve for each powder. The two curves differ considerably, however.

Theoretically the erosion at an individual particle impact depends on the kinetic energy of the particle only. Figure 2-10 confirms this theory. From the mean particle size we calculated the number of particles per gram and by dividing the erosion rate by the number of particles per gram erodent, computed the average erosion per particle. In this figure the erosion per particle is plotted against its kinetic energy for a wide range of particle sizes from 9 to 200 μm and impact velocities from 20 to 300 m/s. The broken line represents a power law fit to our data, using the least squares technique from which we obtained $0.0396\ U_{kin}^{1.23}$.
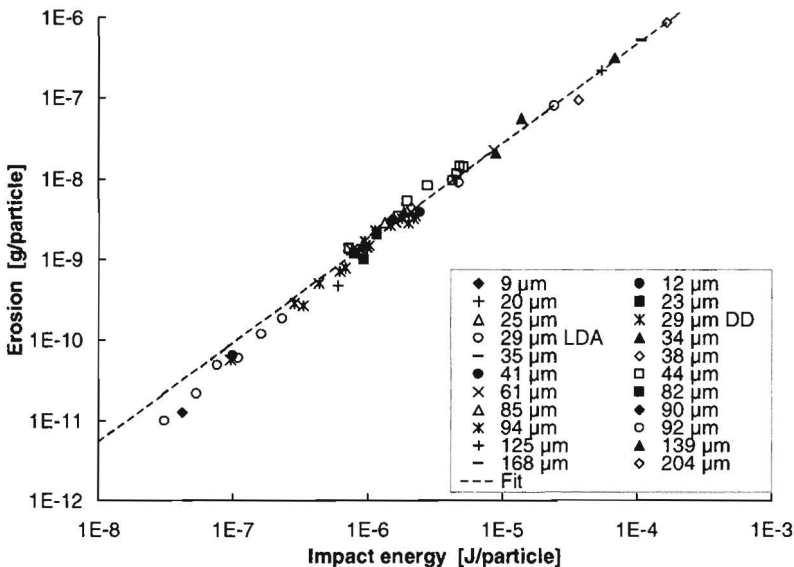
Figure 2-10: The erosion per particle plotted against the kinetic energy of the particle of a wide range of powders (9-200 μm) and velocities (20-300 m/s).

For optimising an industrial process, both erosion rate and erosion per particle are of limited importance. Here the erosion efficiency can be useful. For our full range

of measurements, Figure 2-11 depicts the erosion efficiency against particle kinetic energy. It shows the erosion efficiency to be mildly dependent on particle energy.
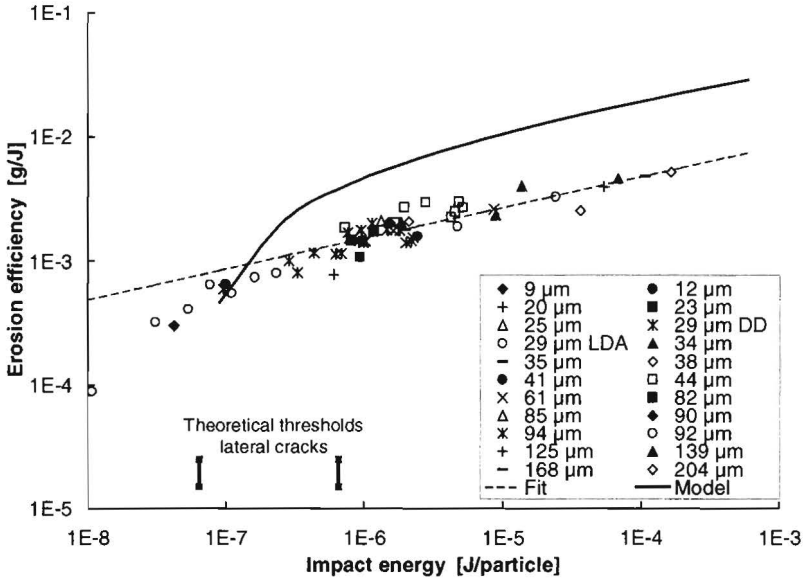
Figure 2-11: The erosion efficiency plotted against the kinetic energy of the particles over a wide range of powders (9-200 µm) and velocities (20-300 m/s).

Here again the broken line is a power law fit to the data using least-squares fitting, giving ($4.75 \ 10^{-2} \ U_{kin}^{0.247}$), and the solid line is the prediction from equation 2.18 ($0.126 \ U_{kin}^{0.167} - 8 \ 10^{-3}$). The short vertical lines near the horizontal axis indicate the predictions of the crack thresholds for lateral cracks derived from Table 2-1 (see Table 2-3). The theoretical threshold for radial cracks is outside the range of the figure.

2.5.3   Surface roughness

The surface roughness was measured in two orthogonal directions corresponding with the scan directions of the air jet over the substrate. We found no significant difference in the results, so took the mean value as the surface roughness.

Figure 2-12 plots the surface roughness against the kinetic energy of the impacting particles for all our experiments. As in the previous section, this figure shows that it is the kinetic energy that governs the surface roughness.

The solid line shows the theoretically obtained curve ($240 \ U_{kin}^{0.333}$), while the broken line gives a least square fit of the results ($75.4 \ U_{kin}^{0.253}$).

The short vertical lines near the horizontal axis indicate the theoretically obtained threshold values for the lateral and radial cracks (see Table 2-3).
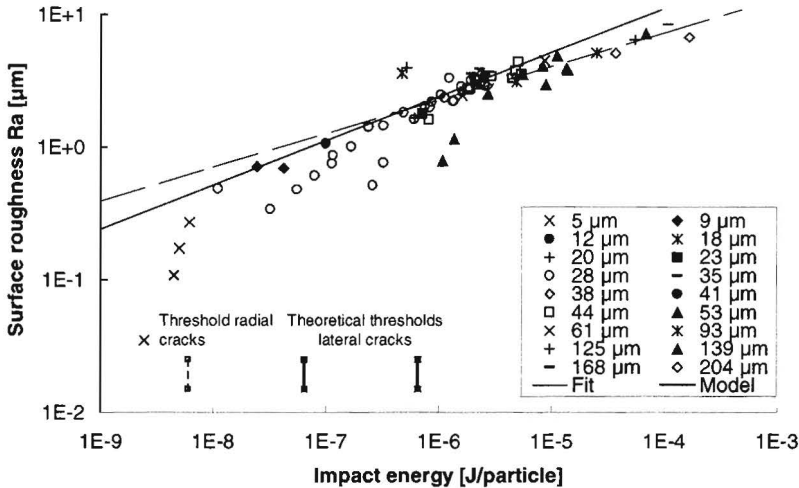
Figure 2-12: The surface roughness (R_a) plotted against particle kinetic energy of the particle of a wide range of powders (9-200 μm) and velocities (20-300 m/s).

2.5.4 Strength

Fractography showed that the erosion damage was the strength determining factor in 3PB testing. No preferable crack initiation was observed at the edges. The strength data for the surfaces, eroded with 29-μm particles at various velocities, are presented in Figure 2-13. A fairly homogeneous damage pattern is achieved for all blasting conditions. The Weibull modulus is, on average, about 20 for all the test series. At lower blasting pressures (low velocities), the powder flow varied somewhat which resulted in a slightly lower Weibull modulus.

In Figure 2-14 the average failure stress is given as a function of the kinetic energy. The error bars indicate the standard deviation of the samples. Experimental data for various particle sizes and particle velocities are represented with the same line: $\sigma_f \cong U_{kin}{}^\gamma$. From a least-squares fit on the experimental points, $\gamma = -0.10$ is obtained. It clearly deviates from the theoretically predicted slope of $\gamma = -2/9$ (equation 2.22). The theoretical line is shown in Figure 2-14 as a solid line.
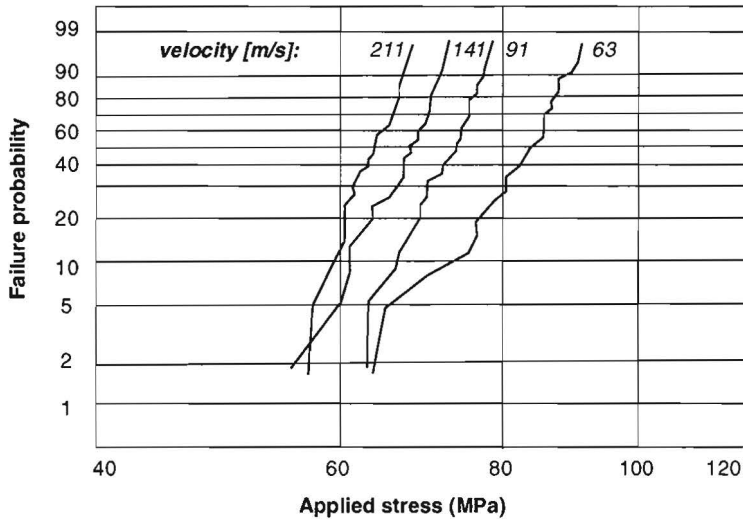
Figure 2-13: An example of a Weibull plot displaying the strength distribution of the samples eroded with 29 μm particles at different velocities.
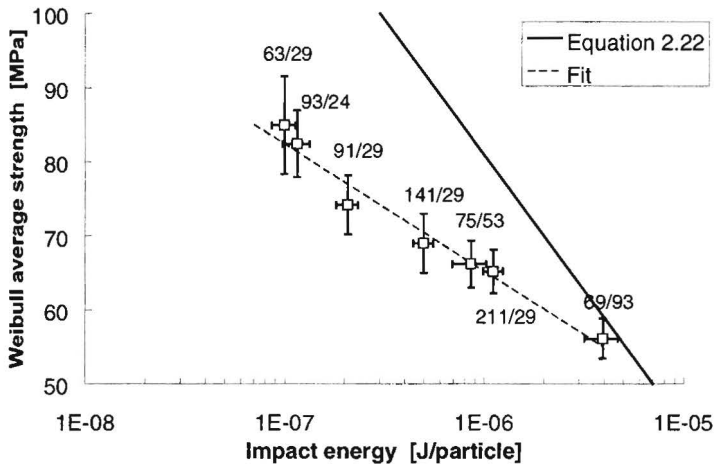
Figure 2-14: The average failure stress as a function of kinetic energy. The ratio at the individual point gives particle velocity /particle size ([m/s]/[μm]).

2.6 Discussion

2.6.1 Distributions and averaging

The theoretical model predicts erosion being dominated with the kinetic energy of the particle. Starting from a single particle the modelling predicts parameters for multiple-particle erosion, in which all particles have the same kinetic energy.

In the experiments both the velocity and the particle size show a considerable width in their distribution, leading to a comparable width in the energy distribution. Since it is convenient to compare scalar functions, we have chosen to calculate the averaged kinetic energies for our experiments and compare these with predictions of the model at these energies. Since the energy distribution could not be measured, the average kinetic energy was calculated using the mass-averaged particle size (number-averaged mass) and the number-averaged velocity:

$$\left\langle \frac{1}{2} m v^2 \right\rangle \approx \frac{1}{2} \langle m \rangle \langle v \rangle^2 \tag{2.24}$$

The choice for the way of averaging is rather arbitrary. However, since the distribution curves of both particle size and particle velocity are rather isomorphic, a different way of averaging will only effect in changing the average energies by a constant factor. In the comparison between experiments and theory this would shift the curves horizontally.

2.6.2 Material properties

Apart from the models being based on quasi-static indentation theory, the material parameters used in the model predictions (Table 2-2) are determined with quasi-static measuring techniques. Since the deformation rates during impact are very high (up to 10^6 1/s, [20]) strain rate effects on the measured parameters can be expected.

In the elasto-plastic indentations considered, the apparent indentation hardness (H) at the fast deformation rates might be considerably higher than the one measured in quasi-static tests. Whether this increase in apparent hardness corresponds to an intrinsic material property or is an artefact of the measurement technique is still unclear.

More evidence is available for the strain rate dependence of the fracture toughness (material strength), caused by stress corrosion or slow crack growth. Several sources correlate the fracture strength of a material (σ) with the stressing rate ($d\sigma/dt$) via $\sigma \propto (d\sigma/dt)^{1/(n+1)}$ (for an overview see [21]). The value of the power n varies commonly between 20 and 35. Using this relation with an n of 32, the fracture toughness is estimated to be about a factor 2 higher than the one given in Table 2.2 (strain rate at measurement $\approx 10^{-4}$ 1/s, at impact $\approx 10^6$ 1/s).

The dependency of strength on strain rate however must be used with care. The relation has been verified only for characteristic strain rates from 10^{-5} 1/s to 10^2 1/s [see e.g. 22, 23]. Applying the relation for impact requires extrapolation over four orders of magnitude, while the measured curves [23] display a tendency to deviate from the relation at high strain rates. The factor 2 should therefore be considered to be a worst case estimate for the strain rate effect.

The compaction behaviour of the AF 45 borosilicate glass might introduce another deviation from the material model used in the indentation models. The AF 45 glass belongs to a group of glasses that have a more open structure than the soda-lime Lawn and Evans used for their indentation experiments. Soda-lime glass itself does display some densification by indentation (compaction, [24]), the effect is more prominent for open-structured glasses. It is visible as a ramping at the ballistic impact of pyrex rods [25] or densification of the glass under the indenter [26, 27]. Although no specific data is available on the compaction of AF 45 glass, it can be expected to have an increased compaction relative to that of soda-lime glass.

The influence of the phenomena discussed in this section on the comparison between model and experiment may be difficult to quantify. However, they will all give a reduction of the size of plastic zones and cracks compared with those predicted by the models.

2.6.3 Erosion rate and efficiency

Our measurements confirm here the theory that erosion depends on particle parameters primarily by its kinetic energy. We were able to produce master curves over several orders of magnitude that combined measurements with particles differing up to four orders in magnitude in particle kinetic energy.

By fitting to the erosion efficiency curve, we found that it depended on the kinetic energy with a power of 0.247. This power can be determined quite accurately from our measurements, since the data range over four orders of magnitude.
In the literature several models (e.g. [1, 8]) have been derived giving a theoretical relation between erosion rate and impact velocity in the form of a power law with the power of 7/3. For large impact velocities our model gives the same result, translating it (by using equation 2.17 and replacing the velocity by the kinetic energy) into an erosion efficiency depending on kinetic energy with the power 1/6.
However, since our model contains a threshold for erosion, the theoretical line is slightly curved giving it a slightly higher apparent slope. By fitting a power law to the part of the theoretical curve in Figure 2-11 that was not strongly bent, apparent

slopes can be obtained comparable with those from the experiments. The model thus describes the influence of kinetic energy on erosion very well.

The theoretical erosion efficiency is about four times higher than the measured one. Considering the assumptions in the model, this is a good achievement. There are several reasons why the theoretical model overestimates the actual erosion per particle impact. Besides the ones mentioned in section 2.6.2 some of the more important are:

- The model assumes that all material above the lateral crack is removed. Single impact studies show that this only occurs for a fraction of the impacts.
- The model does not incorporate impact site interaction. An impact will hit a part of the surface that has been hit by many previous particles. The surface roughness and the presence of subsurface cracks (lateral and radial) will prevent the lateral cracks from growing to their full length. As Figure 2-8 illustrates, only occasionally can a full lateral crack system be found.
- The model is based on well-developed plasticity, whereas certainly part of our experiments are quite close to the threshold of erosion where this assumption does not hold.
- The models for crack length assumed well-developed crack sizes. Although it is hard to be precise, in our experiments we calculate crack lengths to plastic zone ratios from 1 to 5. Over a large part of the area, the model assumption of a point force will be not valid.

For comparing experiments with theory a choice for an averaged kinetic energy seems obvious. We approximate this value by using the mass-averaged particle size and the number averaged velocity.

Figure 2-11 suggests a weak threshold in erosion below a kinetic energy of 10^{-7} J. This confirms the order of magnitude for the threshold of lateral cracks found theoretically (see Table 2-3). The weakness of the threshold found experimentally might originate in the wide distribution in particle size and velocity. The distribution in kinetic energies might give a diffuse threshold, which could become visible only when even the particles with the highest energy stop invoking lateral cracks.

We compared our erosion data with those of Buijs [1]. For the higher velocities these data coincide. We were, however, not able to reproduce the results for lower velocities, which show a rather fast decrease with velocity. After discussion with the author, we concluded together that the experimental procedure of Buijs

probably failed to register the inaccuracy in the pressure measurement, which resulted in overestimating the particle velocity.

2.6.4   Surface roughness

Figure 2-12 shows the calculated surface roughness (R_a) being of the same magnitude as the measured ones. As surface roughness parameters are integral values, this cannot tell that the model assumptions are correct.

The surface roughness is a rather crude parameter. For model verification, at least a steady state is required. As Figure 2-15 shows, it is uncertain whether such a state exists in surface roughness. Anyway, it might require quite a high dose of particles per surface area, especially at low impact energies.
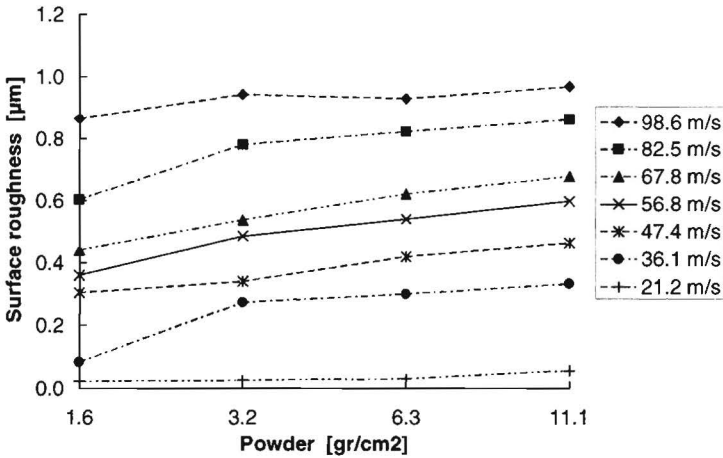
Figure 2-15: The development of the surface roughness towards a steady state (28.5 μm particles).

Figure 2-12 shows a difference in power of the experimental (0.25) and the theoretical curve (0.33). Despite the uncertainty in the surface roughness determined, we think this might originate in the interaction between a particle impact and the structure of the earlier erosion. At high impact energy, larger cracks are formed, which can remove the edges of earlier impacts more easily. Only a slight difference in the edges would give the decrease in power observed.

At very low energies the surface roughness decreases very quickly with energy, even at a logarithmic scale, which could be interpreted as a crack threshold.

Although the variance is rather wide, the relation between surface roughness and particle energy is valuable for an industrial purpose. Using a surface roughness

measurement, an initial crude estimate can be made of the process conditions (energy) of the erosion process.

2.6.5   Strength

As Figure 2-14 shows, the slope found experimentally (-0.1) differs considerably from the one expected theoretically (-2/9). In the literature, a variety of slope values have been reported on strength in erosion and indentation.

Ritter et al. [28] measured the strength of eroded glass for various erosion conditions. The results are well described with the slope $\gamma = -2/9$, as predicted with indentation theory. In [29] erosion and indentation experiments on soda-lime glass and various types of ceramics are compared. For most ceramics, the (log-log) plot of the failure stress as a function of the kinetic energy of the impacting particle has a slope γ significantly smaller than -2/9. For alumina, $-0.16 < \gamma < -0.05$ has been reported [30]. In these cases, a crack length-dependent toughening mechanism is used to describe the experimental results.

Indentation theory predicts a slope of -1/3 for a log-log plot of the failure stress as a function of the indentation load. For soda-lime glass, this slope is determined experimentally [31]. On small indentation loads, both a slope of -1/3 [32] and a smaller slope (-0.23) [33] are reported on fused silica glass.

Explaining the difference with a toughening mechanism, as proposed for ceramics, is not reasonable for glass. In our experiments, however, the kinetic energy of the impacting particles is considerably lower (0.1 - 5 μJ) than the energy in erosion experiments on soda-lime glass (6-600 μJ) and alumina [17]. This might explain the deviation observed between our measurements and theory. Being close to the crack threshold, the theory, based on "well-developed" crack patterns, might not hold. The lower slope of the $\ln \sigma$ - $\ln P$ plot, reported in [33] supports this suggestion.

A combination of a distribution and a threshold in the kinetic energy could influence the slope of the experimental curve. If only the upper part of the energy distribution determines the strength and there is a crack threshold in this region, the mean energy of the active particles increases more slowly then the energy of the whole distribution. This would lead to a lower slope than expected.

Comparing the experimental and the theoretical curve in Figure 2-14, one should note that both are plotted against the average kinetic energy. For the experimental curve this is not fully correct, since the strength is determined by the weakest spots. These are the larger cracks originating from impacts at the high end of energy

distribution. For a better comparison with theory, the experimental curve thus should be plotted against the energy of these high-energy particles. These particles may have an energy a factor of five to ten higher than the average energy shifting the experimental curve to the right. The theoretical and the experimental curve then would intersect near the centre of the investigated area, like the case for the surface roughness.

2.7 Conclusion

Starting from the models of Lawn and Evans, we derived a quantitative estimate for the parameters determining the erosion process, such as erosion efficiency, surface roughness and strength. From this we found that there is only one independent parameter determining the influence of the particle: its kinetic energy. On this basis, we defined the erosion efficiency (amount of erosion per amount of kinetic energy of the incidenting particles) as a better parameter to describe erosion processes than the erosion rate.

With erosion experiments using a wide range of particle sizes and velocities, we confirmed the dominance of the particle kinetic energy in erosion processes with erosion efficiency, surface roughness and strength. The quality of the predictions of the quantitative model differs per parameter:

-   The variation of erosion efficiency with kinetic energy is well described. In contrast to earlier models, it predicts a power of 0.25, which is also found from the experiments. The actual erosion is overestimated by a factor of four, which we consider as a good result, considering the assumptions made in the model.
-   The surface roughness is predicted in the correct order of magnitude. The dependency on kinetic energy is, however, slightly overestimated. Considering the definition of surface roughness, it is hard to find a plausible cause.
-   The model overestimates the slope of strength versus kinetic energy by a factor of two. This might originate from the fact that our experiments are quite close to the crack threshold, whereas the theory assumes well-developed cracks. A second reason may lie in the rather wide distribution of kinetic energies of the erodent we used in each measurement.

Appendix A: The fitting of the plastic zone theory

One of the building blocks of the theory of the "well-developed plasticity model" for indentation is the expanding cavity model presented by Hill [11]. His analysis provides a relation between the ratio -cavity size to size of the plastic zone (b/a')- and the ratio H/E [6]:

$$\frac{H}{E} = \frac{2}{9} \frac{1 + \ln(b/a')^3}{(1-v)(b/a')^3 - \frac{2}{3}(1-2v)} \tag{2.25}$$

Since an explicit relation for b/a' is more convenient this relation is usually approximated by a power law

$$\frac{b}{a'} = \mu\left(\frac{E}{H}\right)^m \tag{2.26}$$

The common value of m mentioned in literature is $m=0.5$. In the Figure 2-16 we show that this value does not fit the curve very well. By performing a least-squares fit to the logarithmic curve, we find a better fit with $m = 0.43$ and $\mu = 0.80$. The value of μ found by least-squares fit with m fixed to 0.5 is $\mu = 0.63$.
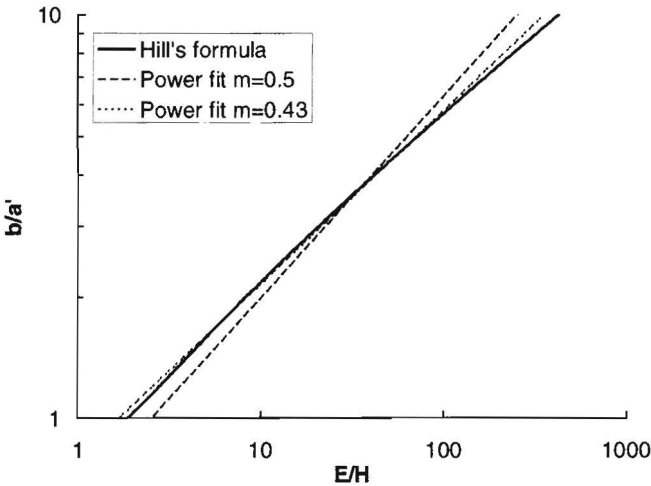
Figure 2-16: Hill's relation between b/a' and E/H and two power law fits.

Appendix B: Comparison between double-disk and laser doppler velocity measurements

In our experiments, two techniques have been used to measure particle velocity. In the earlier experiments we used a Double Disk Anemometer (DD, see for example [34]), which is an off-line technique which is quite elaborate for accurate measurements (Δv < 10 % of value). In the later experiments we used a Laser Doppler anemometer (LDA), which can be operated on-line during an erosion experiment and gives fast results with very high accuracy (Δv < 1% Full Scale).

To enable us to combine the results, we measured a calibration curve for the average particle velocity of F320 alumina accelerated by our system. Figure 2-17 shows the linearity in the relation between the velocities measured with the two techniques.

The DD technique, however, registers a 15 % smaller value than the LDA technique, which findings are consistent with those of Ponnaganti et al. [35]. We attribute this effect to the difference in measuring technique. The LDA measures the velocity of individual particles and calculates from this the number-averaged mean velocity. In the DD method, the distance between two markings on a tape is measured. Since the heavier particles contain more kinetic energy, they will leave a stronger mark than the faster, lighter ones. The DD method thus measures a lower, more mass-weighed average velocity.
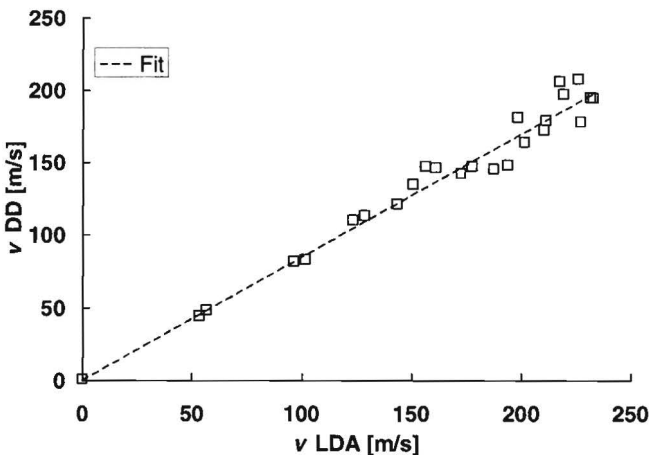
Figure 2-17: Comparison between LDA and Double Disk velocity measurement.

Appendix C: Comparison of erosion data for various erodents.

Introduction

The theoretical models for erosion of brittle substrates with hard, angular particles derived in this chapter indicate that the particles influence erosion by their kinetic energy only. Plots of erosion parameters like the amount of erosion, the resulting surface roughness and the reduction in substrate strength, against the kinetic energy of the impacting particles confirms this for alumina particles with a considerable range in particle sizes and impacting with a substantial difference in velocities.

Although these results make the findings of the theory plausible, the theory is only verified for one type erodent material. In this appendix the experimental results are therefore compared with recently published data from Feng and Ball [36, 37] obtained for glass erosion with five different erodent materials. To assist the discussion the experimental procedure used by Feng and Ball is summarised first.

Experimental procedure

Feng and Ball [36] used a conventional type of gas blast apparatus [38], whereto the erodent was fed at a rate of about 10 g/minute. Prior to the erosion experiments, the exit velocity of the particles was measured as a function of particle size and feeding pressure to the erosion rig using an opto-electronic flight timer similar to that used by Kosel and Anand [39]. During the erosion experiment the desired particle velocity was selected by varying the air pressure.

Five different erodent materials were used having angular particles: silica, alumina, silicon carbide (SiC), diamond and tungsten carbide (WC). The powders were separated in size fractions by sieving according to British standard BS 410. In this way five fractions were made for the alumina, silica and SiC powders, namely 63-106 µm, 106-125 µm, 180-250 µm, 400-500 µm, 800-1000 µm. Two size fractions were available for the diamond (106-125 µm and 180-250 µm) and only one for the tungsten carbide (180-250 µm).

The particle size distributions of these fractions were measured with a laser diffraction particle sizer to determine their particle size. It was found that this average particle size could be approximated reasonably well by the linear average of the sieve sizes.

As a target material soda-lime glass was used. The weight loss of the target was plotted against the amount of erodent used. From the slope of the plot the erosion rate was obtained [g/g]. Dividing the erosion rate by the average particle mass gives the erosion per particle. To simplify a comparison of different target materials Feng and Ball plotted the erosion per particle as cm^3/particle [E_p], which

is obtained by dividing the erosion per particle by the specific mass of the substrate.

A comparison of results

Figure 2-18 combines the erosion data per particle of the previous chapter with those of Feng and Ball. It clearly shows that all data coincide except that of the tungsten carbide (WC).
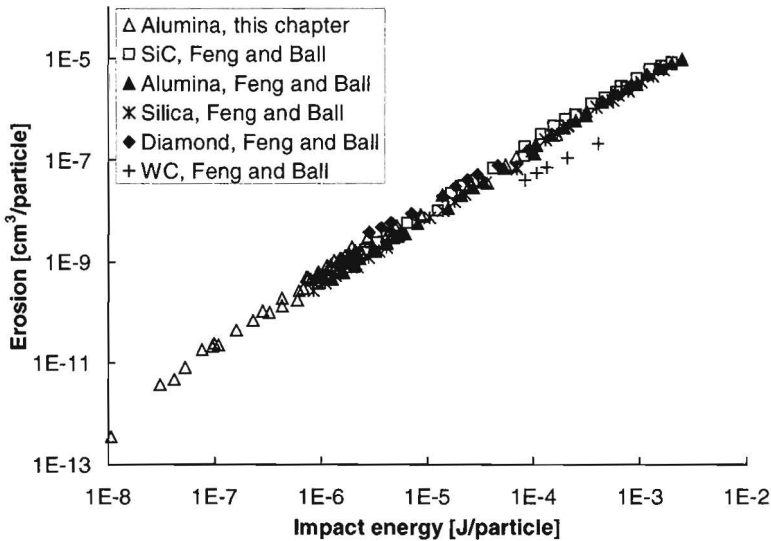
Figure 2-18: A graph combining the erosion-per-particle data from the previous section (Δ) with the data of Feng and Ball [36].

As illustrated in section 2.5 the scatter in the data can be studied best in an erosion efficiency plot. Figure 2-19 displays the same data as the previous graph, but now plotted as the erosion efficiency (here defined as cm^3/J). It shows that the scatter in the two data sets is comparable, where all data from Feng and Ball is considered to be one data set.

Plotting the results for the different erodent materials of Feng and Ball separately shows that the scatter for the individual erodent materials is considerably less than that of the entire data set (see Figure 2-20). To guide the eye, trend-lines are included in this figure. The silica and alumina data truly coincide, while the SiC data display a systematic offset. The diamond powders seem to display a different behaviour, although the erosion values are of the same values as the other materials. The tungsten carbide data obviously miss the trend set by the other particles completely.
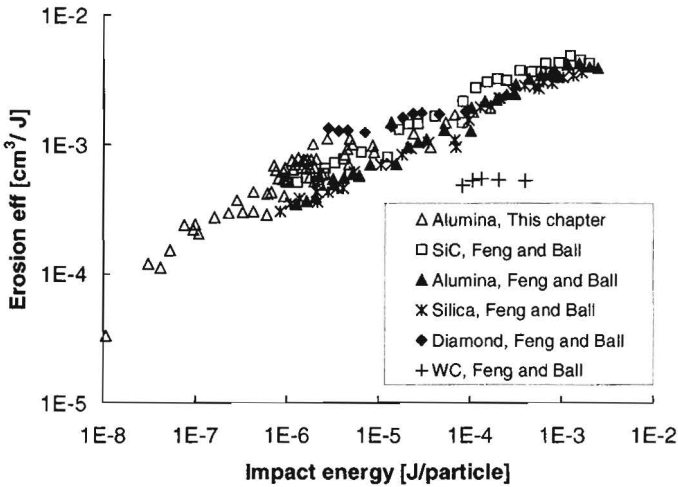
Figure 2-19: A graph combining the erosion efficiency data [cm³/J] from the previous section (Δ) with the data of Feng and Ball.
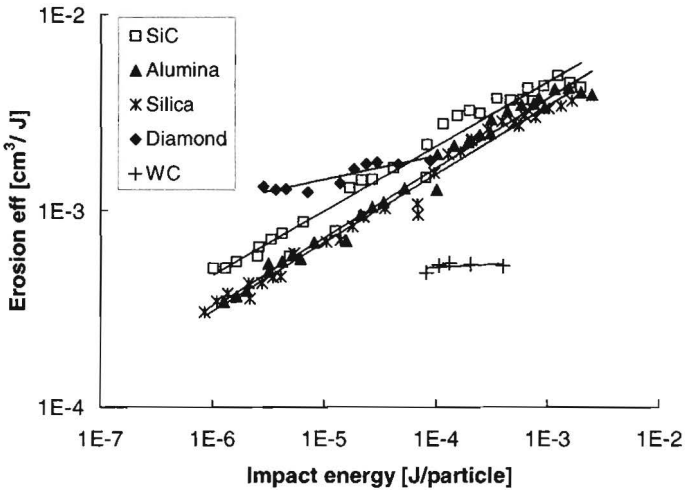
Figure 2-20: The erosion efficiency data [cm³/J] of Feng and Ball illustrating the differences between the different erodents.

Discussion and conclusion

As the figures show the erosion data for most erodent materials confirm the theory derived in this chapter by coinciding on a single line. The results for the tungsten carbide (WC) particles are the only ones that do not follow this trend. Before conclusions may be drawn of this deviation of the WC particles, the significance of the results should be verified. For example, since WC has a considerable higher specific mass than all other abrasives used (15000 kg/m^3 compared to 2000-4000 kg/m^3), it might be possible that the air jet did not accelerate the WC particles to the velocity expected from the calibration curve.

The data of Feng and Ball show per erodent a significant lower scatter than the alumina data presented in section 2.5. This can be attributed to the better-defined size of the powders used by Feng and Ball. The powders used in this chapter are commercially (FEPA) classified and contain original and reused powders, while Feng and Ball used sieved original powders.

The data of Feng and Ball show the data for silica and alumina to coincide. Although the silica particles are only slightly harder than the glass substrate, they can apparently be treated as hard particles.

The data for silicon-carbide particles seem to give an erosion efficiency of about 30% higher than the silica and alumina. Considering the accuracy of the experimental procedures it is uncertain whether this is significant.

The diamond particles display a lower slope than the other particles. The reason for this is uncertain, but it might be related to the presence of flat sides of the crystal surfaces on the diamond particles. Where the other powders are made by a crushing process, the diamond particles display a blocky structure giving away their crystal structure.

Acknowledgement

2.8 List of symbols

A	Shape factor of the chips above the lateral cracks [-], Equation 2.6.
A_{ind}	The projected surface of the indentation [m^2], Equation 2.1.
B	The apparent threshold in the lateral crack relations of Marshall et al. [-], Equation 2.7.
C	Proportionality factor in Equation 2.11.
$C_{\delta v}$	Pre-factor in the transition to lateral and radial cracks [-], Equation 2.11.
E	The Young's modulus of the substrate [Pa], Equation 2.2.

E_{eff} The erosion efficiency (mass of removed substrate per amount of kinetic energy of erodent used) [g/J], Equation 2.18 or [cm^3/J], Figure 2.19.

E_r The erosion rate (mass of removed substrate per mass of erodent used) [g/J], Equation 2.17.

F_f The breaking force at a three point bend test [N], Equation 2.23.

H The hardness of the substrate [Pa], Equation 2.1.

K_I The stress concentration factor [Pa m$^{1/2}$], Equation 2.20.

K_{Ic} The fracture toughness of the substrate [Pa m$^{1/2}$], Equation 2.3.

P The indentation force [N], Equation 2.1.

P_f The Weibull failure probability estimator [-], below Equation 2.23.

U_{kin} The kinetic energy of a particle at impact [J], Equation 2.12.

Y The stress factor of a penny shaped crack (≈ 1.28) [-], Equation 2.20.

a' The radius of the hemispherical indentation [m], Figure 2.2.

b The outer radius of the plastic zone [m], Figure 2.2.

c_{lat} The lateral crack length [m], Equation 2.5.

$c_{lat}{}^L$ The lateral crack length in the limit of long cracks [m], Equation 2.6.

c_m The crack size at failure [m], Equation 2.21.

c_{rad} The length of the radial crack [m], Equation 2.3.

h The height of a three point bend sample [m], Equation 2.23.

l The length of a three point bend sample [m], Equation 2.23.

m Exponent of fit to Hill's inflated hole model [-], Equation 2.2 and Equation 2.26.

w The width of a three point bend sample [m], Equation 2.23.

Δv The velocity difference between double disk and laser doppler velocity measurements [m/s], Appendix B.

α The shape factor of the indenter (=2 for Vickers) [-], Equation 2.4.

β Parameter in radial crack length relation [-], Equation 2.3.

γ The slope of the strength against impact energy plot [-], Section 2.5.4.

δ The indentation depth [m], Equation 2.12.

δV The volume of the plastic indentation [m^3], Figure 2.2.

δ_{max} The maximal indentation depth at impact [m], Equation 2.12.

μ Parameter of fit to Hill's inflated hole model [-], Equation 2.2 and Equation 2.26.

ρ_t The specific mass of the substrate [kg/m^3], Equation 2.15.

σ The external applied stress near a crack tip [Pa], Equation 2.20.

σ_f The failure stress [Pa], Equation 2.22.

ψ Half the top-angle of the indenter [°], Equation 2.4.

ζ_0 Proportionality factor in the lateral crack threshold ($1.2 \ 10^3$) [-], Equation 2.7.

ζ_L Proportionality factor for the limit of long lateral cracks ($25 \ 10^{-3}$) [-], Equation 2.6.

2.9 Literature

1   M. Buijs, *Erosion of glass modeled by indentation theory*, J. Am. Ceram. Soc. 77, no 6 (1994) 1676-1678.

2   L. Murugesh and R.O. Scattergood, *Effect of erodent properties on the erosion of alumina*, J. Mater. Sci. 26 (1991) 5456-5466.

3   A.G. Evans, M.E. Gulden and M. Rosenblatt, *Impact damage in brittle materials in the elastic-plastic response regime*, Proc. Roy. Soc. Lond. A. A361 (1978) 343-365.

4   S.M. Wiederhorn and B.J. Hockey, *Effect of material parameters on the erosion resistance of brittle materials*, J. Mater. Sci. 18 (1983) 766-780.

5   D.B. Marshall, B.R. Lawn, A.G. Evans, *Elastic/plastic indentation damage in ceramics: the lateral crack system*, J. Am. Ceram. Soc. 65, No 11 (1982) 561-566.

6   B.R.Lawn, A.G. Evans and D.B. Marshall, *Elastic/plastic indentation damage in ceramics: the median/radial crack system*, J. Am. Ceram. Soc. 63, No 9-10 (1980) 574-581.

7   D.B. Marshall, *Geometrical effects in elastic/plastic indentation*, J. Am. Ceram. Soc. 67, no 1 (1984) 57-60.

8   I.M. Hutchings, *Transitions, threshold effects and erosion maps*, Key Eng. Mat., 71 (1992) 75-92.

9   B. Lawn, *Fracture of brittle solids*, Chapter 8, Second edition, Cambridge University Press (1993).

10 S.S. Chiang, D.B. Marshall and A.G. Evans, *The response of solids to elastic/plastic indentation. i stresses and residual stresses*, J. Appl. Phys. 53 (1982) 298-311.

11 R. Hill, *The mathematical theory of plasticity*, Oxford University Press, Oxford (1950).

12 G.R. Anstis, P. Chantikul, B.R. Lawn and D.B. Marshall, *A critical evaluation of indentation techniques for measuring fracture toughness*, J. Am. Ceram. Soc. 64 (1981) 533-538.

13 B.R. Lawn, A.G. Evans, *A model for crack initiation in elastic/plastic indentation fields*, J. Mater. Sci. 12 (1997) 2195-2199.

14 S. Lathabai, J. Rödel, T. Dabbs, B.R. Lawn, *Fracture mechanics model for subthreshold indentation flaws*, J. Mater. Sci. 26 (1991) 2157-2168.

15 A.E.H. Love, *A treatise on the mathematical theory of elasticity*, Cambridge University Press (1952).

16 S.C. Hunter, J. Mech. Phys. Solids 5 (1956) 162.

17 B.R. Lawn, D.B. Marshall, G.R. Anstis and T.P. Dabbs, *Fatigue analysis of brittle materials using indentation flaws*, J. Mater. Sci. 16 (1981) 2846-2854.

18 S.P. Timoshenko and J.N. Goodier, *Theory of elasticity*, 3rd int. edition, Eng. Mech. Ser., McGraw-Hill (1970).

19 L.J.M.G. Dortmans and G. de With, *Noise sensitivity of fit procedures for weibull parameter extraction*, J. Am. Ceram. Soc. 74 (1991) 2293-2294.

20 I.M. Hutchings, *Tribology*, Section 6.4, Edward Arnold, London (1992).

21 S.W. Freiman, *Fracture mechanics of glass*, in D.R. Uhlman, N.J. Kreidl (eds), *Elasticity and strength of glasses*, Glass Sci. and Techn. 5, Academic Press, New York et al (1980).

22 W. Griffioen, *Optical fiber, mechanical reliability*, PhD thesis, Technical University Eindhoven (1995).

23 J. Börkman, T. Svensson, *Quick-access to fracture statistics at ultra wide range tensile test of optical fibers*, Proc. Int. Wire and Cable Symp. (1990) 373-378.

24 J.T. Hagan, *Shear deformation under pyramidal indentations in soda-lime glass*, J. Mater. Sci. 15 (1980) 1417-1424.

25 N.K. Bourne, Z. Rosenberg, A. Ginzburg, *The ramping of shock waves in three glasses*, Proc. R. Soc. Lond. A 452 (1996) 1491-1496.

26 J.T. Hagan, S. van der Zwaag, *Plastic processes in a range of soda-lime-silica glasses*, J. Non Cryst. Solids 64 (1984) 249-268.

27 D.M. Marsh, *Plastic flow in glass*, Proc. R. Soc. A279 (1964) 420-435.

28 J.E. Ritter, P. Strzepa, K. Jakus, L. Rosenfeld and K.J. Buckman, *Erosion damage in glass and alumina*, J. Am. Ceram. Soc. 67 (1984) 769-774.

29 J.E. Ritter, *Strength degradation of ceramics due to solid particle erosion*, Key Eng. Mat. 71 (1992) 93-106.

30 K. Breder, J.E. Ritter and K. Jakus, *Strength degradation in polycrystalline alumina due to sharp-particle impact damage*, J. Am. Ceram. Soc. 71 (1988) 1154-1158.

31 G.S. Glaesemann, K. Jakus, J.E. Ritter, *Strength variability of indented Soda-Lime Glass*, J. Am. Ceram. Soc. 70 (1987) 441-444.

32 T.P. Dabbs and B.R. Lawn, *Strength and fatigue properties of optical glass fibers containing microindentation flaws*, J. Am. Ceram. Soc. 68 (1985) 563-569.

33 B. Lin and M.J. Matthewson, *Inert strength of sub- and postthreshold vickers indentations on fused silica optical fibers*, Phil. Mag. A. 74, no 5 (1996) 1235-1244.

34 D.R. Andrews and N. Horsfield, *Particle collisions in the vicinity of an eroding surface*, J. Phys. D.: Appl. Phys. 16 (1983) 525-538.

35 V. Ponnaganti, D.E. Stock and G.L. Sheldon, in R.A. Bajura (ed.), *Polyphase flow and transport technology*, ASME (1980), 217-222.

36 Z. Feng and A. Ball, *The erosion of four materials using seven erodents –towards an understanding*, ICEAW conference, Cambridge 1998.

37 Z. Feng, PhD Thesis, Cape Town University, (1999).

38 P.H. Shipway and I.M. Hutchings, *A method for optimizing the particle flux in erosion testing with a gas blast apparatus,* Wear 174 (1994) 169-175.

39 T.H. Kosel, K. Anand, *An optoelectronic erodent particle velocimeter*, in V. Srinivasan, K. Vedula (eds), *Corrosion and particle erosion at high temperatures*, The Minerals, Metals and Materials Society (1989) 349-368.

3 Erosion and damage by spherical particles[*]

The previous chapter examined the erosion process of glass by hard, angular particles. Being the dominant industrial process it is advantageous to know its limitations. This chapter studies the effect of particle shape on the erosion process by investigating impacts of hard spherical particles.

Theoretical models are presented for the transitions between the different impact regimes and process parameters like erosion rate and surface roughness. To study the transition between angular and spherical particles the models are formulated for rounded particles, which include spherical particles and angular ones as limit cases. To obtain an overview of the erosion mechanisms in the presence of an elastic impact regime with its specific cone crack pattern, the transitions are plotted in so-called erosion maps. These maps are validated with single-impact experiments.

Data from erosion experiments are used to test the relations for erosion rate and resulting surface roughness. The models for angular particles do not predict a particle shape effect, which is confirmed by single impact experiments. Erosion experiments, however, indicate a significant difference in the erosion mechanism.

3.1 Introduction

The literature on solid particle impact distinguishes sharp, rounded and spherical particles for their differences in erosion behaviour [e.g. 1]. For the erosion of brittle materials, hard angular particles are of the most practical importance; angular particles are most common in nature and they inflict the most damage in technical equipment. It is for that reason understandable that the extensive erosion literature concentrates on erodents with angular shapes.

Several models have been published for impact of sharp particles [1-4] Most of these models use the analogy between solid particle impact and indentation processes. Two regimes exist for sharp particles or sharp indenters, namely plastic indentation and plastic indentation combined with lateral/radial crack patterns. Validation experiments showed that the theory is in good agreement with experiments using a variation of substrate materials [2] and using different particle sizes and velocities [4].

Although it is of limited practical importance, impact and erosion with spherical particles is interesting fundamentally because of the presence of two extra regimes, namely purely elastic impact and elastic impact with cone cracks. Understanding the impact behaviour of spherical particles is also a first step towards the modelling the transition between angular and spherical particles.

This paper presents the models for solid particle impact of spherical particles and tests these against experimental data. The models describe the particles having a radius of curvature at the impact site not necessarily equal to the particle radius to include sharp, rounded and spherical particles. The paper consists of two main sections.

In the first section the transitions between the different erosion regimes are modelled. The resulting "erosion maps" are tested with single-impact experiments. The second section derives models for erosion and surface roughness in the two regimes that involve fracture (lateral/radial cracking and cone cracking). The results of these models are compared with erosion experiments. Each section discusses the differences between experiment and theory.

As will be shown later in this chapter, the success of the modelling differs greatly between the single- and multiple-impact (erosion) experiments. The last section discusses this difference and suggests that one of the assumptions in theoretical modelling might be the cause of the observed difference.

3.2 Transitions

3.2.1 Theory

Most models for solid particle erosion are based on quasi-static indentation theory. This is appropriate since the impact speeds, although they can reach up to some

hundreds of meters per second, are considerably smaller than the bounding velocities of elastic and plastic waves in the brittle materials themselves [5, 6]. Impacts can thus be considered as quasi-static indentations, where the indentation force is supplied by the deceleration of the particles.

Impacts can be classified in different regimes depending on the conditions. For an easy classification of erosion processes, it is illustrative to draw an erosion map showing the transition lines between the different erosion regimes as a function of particle size (R) and particle velocity (v). Hutchings [7] draws two separate maps; one for impacts that are purely elastic and one for predominantly plastic deformation. This chapter combines these maps into one, derives quantified relations for the transitions [8] and extends those to round-tipped non-spherical particles, as shown in Figure 3-1. Describing the particle geometry with a tip radius (r) differing from its particle size (R) enables to study the transition between spherical particles ($r/R = 1$) and sharp particles ($r/R = 0$).
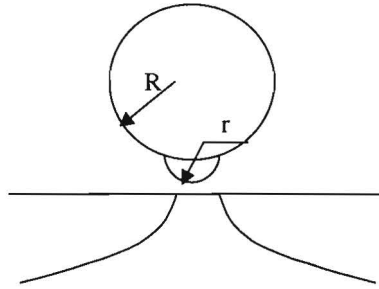
Figure 3-1: A cone crack beneath a round-tipped particle. R determines the particle size and r the contact radius of the particle.

Transition from elastic to plastic behaviour

The impacts are classified with respect to the dominant type of deformation caused by the impact: elastic impacts at small loads and plastic impacts at higher loads. When the mean indentation pressure ($P_{i,crit}$) equals the hardness of the material (H_t) the boundary between those classes is assumed to be reached.

$$P_{i,crit} = \frac{P}{\pi a^2} = H_t \tag{3.1}$$

where P is the indentation load and a the radius of the contact circle. An alternative way of defining the start of plasticity equates the maximal shear stress beneath the indentation to the material's yield stress results in a comparable value of critical indentation load ($P_{i, crit}$,[9]).

The radius of the contact circle can be found by Hertz's theory [10]

$$a^3 = \frac{3}{4}\frac{Pr}{E^*} \tag{3.2}$$

The parameter E^* is the contact modulus ($1/E^* = (1-v^2)/E + (1-v_p^2)/E_p$), with E the modulus of the target, E_p the modulus of the particle, and v and v_p the Poisson ratio of substrate and particle, respectively. The contact radius of the indenter is denoted by r. Combining the equations above gives an explicit relation for the indentation load at the plastic boundary (P_p):

$$P_p = (\pi H_t)^3 \left(\frac{3}{4}\frac{r}{E^*}\right)^2 \tag{3.3}$$

The indentation load during impact is generated by the inertia of the particle. The equivalent indentation load can be obtained from equating the kinetic energy of the particle to the (elastic) work done by the impact.

$$\frac{1}{2}mv^2 = \int_0^{\delta_{max}} P(\delta)d\delta \tag{3.4}$$

δ is the mutual approach of particle and substrate, which for a Hertzian indentation obeys $\delta = a^2/r$ [10, 11] with a the radius of contact. The parameter v and m are respectively the impact velocity of the particle and its mass ($= 4\pi/3\,\rho\,R^3$, with ρ the specific mass of the particle and R its radius (see Figure 3-1)). Using equation 3.2 and the relations above, equation 3.4 can be solved to find the maximal indentation depth δ_{max}.

$$\delta_{max} = \left(\frac{5\pi\rho\,v^2}{4E^*}\frac{R^3}{r^{1/2}}\right)^{2/5} \tag{3.5}$$

The maximum indentation load (P_m) can be obtained from equation 3.5 with use of equation 3.2 and the relation between indentation depth and contact radius mentioned above to find

$$P_m = \frac{1}{3}(4r^{1/2}E^*)^{2/5}(5\pi\rho R^3 v^2)^{3/5} \tag{3.6}$$

By equating the maximal indentation force (P_m) and the indentation load at the plastic boundary we obtain a critical velocity for plastic impacts $v_{crit,p}$

$$v_{crit,p} = \frac{9}{80}\sqrt{15}\pi^2\,\frac{H_t^{5/2}}{E^{*2}\rho^{1/2}}\left(\frac{r}{R}\right)^{3/2} \tag{3.7}$$

Note that for spherical particles ($r = R$) the particle size does not influence the critical velocity. The critical velocity decreases with r/R (for "sharper" particles).

Transition to cone cracking

With increasing indenter load at elastic impact the tensile stresses in the target surface just outside the contact circle will start opening surface flaws. These flaws grow together to a ring crack that is later extended to a cone crack. Auerbach's law gives the indenter load for which the crack starts developing [12].

$$P_c = \frac{9K_{Ic}^2 r}{16E^*\varphi_I^*}$$

(3.8)

where K_{Ic} is the fracture toughness of the target material and φ_I^* a proportionality constant determined empirically. Although φ_I^* is considered to be a constant, a significant scatter of values is found in the literature [12-14] $\varphi_I^*=1.6\times10^{-5}$, $\varphi_I^* = 5\times10^{-5}$ and $\varphi_I^*=8\times10^{-5}$. For the drawing of the erosion maps the value 8×10^{-5} is used [14].

Expressing equation 3.8 as a critical velocity for impacting particles using equation 3.6 we obtain

$$v_{crit,c} = \frac{9}{80}\sqrt{\frac{15}{\pi}} \frac{K_{Ic}^{5/3}}{E^{*7/6}\varphi_I^{*5/6}\rho^{1/2}R^{5/6}}\left(\frac{r}{R}\right)^{2/3}.$$

(3.9)

Note that the transition to cone cracking shifts to lower velocities with decreasing (r/R) ratio.

Plastic regime: transition to lateral/median and lateral cracks

Relations for the transition to lateral and radial cracks have been derived for the plastic impact regime in chapter 2 [4]. Although these relations were derived basically for sharp particles, the model predicts no influence of particle shape and should be applicable for spherical particles as well. The transition velocity can be derived from equation 2.14 to

$$v_{crit,l} = C \frac{E^{3/4}K_{Ic}^3}{H^{13/4}\rho^{1/2}R^{3/2}}.$$

(3.10)

The value of the pre-factor C is about 32 for the transition to radial cracks and about 105 for the transition to lateral cracks. In the erosion map these transition lines will be represented as two parallel lines.

The erosion map

The transition velocities (equations 3.7, 3.9 and 3.10) can be plotted against the particle size to construct an erosion map like Figure 3-2. It visualises the regimes

predicted by the models above. An elastic regime at low impact velocities with a cone crack regime increasing in size for large particles. At high impact velocities the area of plastic impact is found with transitions to radial and lateral crack patterns. In this area the spherical particles are expected to follow the rules derived in Chapter 2, i.e. they behave like sharp particles.
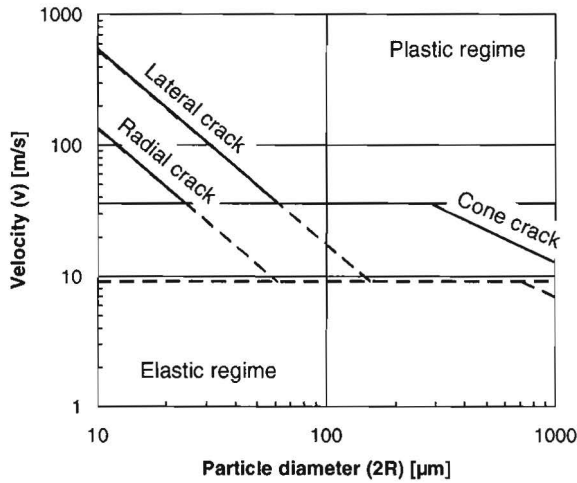
Figure 3-2: The theoretical erosion map for AF 45 glass. The solid lines are for spherical particles (r/R = 1). The dashed lines are calculated for rounded particles with r/R = 0.4.

This erosion map in Figure 3.2 illustrates the theoretical transformation of the map from spherical particles to sharp ones. At decreased roundness (r/R) the transition from elastic to plastic impact shifts to lower impact velocities, increasing the area where the particles behave "sharp". For sharp particles (r/R = 0) all impacts become plastic, resulting in a map with the lateral and radial transition lines as described earlier [8].

3.2.2 Experimental procedures

The experiments used two types of spherical particles: soda-lime spheres (Solvent) and ceramic spheres with a mean diameter from 46 to 484 μm (Zirblast, Sepr). The Zirblast ceramic particles contained 68% Zirconia and 32% "glassy phase". The size of the powders was measured by sedimentometry (Sedigraph 5100). The average particle sizes and material parameters are shown in Table 3-1. Figure 3-3 shows a characteristic SEM picture of the ceramic and the glass particles.

Two types of glass were used as targets: a borosilicate glass (AF45, Schott) and a soda-lime glass (Glaverbel). The material parameters of both substrates are given in Table 3-2.

The Zirblast particles were used on both the AF45 glass and the soda-lime glass. The soda-lime spheres were impacted on AF45 only.

Table 3-1: The properties of the erodents.

Zirblast		Soda-lime spheres	
Powder	Average size [μm]	Powder	Average size [μm]
B205	46.2	0-44 μm	37
B120	93.0	44-88 μm	66
B60	179		
B40	285		
B30	484		
Material properties			
Hardness	7-9 GPa	Hardness	5.6 GPa
Specific mass	3850 kg/m^3	Specific mass	2450-2550 kg/m^3
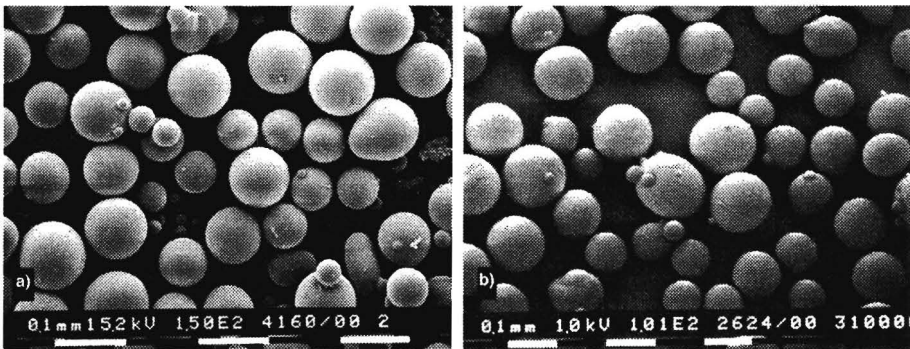
Figure 3-3: Sample of the shapes of the powders used a) glass spheres 44-88, b) Zirblast B120. Note the presence of satellite droplets and aspherical particles.

All experiments used a commercial abrasive jet machine (HP-1, Texas Airsonics, Corpus Christi, Texas, USA). The power-air mixture is fed from this machine by a tube to an alumina nozzle, 16 mm long with an inner diameter of 1.5 mm. The target substrate is attached to a substrate table, that scans below the fixed nozzle to prevent crater formation. During the experiments the particle velocity was

measured using a one-dimensional Laser-Doppler system (FlowLite and BSA, Dantec Measurement Technology A/S, Skovlunde, Danmark).

To prevent interaction between impact sites, a low powder flux was used combined with a very high scan rate of the substrate table. The sample was scanned only once. Five representative photographs were taken from the surface of each sample using a microscope. Two individuals assessed the series of photographs separately to classify the individual impact sites, obtaining comparable results.

Table 3-2: The material parameters of the target materials used. For a remark on the measurement techniques used see section 2.4.3.

			Soda lime	AF 45
Hardness	H	[GPa]	5.2 ± 0.13	5.13 ± 0.09
Modulus	E	[GPa]	73.4 ± 0.18	66.1 ± 0.12
Fracture toughness	K_{Ic}	[MPa·m$^{1/2}$]	0.86 ± 0.14	0.89 ± 0.12
Poisson ratio	ν	[-]	0.227 ± 0.0003	0.241 ± 0.0007
Specific mass	ρ	[kg/m^3]	2500 ± 3	2727 ± 2

3.2.3 Results

Classification of the impact sites resulted in tables with relative occurrence of the types of impacts. The visible impact sites were classified in four categories: sites with plastic deformation only, sites with visible radial/median crack patterns, sites with visible lateral cracks and sites with visible ring or cone cracks. Please note that elastic impacts do not leave traces, which makes the data somewhat difficult to interpret.

As an example, Figure 3-4 shows the relative occurrence of the four categories for one powder as a function of particle velocity. Three transitions are visible. At low velocities almost all impact sites visible are plastic. As the velocity increases, radial/median cracks start to develop and at a slightly higher velocity the number of lateral cracks increase. At the high velocities ring/cone cracks start to appear.

The broad transitions visible in the data are to be expected, considering the width of the distribution of both particle size and velocity in each experiment. Although the value is rather arbitrary, the velocity value at which the presence of a specific crack pattern exceeds the 10 percent is used as the transition value to that crack pattern.

The transition lines are drawn in the theoretical erosion maps as derived above. The resulting charts are shown in Figure 3-5 for the two target materials impacted by Zirblast beads. The broken lines represent the transition lines found from theory. The solid lines show the transition lines found experimentally. The markers

on these lines indicate the measurement points. The transition from elastic to plastic is placed at the lowest measured velocity, since sites with plastic deformation were found on all samples impacted by Zirblast beads.
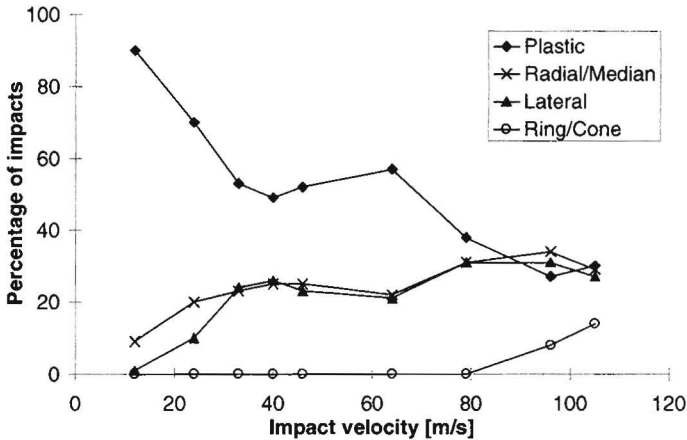
Figure 3-4: The relative occurrence of types of impact sites for Zirblast B60 (179 μm) on AF 45 substrates. The sum of the four types is 100%.

The single-impact experiments with the soda-lime spheres on AF45 give the same global results, except that the threshold velocities are considerably higher than for the Zirblast particles. They show no transition to cone cracks. Since data is only available for two sizes of particles, no erosion map is drawn. Following the procedure above we find a transition to radial cracks at 90 m/s for the smaller particles and 50 m/s for the larger ones. For the transition to lateral cracks the values are 200 m/s and 89 m/s, respectively.

3.2.4 Discussion

As Figure 3-5 shows, all predicted transition lines are found experimentally for the two glasses. However, some differences can be observed between the theoretical and experimental erosion maps. The shift to low impact velocities of the elastic–plastic transitions and the shift to higher velocities for both target materials of the transition to cone cracking are remarkable. Furthermore, a clear difference can be seen between the slopes of the transition to lateral/radial cracks of the two glasses. We will address these subjects separately.
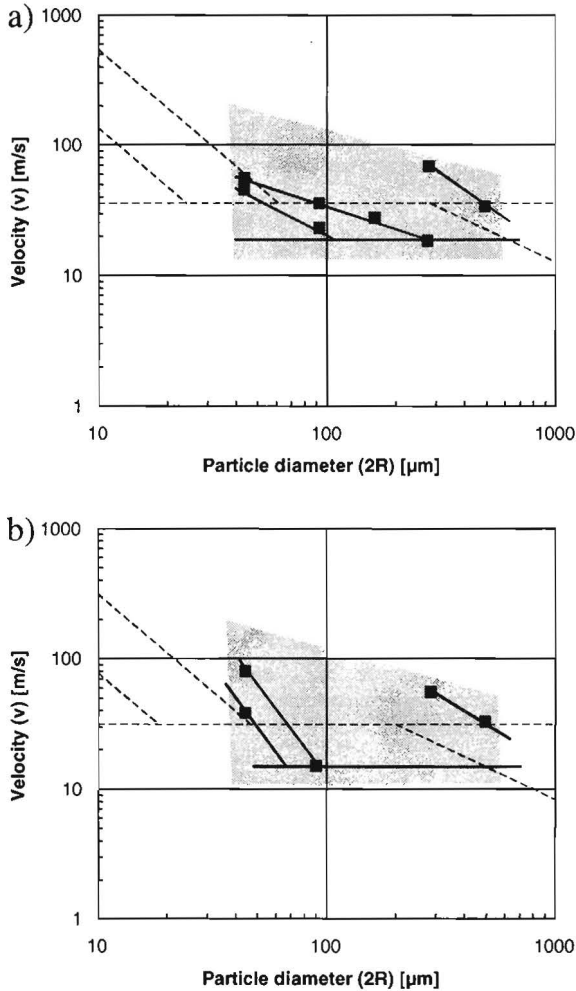
Figure 3-5: The erosion maps for Zirblast particles on (a) AF45 [8] and (b) soda-lime glass. The broken lines represent the theoretical predictions from section 2. The solid lines are the experimentally found transitions. The shaded area illustrates the experimental window.

The elastic–plastic transition

In an earlier paper [8] the shift of the AF45 transition to lower velocities has been attributed to the compaction of the open structure of the borosilicate glass. Figure 3-5, however, shows the same shift being present for soda-lime glass. Since soda-lime glass does not have an open structure, this explanation is not satisfactory.

A study of the impact sites shows a clear difference in the size of the impact marks on the surface, as Figure 3-6 illustrates. The size of the plastic indentations observed is generally of the order of 15 μm, whereas the ring cracks are between 40 and 70 μm.

The plastic indentations found experimentally are smaller than expected for spherical particles. The theoretical contact diameter in the situation in Figure 3-6a (B60, 136 m/s) is, for example, 75 μm, while the picture shows a plastic indentation of less than 20 μm. The ring crack in Figure 3-6b, however, compares reasonably with the calculated contact zone of 40 μm (B120, 247 m/s).
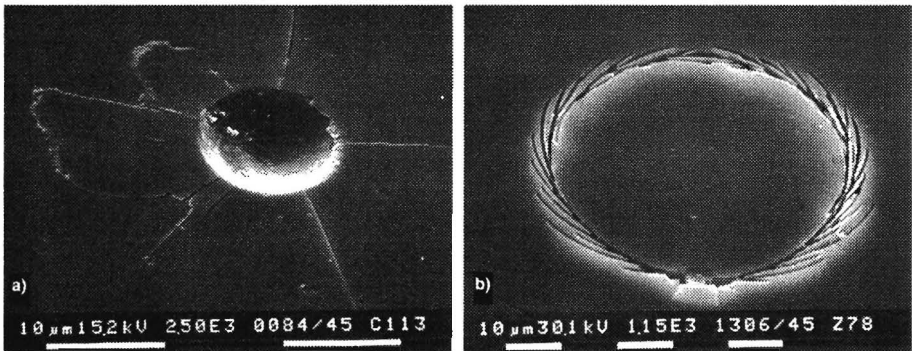
Figure 3-6: Sample photographs of lateral/radial crack pattern (a) and a ring-crack pattern (b) beneath an impact site of Zirblast particles. Note the difference in impact size.

Considering the presence of satellite droplets on the particles, it must be concluded that the plastic indentation sites are usually generated by the protrusions on the particles hitting the surface. As equation 3.7 shows, a ratio of curvature at the contact zone and particle radius (r/R) of 1/5 is needed for shifting the elastic–plastic transition a factor 10 to lower velocities. While most particles bounce off the surface elastically, without leaving a trace, the particles hitting the surface with the protrusion will leave visible damage.

Ring and cone cracks
As discussed above, the sizes of the ring cracks observed suggest that they are very likely caused by the impact of the spherical particle itself. An explanation is needed for the difference between the experimentally observed transitions and the theoretical ones.

The higher velocity needed experimentally to induce cone cracks than expected theoretically, might be a combination of a size effect of the Hertzian indent and the surface flaw distribution. Since the size of the surface under tensile stress is limited and scales linearly with particle size, smaller indentations have less chance of finding a large flaw in the strained area and will result generally in a higher transition to cone cracking [15].

The surface state (flaw distribution) itself might also be a possible source for the discrepancy between theory and experiment. The sensitivity of the transition to the surface flaw distribution is represented in the range of values that is found in the literature for the proportionality constant in Auerbach's law [12-14] or in the range of indentation forces before a cone crack is initiated [16]. The experimentally observed transitions are well within the range of the constants found in the literature, as Figure 3-7 shows.
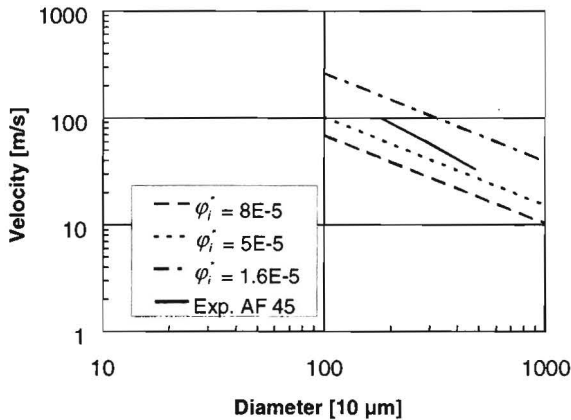
Figure 3-7: The transition to cone cracking derived for different values of φ_l^*.

It remains to observe that cone cracks are initiated well above the theoretical transition to plastic impact. Once plastic deformation is well developed, one expects that the compressive stresses would prevent the initiation of ring cracks. The experimental data, however, does not support this image. It is unclear whether the experimental observation is an effect of the distribution of particle sizes and shapes or it is connected with an omission in the modelling.

Although cone cracks may occur for open-structured glasses around sharp indenters [17], this cannot be used as an explanation since the same effect is visible for the soda-lime glass (see the discussion in section 2.6.2).

Radial and lateral cracks

For soda-lime glass the transition to lateral/radial cracks is found experimentally at about the same position as the theory predicted. The slope of the lines seems to be slightly higher, but this is not significant, considering the limited number of experiments.

The transition lines in the AF 45 erosion map show a considerably lower slope. This might originate in the anomalous behaviour of the borosilicate glass. The compaction of the target under impact reduces the stresses outside the plastic zone, thereby postponing the initiation of lateral and radial cracks [18].

3.3   Erosion and surface roughness

3.3.1   Theory

For an industrial erosion process, the velocity of the erosion and the resulting surface roughness are important parameters. In the case of sharp particles, quantitative equations were derived for the two parameters. This theory based on plastic indentations with lateral cracks is in good qualitative agreement with experiments (Chapter 2, [4]).

The theory behind the model shows that the shape of the particle is not important, which should make the results applicable to spherical particles in the lateral/radial crack regime as well. Since, according to the model, the erosion is governed by the kinetic energy, the erosion efficiency is defined as a measure for the velocity of the erosion (equation 2.18). The erosion efficiency is defined as the eroded mass of substrate per amount of kinetic energy of the erodent [kg/J]. In simplified form equation 2.18 reads

$$E_{eff} \approx 2.7 \cdot 10^{-2} \frac{\rho_t E^{5/4}}{H^{5/2} K_{Ic}} \left(2.75 H^{13/12} U_{kin}^{1/6} - 14.7 K_{Ic} E^{1/4}\right) \qquad (3.11)$$

where U_{kin} denotes the kinetic energy of an individual particle ($U_{kin} = 2/3\pi R^3 \rho v^2$). The often-used erosion rate E_r is related to the erosion efficiency by equation 2.17:

$$E_r = E_{eff} \frac{v^2}{2}. \qquad (3.12)$$

For the surface roughness R_a the equation 2.19 has been derived, which reads approximately

$$R_a \approx 0.12 \left(\frac{E}{H}\right)^{1/2} \left(\frac{U_{kin}}{H}\right)^{1/3} \qquad (3.13)$$

The equations given above have been derived for sharp particles in the lateral/radial crack regime.

In the elastic impact regime using the same method, relations can be derived for erosion and surface roughness originating from the forming of cone cracks. For the erosion rate an estimate of the volume of material over an individual cone crack is needed. It has been assumed that each particle impact removes that volume, so the total erosion is found by just adding the contributions.
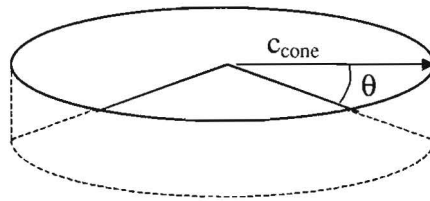
Figure 3-8: The schematic representation of a single particle impact site used in the cone-crack model.

Here the volume removed per particle V_i is estimated to be equal to the volume above the cone crack, approximated as sketched in Figure 3-8. This volume equals

$$V_i = \frac{2}{3}\pi c_{cone}^3 \tan\theta \qquad (3.14)$$

with θ being the propagation angle of the cone cracks. We will use $\theta = 14°$ as is obtained for quasi-static indentation in soda-lime glass, although there is evidence suggesting that the angle depends on the impact velocity and might be as large as 40° [19, 20] by loading rate effects, which we will neglect in this chapter.
The length of the cone crack c_{cone} is derived from indentation work [12]

$$\frac{P}{c_{cone}^{3/2}} = \beta_R K_{Ic} \qquad (3.15)$$

where P is the indentation load and β_R is a constant, usually determined experimentally. Wiederhorn and Lawn [12] give $\beta_R = 28$ for soda-lime glass. Expressing the indentation load in elastic impact parameters, the equation for the erosion rate E_r can be derived from equations 3.14 and 3.15, resulting in:

$$E_{r,cone} \approx 4.8 \frac{\rho^{1/5} r^{3/5} R^{2/5} E^{*4/5} v^{12/5}}{\beta_R^2 K_{Ic}^2} \rho_t \qquad (3.16)$$

with ρ and ρ_t being the specific mass of the particles and target, respectively.

The surface roughness R_a is calculated over one impact site in a similar way as for the lateral crack system [4] by integrating the deviation of the surface (y) from its average height (y_0) over one impact site with $A = \pi\, c_{\text{cone}}^2$ (see Figure 3-8).

$$R_a = \frac{1}{A} \int_A |y - y_0|\, dA \tag{3.17}$$

This results in

$$R_a \approx 0.10 \left(\frac{r}{R}\right)^{2/15} \frac{\rho^{2/5} R^{4/3} E^{*4/15}}{K_{IC}^{2/3}} v^{4/5} \tag{3.18}$$

The procedure of computing the surface roughness over a single impact site in fact assumes the surface to be fully covered with identical sites. As discussed in section 2.3.3 the surface roughness obtained this way, may be considered as a moderate estimate since crack interaction might both increase and decrease the surface roughness.

The equations have also been derived for the geometry of a dug-in truncated cone, with the truncated top modelling the finite size of the ring crack. Although the equations become considerably more complicated, the general behaviour is similar to the model described above, so the extended model is omitted.

3.3.2   Experimental procedures

The erosion experiments use the same equipment as the single impact experiments, except that the particle flux is higher, the scan rate is lower and each sample is scanned multiple times. Each sample received about 60 grams of powder at an eroded surface of about 10 cm^2. The particle flux is measured by monitoring the weight loss of the abrasive jet machine by placing it on a balance (Mettler PM 30-K). The weight loss of the sample was measured by weighing the sample before and after the experiment on a Sartorius analytical balance. Each experiment was repeated at least three times to ensure the reproducibility of the process. The results presented here represent the average values of the repeated experiments.

The glass beads used showed slight size degradation from 37 to 35 µm at high impact velocities, as was verified with sedimentometry (Sedigraph 5100). For the Zirblast particles no degradation could be measured.

The surface roughness of the eroded substrates was measured using an Alpha-Step profilometer equipped with a stylus with a top radius of 12.5 µm. The scans were filtered according to the norm DIN 4777.

All experiments in this section use the AF45 glass as target. The types of particles used are the same as those of the single impact experiments (see section 3.2).

3.3.3 Results

Figure 3-9 and Figure 3-10 combine the erosion results of the Zirblast beads and the glass spheres. Figure 3-9 plots the results as the erosion efficiency against kinetic energy of the individual particles. As has been shown [4], this results in a master curve when the lateral crack model is applicable. For comparison, the experimental data for hard sharp particles [4] are shown as points. In contradiction to the data from the sharp particles, the data for the different sizes of round particles do not coincide, the larger particles giving lower erosion efficiency at the same energy.

Figure 3-10 plots the same data as the experimental erosion rate against that predicted by the cone-crack model (equation 3.16). When this model is applicable the data should lay on the dashed line in the figure. Although the curves of the different particle sizes are closer together, they do not coincide. Note that the relative position of the two particle sizes has changed.
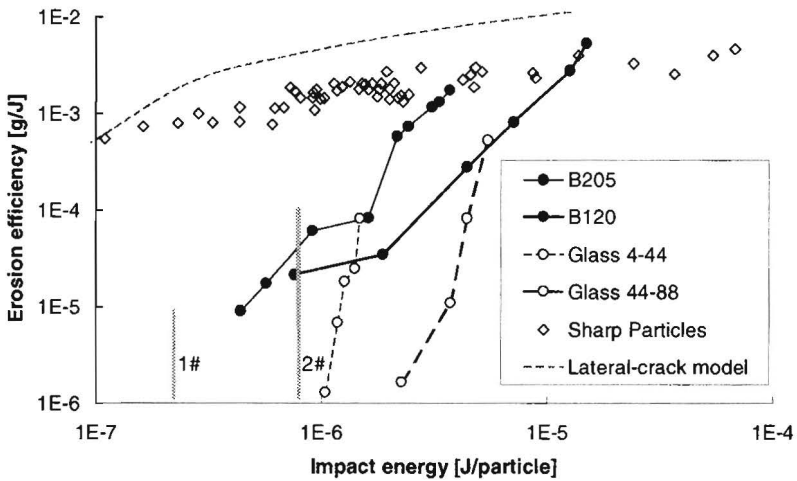
Figure 3-9: The erosion efficiency of all measured spherical powders. The points are the experimental data for hard sharp particles [4] and the dotted line is the theoretical model (equation 3.11). The markers 1# and 2# denote the transition to lateral cracks observed in single impact experiments for B205 and B120, respectively.
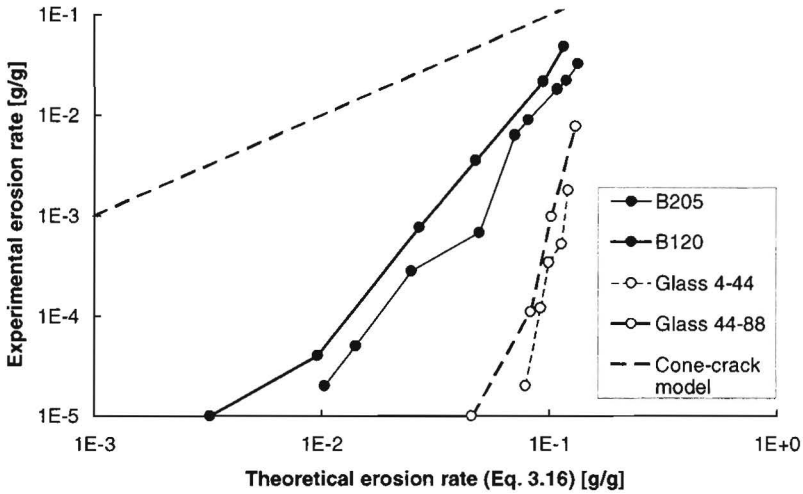
Figure 3-10: The measured erosion rate for all spherical particles plotted against the one calculated with the cone-crack model (equation 3.16). The dotted line sketches the model prediction.
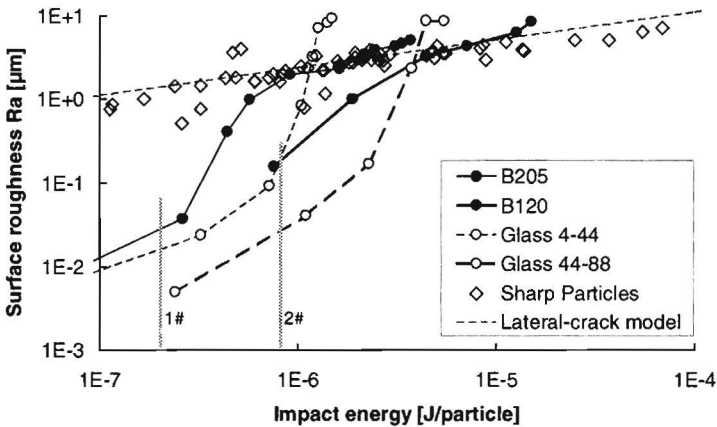
Figure 3-11: The measured surface roughness of all spherical particles plotted against their kinetic energy. The points represent data from sharp particles [4], the dotted line is the lateral-crack model (equation 3.11). The markers 1# and 2# denote the transition to lateral cracks observed in single impact experiments for B205 and B120, respectively.
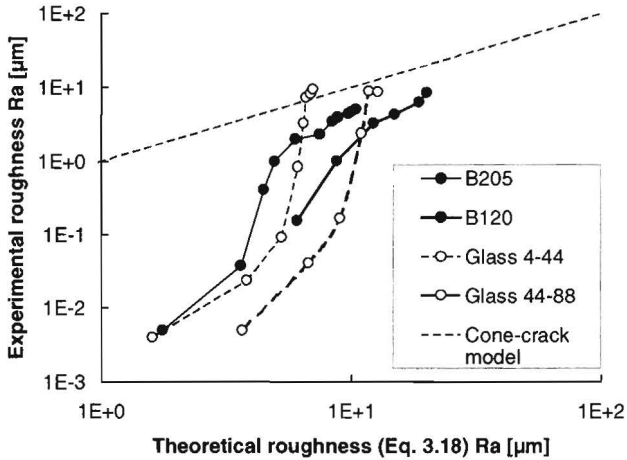
Figure 3-12: The measured surface roughness of all spherical particles plotted against the roughness calculated with the cone-crack model (equation 3.18). The dotted line gives the perfect correlation between experiment and model.

Figure 3-11 and Figure 3-12 plot the surface roughness data in the same way. In Figure 3-11 the data is plotted against the kinetic energy of the particles. As a reference it includes again the data for sharp particles [4] and the lateral erosion model (equation 3.13). Figure 3-12 plots the measured surface roughness against the one predicted by the cone-crack model (equation 3.18). The dashed line depicts the correlation between theory and experiment. The surface roughness of the non-eroded samples is about $R_a = 0.005$ µm.

3.3.4   Discussion

As expected from the erosion maps, both the erosion efficiency (rate) and the surface roughness data in the figures (3.9-3.12) show a regime at low impact velocities where erosion and surface roughness are small. Being below the fracture thresholds, the elastic impacts in this regime should introduce neither damage nor plastic deformation and would lead to no change in surface roughness or erosion.

At increased energy, first the surface roughness increases and later also the erosion efficiency. This is expected since the damage of a few particles would already result in increased roughness, while their erosion is still negligible. The "softer" glass particles exhibit a higher threshold, probably since the stresses beneath these particles are reduced by the deformation of the particles themselves. Above this

threshold the erosion of the glass beads exhibit a steeper slope than the "hard" Zirblast particles. The reason for this is not understood.

At high impact velocities the glass particles give unexpected results by inducing a considerably higher surface roughness than the ceramic particles and seem even to give higher erosion. The slope of all spherical powders suggests that surface roughness and erosion efficiency at high impact velocities will be larger than for sharp particles.

The models derived in section 3.4.1 do not predict such behaviour. When the experiments were to follow one of the models the data at high velocities should coincide with the model either in the Figure 3-9 and Figure 3-11 or in Figure 3-10 and Figure 3-12. These figures, however, show that none of the models predict the measured erosion or the resulting surface roughness correctly.

So, although the erosion maps for single impacts do predict the regimes reasonably well, the models for process parameters like erosion efficiency and surface roughness fail. Although the effect of non-constant cone crack angle [20] and the anomalous behaviour of the AF45 (see the discussion in section 2.6.2) may play a role in this deviation, it is not expected that they dominate the gap between theory and experiment. A closer look at the eroded surfaces gives an indication of the origin of this failure.
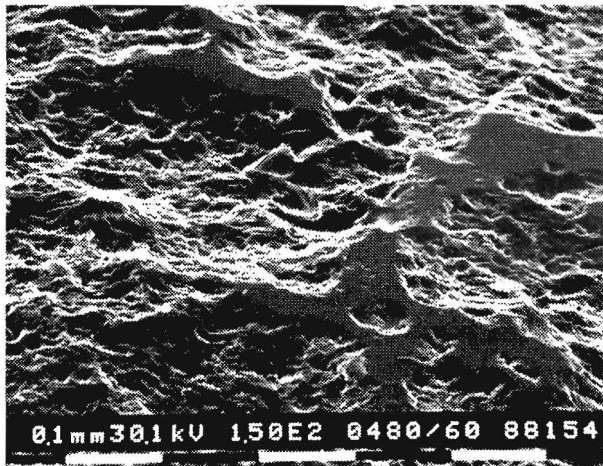
Figure 3-13: SEM photograph of a glass surface (AF45) eroded with glass spheres (44 - 88 µm, 154 m/s) showing eroded surface with apparently non-eroded "islands".

Figure 3-13 shows a characteristic image of an eroded surface with spherical glass particles. Although large parts of the surface have been affected by erosion, "islands" with the original glass surface still exist. The samples eroded with Zirblast particles exhibit a similar island structure with the island surface showing more signs of plastic impacts and the "cliffs" surrounding the islands being less high. The island phenomenon deviates considerably from samples eroded with sharp particles, where the surface is homogeneously eroded after a far shorter time of erosion. The presence of these islands illustrates that the erosion process did not reach a "steady state". Although an initiation phase is known for erosion of glass by glass beads [21], it is unexpected after erosion of 6 g/cm^2. The steep slope in erosion and roughness might be caused by the start-up effect of the erosion process.
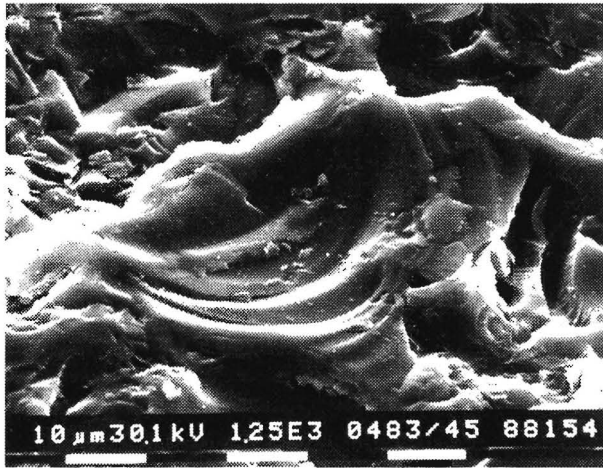
Figure 3-14: Detail SEM photograph of a glass surface eroded with glass spheres (44 – 88 µm, 154 m/s).

Figure 3-14 zooms in at the fracture surface on a sample eroded with glass spheres (44-88 µm), evidently originating from the removal of one chip of material. The stepwise fracture surface is striking. It clearly shows that this surface was not made by a single impact, but might have grown over a number of consecutive impacts. The size of the total structure is also far larger then the fracture length expected based on the particles involved. The Zirblast eroded samples show similar marks, although less and less obvious.

The observations point towards a basic flaw in the model. They assume the absence of interaction between impacts and damage in the surface. Although very successful for sharp particles [4], Figure 3-13 and Figure 3-14 show clear signs of

interaction between particles and damage present in the surface. The erosion process by spherical particles consists most likely of initiation of a crack, growth of this crack by consecutive impacts and, finally, removal of a large chip of material.

3.4 General discussion and conclusion

This chapter has derived quantitative relations for the transitions between the different regimes in erosion of spherical particles as well as for process parameters like surface roughness and erosion efficiency and rate. Erosion maps have been constructed with the transition equations for both soda-lime and borosilicate glass (AF45). Besides giving an overview of the position of the different erosion regimes, the erosion map for rounded particles proposes a gradual transition from angular particle to spherical particles, where the size of the elastic impact regime decreases while the plastic regime increases.

Single-impact experiments confirm the existence of the impact regimes derived theoretically. The locations of the transitions found experimentally differ from the ones obtained theoretically. The experimental elastic–plastic transition is found at lower impact velocities than expected. This is attributed to the presence of protrusions on the particles. The high values of the transition to cone cracking are probably caused by the surface of the glass samples having relative few, small flaws. The high value of the transition found experimentally is, however, within the range of data reported in the literature. The transition to lateral/radial cracks differs for the two substrates, where the soda-lime glass data is in reasonable agreement with theory and the AF45 data shows a considerably lower slope. This difference is attributed to the compaction behaviour of the borosilicate glass.

The erosion experiments confirm the existence of a regime at low impact energies, where particles do not inflict damage to the targets. After crossing this energy threshold (for the onset of fracture), both surface roughness and erosion rate rise steeply with increasing energy, at high energies surpassing the data available for sharp particles in surface roughness and presumably also in erosion efficiency. The "softer" glass particles exhibit a higher threshold to erosion, but at high impact speeds, also a higher surface roughness.

The threshold energies for lateral cracking found in the single-impact experiments of the Zirblast particles are included as markers in Figure 3-9 and Figure 3-11. Figure 3-11 shows that they correlate best with the start of the increase in surface roughness. This is expected since damage induced by a few particles will influence surface roughness, while the erosion threshold will be at higher energies, where most particles generate damage.

The two erosion models used in this paper fail in describing the process most likely since they do not incorporate interaction between impacts and the damage present

in the substrate. A model for erosion of spherical particles would probably need a three-step approach, incorporating the probability of crack initiation, the propagation of cracks by the stress field of successive impacts and removing chips by crack interaction.

The failure of the multiple impact models shows also that the proposed transition from sharp to spherical particle impact as presented in the erosion map (Figure 3-2) is not correct. Which poses the question how the transition will take place? Or which rounded particle will behave like an angular particle and which like a spherical particle.

Two experiments might be useful to supplement the findings in this paper. Single-impact experiments with exact spherical particles would increase the accuracy of the validation of the erosion maps, especially the elastic–plastic transition. Erosion experiments of polished substrates with some predefined flaws might confirm the importance of crack initiation in the erosion process.

3.5   List of symbols

C	Proportionality constant for the transition to lateral/radial cracks, Equation 3.10.
E	The Young's modulus of the substrate [Pa], below Equation 3.2.
E_{eff}	The erosion efficiency (mass of removed substrate per amount of kinetic energy of erodent used) [g/J], Equation 3.11 and Equation 2.18.
E_p	The Young's modulus of the particle [Pa], below Equation 3.2.
$E_{r, cone}$	The erosion rate (mass of removed substrate per mass of erodent used) according to cone crack model [g/J], Equation 3.16.
E_r	The erosion rate (mass of removed substrate per mass of erodent used) according to lateral crack model [g/J], Equation 3.12 and Equation 2.17.
E^*	The contact modulus of the Hertzian contact [Pa], Equation 3.2.
H_t	The hardness of the substrate [Pa], Equation 3.1.
K_{Ic}	The fracture toughness of the substrate [Pa m$^{1/2}$], Equation 3.8.
P	The indentation force [N], Equation 3.1.
P_c	The indentation force at the transition to cone cracks [N], Equation 3.8.
$P_{i.crit}$	The mean indentation pressure for plastic for the transition to plasticity [Pa], Equation 3.1.
P_m	The maximal indentation load corresponding to particle impact [N], Equation 3.6.
P_p	The indentation force at the transition to plasticity [N], Equation 3.3.
R	The size (radius) of the spherical particle [m], Figure 3.1.
U_{kin}	The kinetic energy of a particle at impact [J], Equation 3.11.
V_i	The removed volume per cone crack event [m^3], Equation 3.14.
a	The Hertz contact radius [m], Equation 3.1.
c_{cone}	The length of the cone crack [m], Equation 3.14.

r	The contact radius of a-spherical particle ($r = R$ for a spherical particle) [m], Figure 3.1.
m	The mass of an impacting particle [kg], Equation 3.4.
v	The impact velocity of a particle [m/s], Equation 3.4.
$v_{crit,c}$	The critical velocity for the transition to cone cracks [m/s], Equation 3.9.
$v_{crit,l}$	The critical velocity for the transition to lateral/radial cracks [m/s], Equation 3.10.
$v_{crit,p}$	The critical velocity for the transition to plastic impact [m/s], Equation 3.7.
y_0	The average surface position for surface roughness determination [m], Equation 3.17.
β_R	Proportionality constant of the cone crack length [-], Equation 3.15.
δ	The indentation depth [m], Equation 3.4.
δ_{max}	The maximal indentation depth at impact [m], Equation 3.4.
θ	The propagation angle of the cone crack [°], Equation 3.14, Figure 3.8.
v	The Poisson ratio of the substrate [-], below Equation 3.2.
v_p	The Poisson ratio of the particle [-], below Equation 3.2.
ρ_t	The specific mass of the substrate [kg/m^3], Equation 3.11.
ρ	The specific mass of the particle [kg/m^3], Equation 3.5.
φ_t^*	Dimensionless constant for the cone crack initiation [-], Equation 3.8.

3.6 Literature

1   I.M. Hutchings, *Transitions, threshold effects and erosion maps*, Key Eng. Mat. 71 (1992) 75-92.

2   M. Buijs, *Erosion of glass modelled by Indentation Theory*, J. Am. Ceram. Soc., 77 no 6 (1994) 1676-1678.

3   A.G. Evans, M.E. Gulden, M. Rosenblat, *Impact damage in brittle materials in the elastic-plastic response regime*, Proc. Roy. Soc. Lond. A361 (1978) 343-365.

4   P.J. Slikkerveer, P.C.P. Bouten, F.H. in 't Veld, H. Scholten, *Erosion and damage by sharp particles*, Wear 217 (1998) 237-250.

5   A.E.H. Love, *A treatise on the mathematical theory of elasticity*, Cambridge University Press (1952).

6   S.C. Hunter, J. Mech. Phys. Solids 5 (1956) 162.

7   I.M. Hutchings, *Ductile-brittle transitions and wear maps for the erosion and abrasion of brittle materials*, J. Phys. D.: Appl. Phys. 25 (1992) A212-A221.

8   M.A. Verspui, P.J. Slikkerveer, G.J.E. Skerka, I. Oomen, G. de With, *Validation of the erosion map for spherical particle impacts on glass,* Wear 215 (1998) 77-82.

9   K.L. Johnson, *Contact Mechanics*, Cambridge University Press (1989).

10 S.P. Timoshenko, J.N. Goodier, *Theory of elasticity*, Int. 3nd edn. McGraw-Hill Int. Ed., Engineering Mechanics Series London (1970).

11 C.G. Knight, M.V. Swain, M.M. Chaudhri, *Impact of small steel spheres on glass surfaces*, J. Mater. Sci. 12 (1997) 1573-1586.

12 S.M. Wiederhorn, B.R. Lawn, *Strength degradation of glass resulting from impact with spheres*, J. Am. Ceram. Soc. 60, no 9-10 (1977) 451-458.

13 B.R. Lawn, R. Wilshaw, *Review indentation fracture: principles and applications*, J. Mater. Sci. 10 (1975) 1049-1081.

14 K. Peter, *Sprödbruch und Mikroplastizität von Glas in Eindrucksversuchen*, Glastechn. Ber. (1964) 333-345.

15 P.D.Warren, D.A. Hills, S.G. Roberts, *Influence of surface cracks on Hertzian fracture*, J. Hard Mater. 5 (1994) 213-227.

16 H. Conrad, M.K. Keshavan, G.A. Sargent, *Herzian fracture of Pyrex glass under quasi static loading conditions*, J. Mater. Sci. 14 (1979) 1473-1494.

17 J.T. Hagan, *Cone cracks around Vickers indentations in fused silica glass*, J. Mater. Sci. 14 (1979) 462-466.

18 R.F.Cook, G.M. Pharr, *Direct Observations and Analysis of Indentation Cracking in Glasses*, J. Am. Ceram. Soc. 73, no 4 (1990) 787-817.

19 Q. Sun, J.E. Field, *Spherical project impact on aluminas,* Proc. Int. Symp. on Intense Dynamic Loading and its Effects, Chendu, China, June 9-12 (1992).

20 J.E. Field, Q.Sun, D. Townsend, *Ballistic impact on ceramics*, Inst. Phys. Conf. Ser. 102, 7 (1989) 387-394.

21 P.K. Mehrotra, G.A. Sargent, H. Conrad, *A computer simulation of the time dependence of erosion of Pyrex glass by glass beads*, J. Mater. Sci. 17 (1982) 1049-1058.

4 Erosion and damage at oblique impact

The previous chapters considered the mechanism of erosion at normal impact for hard angular and spherical particles, respectively. In many circumstances, however, abrasive particles will hit the target at an oblique angle. This is for example the case for aircraft windows or bends in pneumatical transport tubes where the air stream is not normal to the surface. As chapter 5 will show, oblique impact is also important for powder blasting of masked substrates, even when the air jet is perpendicular to the surface.

To assist the development of a model for the evolution of shapes in patterned erosion in the next chapter, this chapter studies the erosion process of hard angular particles at oblique impact. It investigates experimentally the way the erosion rate, the surface roughness and strength vary with the angle of impact. Moreover it attempts to measure the rebound characteristics of particles, like rebound velocity and angle.

4.1 Introduction

The change of erosion rate with angle of incidence depends on the deformation mechanism of the substrate. Ductile materials show maximal erosion at glancing impact, while brittle materials display a maximum at normal impact. Figure 4-1 sketches the global shape of the curves. The curves, however, are not to scale; the erosion rate of brittle materials is generally an order of magnitude higher then that of ductile materials. Elastomeric materials - to be discussed in chapter 6 - show an angle-dependence similar to ductile materials. In this chapter we focus on brittle substrates, more specifically on the erosion process of glass with an alumina particles.
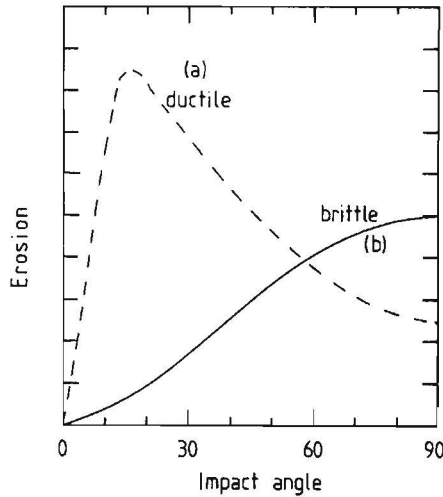
Figure 4-1: Schematic curves representing the erosion as function of angle of incidence for ductile (a) and brittle materials (b)[1].

As stated in chapter 2, the erosion rate (E) of brittle materials can be modelled by the relation $E_r \propto v^k$ where v is the particle velocity and its power k approaches 7/3 at the limit of high impact speeds. At oblique impact a successful empirical relation can be obtained by replacing the impact velocity by $v \sin(\theta)$ with θ the angle of incidence [2, 3]. This is illustrated by experimental data of Morrison et al. [4] who plotted the erosion rate against $v \sin(\theta)$ at various impact angles showing a good correlation. Sheldon [5] shows a good correlation between $\sin(\theta)$ and oblique erosion for various brittle materials like glass, alumina and graphite. In an early erosion model Bitter [6] already included this angle dependence.

The $\sin(\theta)$-relation is remarkably successful, although the experiments start to deviate from it at small impact angles. They show more erosion that the relation predicts [3, 4]. This additional erosion is attributed to ductile mechanisms caused by the tangential component of the velocity [7, 8]. Ibrahim et al. [9] use a special rotating-disk erosion set-up to show that the $v \sin(\theta)$ correlation does hold when the motion of the particles along the substrate surface is compensated for in the experimental set-up.

Single impact studies with sharp particles point to a possible second cause for the deviation at glancing impact. At low impact angles non-symmetrical lateral cracks patterns are generated. Ballout et al. [10] find non-symmetrical lateral crack patterns at angles below 30 degrees. Srinivasan and Scattergood [11] show similar results but give a limiting angle of 20 degrees. In their experiments they encounter no signs of plastic deformation.

For strength degradation of glass the $\sin(\theta)$-rule is also well-known. Wiederhorn et al. [12] for example show that only the normal component of the impact velocity is effective in providing a driving force for the forming of strength degrading micro-cracks.

This chapter verifies the suggested description of the erosion at oblique angles for glass eroded with alumina particles. In analogy with chapter 2 [13], we will study the effect of impact angle on erosion rate, roughness of the eroded surface and strength degradation of the eroded surfaces. Furthermore we will present the results of a first attempt to measure the rebound behaviour of the particles.

4.2 Experimental

Erosion measurements
The erosion rate experiments are performed using a Texas Airsonic HP-1 abrasive jet machine with 29-µm alumina powder (Starck Edelkorund F320). The nozzle with a diameter of 1.5 mm in this set-up scans over the glass substrates (Schott AF45) to prevent crater formation. The scan movement is adjusted in such a way that all particles leaving the jet hit the substrate. For each data point four samples of $50\times50\times2$ mm^3 are used, each eroded with at least 50 grams of abrasive powder to obtain a reproducibility of the erosion rate within 2% of value. The impact angle is varied from normal impact to glancing (15 degrees) in steps of 15 degrees.

The surface roughness is measured with an Alpha Step 200 surface profilometer using a stylus with a tip radius of 12.5 µm. Although this rather large tip radius

might fail to record some of the finer details of the surface structure, a comparison with experiments performed using a 5 μm tip radius showed this effect to be within the normal scatter of roughness measurements.

The profile data of this instrument are collected on a personal computer where they are filtered according to the norm DIN 4777. The measurement procedures comply with ISO 4288. All surface-roughness measurements use a scanning length of 10 mm and the roughness is determined for every sample in both the direction of the oblique impact (x direction, see Figure 4-2) and perpendicular to it (y direction).
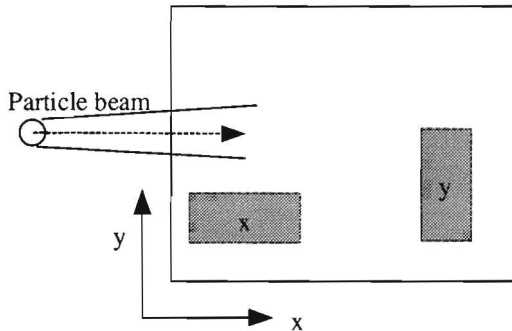
Figure 4-2: Definition of the sample directions with respect of the impact direction.

A one-dimensional Laser-Doppler measurement system (LDA, Dantec BSA and Flowlite) measures the velocity of the particles in the jet during the erosion tests. Using a fixed nozzle and a moving substrate in the erosion set-up enables this.

Rebound measurements

The one-dimensional Laser–Doppler system sets severe limitations to the measurement of rebound velocity. Although it is capable of identifying positive and negative velocities, it is not able to distinguish the incoming particle beam from the rebounding one near the target surface where the beams intersect. Measuring one velocity component at a time, the vertical velocity of the particles of the two beams could be separated by their direction. The wide velocity distribution and the limited difference in horizontal velocity between the two beams make separation of this component impossible.

The velocities of the incident and rebounding beam must therefore be measured outside the intersection of the two beams. To obtain an estimate of the rebound velocity and angle, the horizontal and vertical velocity components (x and z, Figure 4-3) are measured separately along a line through the centre of the jet at a height of 16-20 mm above the substrate surface. To limit the travelling distance of the

particles at the lowest impact angle (15 degrees), the velocity components were measured at two vertical lines at both sides of the beam intersection. Figure 4-3 illustrates the two variants in the measuring method.
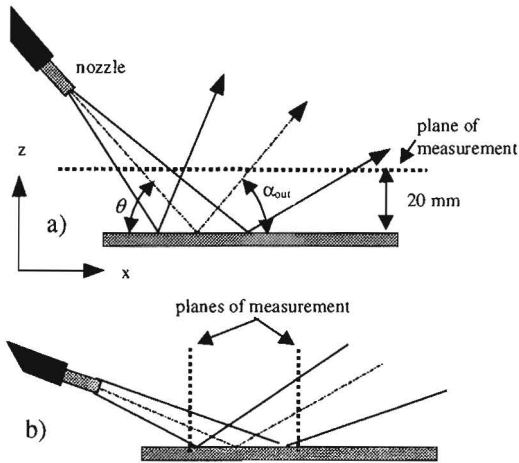
Figure 4-3: Schematic drawing of rebound velocity measurement technique. The dotted lines show the lines along which the velocity components are measured a) for larger impact angles b) at glancing impact.

The two velocity components determine the magnitude of the velocity vector and its direction for each point. The position where the highest velocity is measured coincides with the position with the highest particle flux (illustrated by the data rate of the laser doppler anemometer). Since apparently most particles travel through this point with the highest velocity, the rebound velocity and angle are defined as the velocity and angle measured in this position.

Strength degradation
The strength of the eroded samples was determined by performing a number of three point bending tests. For each experiment about 30 glass samples of $40 \times 20 \times 1.9$ mm^3 were cut out of an eroded glass plate (200 m/s) and tested in a three point bending experiment. The experimental procedure of these experiments is described in chapter 2 [13]. To test the effect of erosion direction, samples were tested in both the x and y direction (see Figure 4-2).

4.3   Erosion rate and surface roughness

Figure 4-4 summarises the erosion and surface roughness dependency of impact angle for three different impact velocities. The surface roughness values plotted are

obtained by averaging the values measured in the x and y direction, since no significant difference was found between the values.

a)

b)
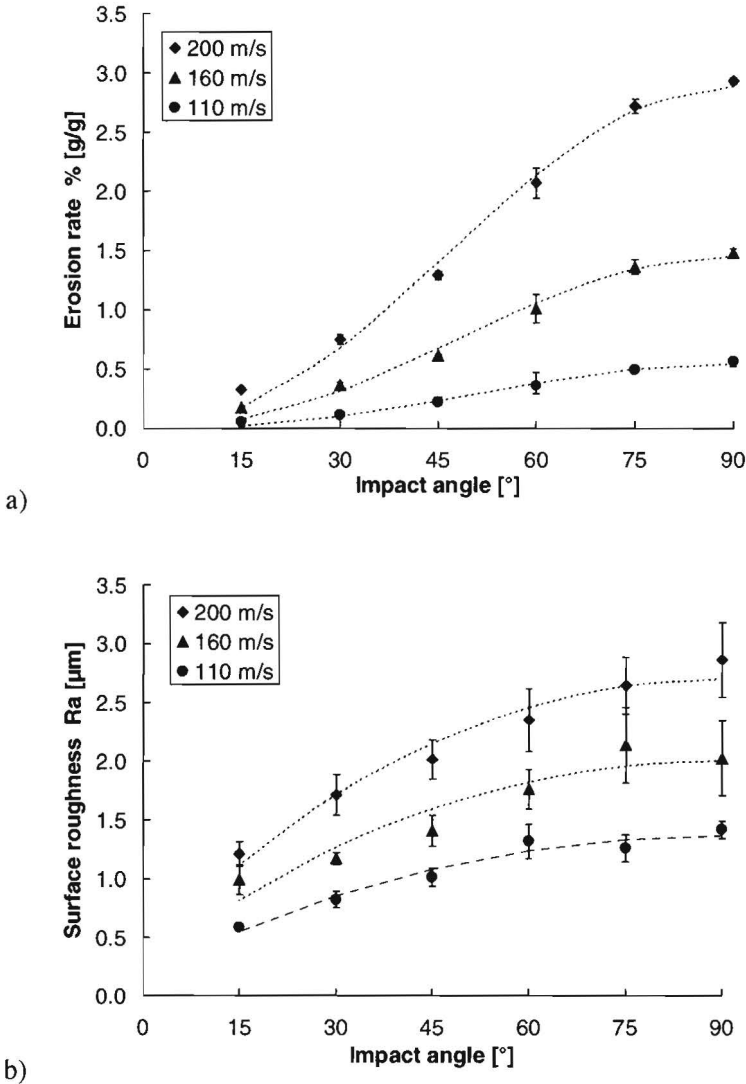
Figure 4-4: The erosion rate (a) and resulting surface roughness (b) as function of impact angle and impact velocity. The error bars represent the standard deviation in the measurements, while the lines represent a fit with sinθ.

The dotted lines represent least-squares fits with the relation $y = a \cdot \sin(\theta)^b$. As the graphs show, this relation fits the data well. The power b is fitted to 2.1-2.4 for the

erosion data and to 0.65-0.68 for the surface roughness. These values compare well with theoretical values derived in chapter 2 [13] for the velocity dependence of erosion (7/3) and surface roughness (2/3).

Plotting all data against the normal component of the velocity gives reasonable plots (see Figure 4-5). The erosion data shows signs of a systematic deviation at small impact angles comparable to the one found by Morrison et al. [4]. At glancing impact the erosion rate is higher than the $\sin(\theta)$-relation predicts. The velocity exponent of the fit over all data is slightly higher than the exponent of $\sin(\theta)$ found above (2.6 instead of 2.1-2.4).

a)

b)
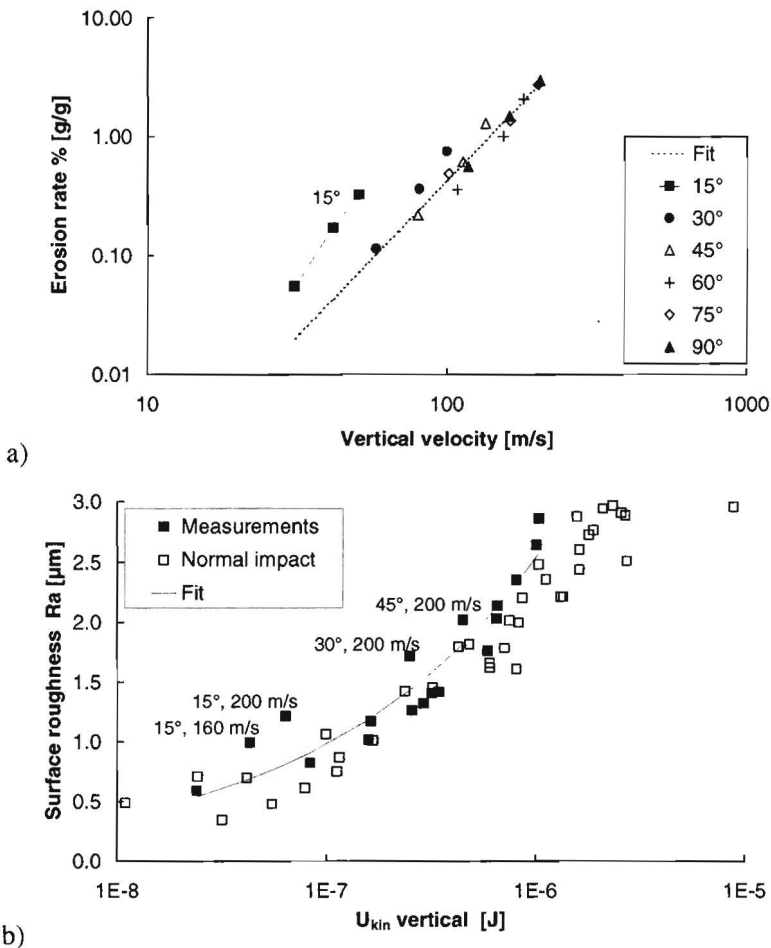
Figure 4-5: The erosion rate and surface roughness plotted against the vertical component of the impact velocity.

The surface roughness data are plotted against the kinetic energy calculated with the component of the velocity normal to the substrate surface. This enables comparison with data obtained with different particle sizes at normal impact (chapter 2, [13]). As the plot shows, the scatter of the surface roughness data is evidently within the range of the data at normal erosion.

Considering these data the correlation of erosion and surface roughness with the normal component of the velocity ($v \sin(\theta)$) is a reasonable approximation for the erosion process at oblique angles.

4.4 Strength and damage

The strength distribution of the tested samples is processed using Weibull statistics to obtain the nominal strength for each angle and testing direction. Figure 4-6 combines the results for the different angles and the two orientations. The x-direction samples were tested in the direction of the oblique jet, the y-direction samples were tested perpendicular to this direction.

Considering the accuracy of the measurements and the contradiction between the relative position at 15 and 30 impact-angle, any suggestion of difference between the strength of the two directions is considered to be non-significant.
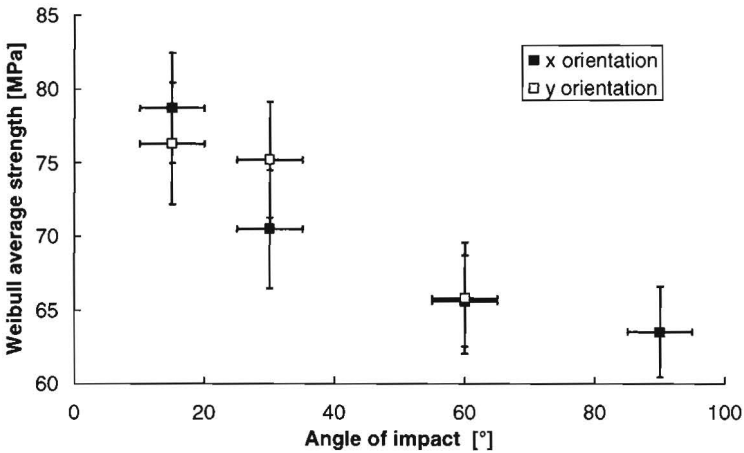
Figure 4-6: Comparison of the strength of oblique eroded samples. X-direction tested in the direction of the oblique jet, y-direction perpendicular to it. The error bars indicate the standard deviation of the samples.

To enable the comparison with normal impact data, the average strength is plotted in Figure 4-7 against the kinetic energy of the particle. For oblique impact the kinetic energy is calculated with the velocity component normal to the surface. The

nominal strength for oblique impact is calculated with the x-direction and y-direction data combined. The figure also shows the data from chapter 2 obtained at normal impact.
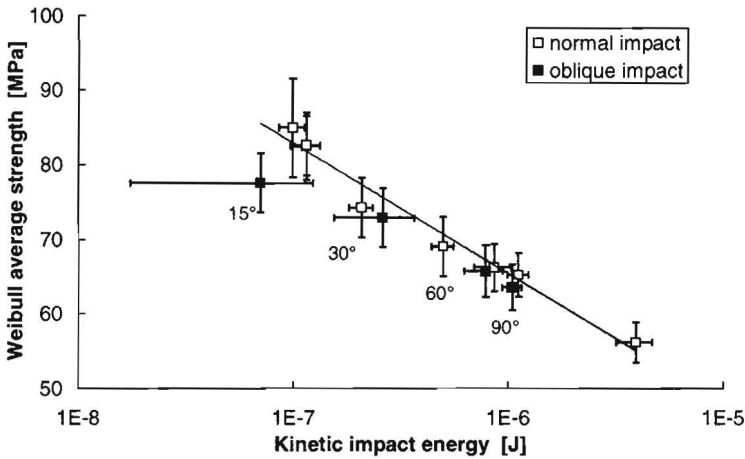
Figure 4-7: The nominal strength as function of impact energy of the particles, comparing oblique impact with normal impact data [Chapter 2, 13].

The figure shows that the strength at oblique erosion can be described well with the kinetic energy calculated with the normal velocity component. It confirms the $\sin(\theta)$-rule. Only at 15 degrees the strength reduction is possibly somewhat larger then described by this "rule". This itself might be in-line with the higher erosion then expected by the rule at these angles. This higher erosion might thus also include increased damage and decreased strength.

4.5 Rebound characteristics

The rebound measurements show a considerable influence of the airflow on the particle trajectories. Since the measurement technique used with the one-dimensional Laser Doppler system required measurements outside the cross-section of the impacting and rebounding beam, the velocity components are measured at considerable distance from the impact sites. Plotting examples of the results as shown in Figure 4-8 and extending the rebound-velocity vectors reveals that they do not intersect the surface at the site where impact is expected considering the incident beam. As suggested by the dot-dashed lines the rebounding particles have probably been deviated by the influence of the air-jet on the substrate.

Although the air-jet influence on the particles severely hampers the value of the experimental results, bearing the limitations in mind, the results still give hints for interesting observations.
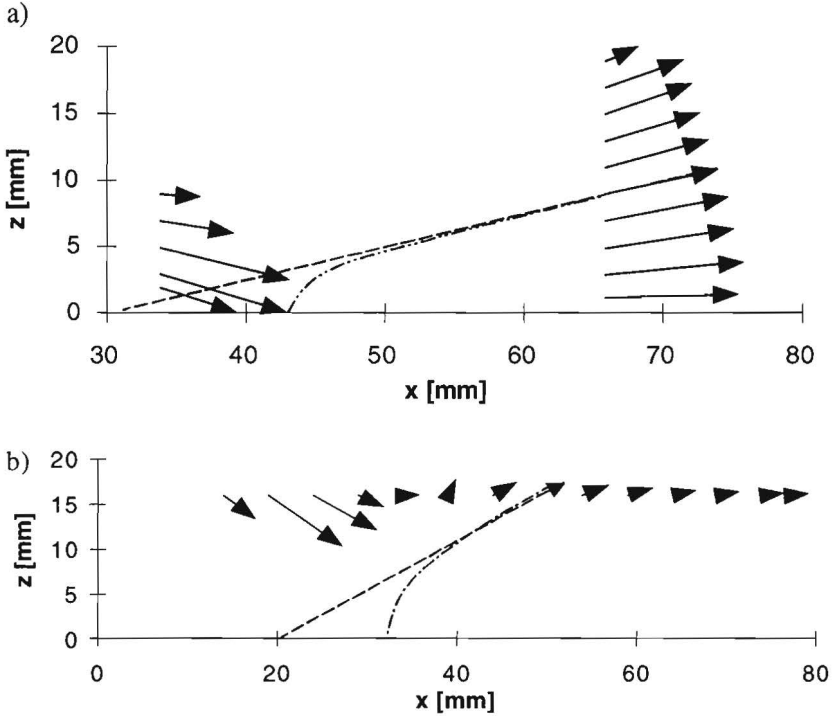
Figure 4-8: Example of the velocity results at 15°(a) and 30°(b) impact angle both at 110 m/s impact speed. The broken lines extend a rebound velocity vector. The dot-dashed line illustrates a possible particle trajectory.

Figure 4-9 collects the rebound velocity and angle as function of angle of incidence of three impact velocities. The rebound velocity data decreases with increasing angle of impact and seems to be independent of impact velocity. The rebound angle shows a comparable independence of impact velocity and is measured roughly a factor 0.5 times the impact angle. The data at normal impact deviate from these trends but should be treated with care, since here no well-defined rebounding beam is present. Worth remarking is the decrease of rebound velocity at glancing contact of high velocity particles.

Although the observed trends should be used with care, since the observed phenomena are influenced by the airflow, it is believed that the trends are significant.
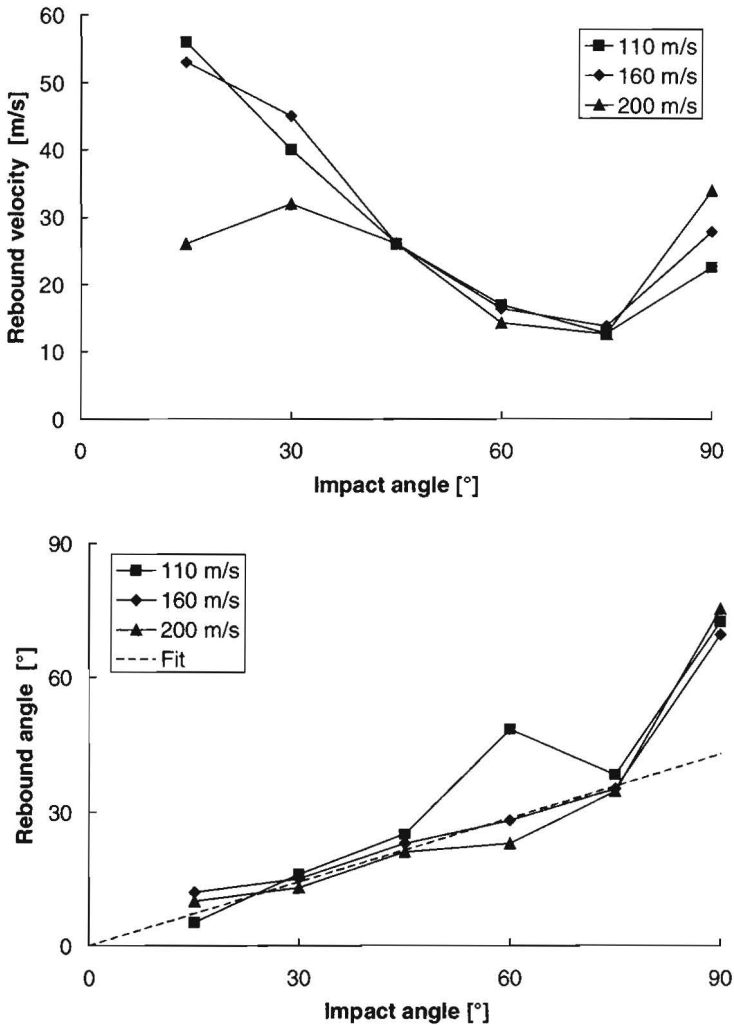
Figure 4-9: The rebound velocities and angles as function of impact velocity and impact angle.

4.6 Discussion and conclusion

The sin(θ)-rule

The experimental data collected in this chapter on impact of glass with hard, sharp alumina particles, confirm the sin(θ)-rule presented in the literature. The erosion

data, the surface roughness data and the strength degradation data all scale with velocity component normal to the target.

The abundance of observations shows the need for a comprehensible model to back up the empirical rule. Starting from the concept of quasi-static indentation, that was successful in modelling normal impact in chapter 2, we will supply an argumentation based on symmetry considerations.

As discussed in chapter 2 at normal impact, the erosion mechanism for hard particles on brittle materials can be described by the theory of well-developed plasticity. In this situation an impacting particle generates a plastic indentation in the substrate. Erosion takes place by the removal of chips of material above the lateral cracks formed, while radial cracks are expected to determine the strength degradation of the substrates.

At oblique impact the component of the kinetic energy normal to the surface will generate a plastic zone like that at normal impact. The movement of the particle along the surface will generate an additional tangential force. In the quasi-static analogy where normal impact corresponds with an indentation experiment, this situation corresponds with a scratching experiment, but only over a short length. This movement might give rise to a ductile material removal mechanism (cutting or ploughing wear) but since the material removal rate is much lower than that of chipping by lateral cracks, it usually will not show in the total erosion rate.

Scratching experiments display usually a fixed ratio between tangential force and normal force often expressed as a friction coefficient. This coefficient depends on the material and shape of the indenter and varies generally between 0.1 and 0.4 [see for example 14]. Since in oblique impact the maximum tangential force can be expected to follow the same rule, it will be a factor smaller than the normal force. It the following discussion we will therefore consider the tangential force as a modifier of the stress field generated by the normal force.

The presence of a horizontal component of the stress will modify the stress-field the plastic zone exerts on its (linear) elastic surrounding as sketched in Figure 4-10. Since the stress p is a maximal normal stress correlated with the yield stress of the substrate, an additional tangential force must lead to a zone of decreased stress behind the indenting particle. In Figure 4-10a this zone is indicated schematically as an area without stress.

To study the effect of tangential force on the development of cracks it is convenient to split the stress field exerted by the plastic zone in its symmetrical

part governed by the normal force and its anti-symmetrical part controlled by the tangential force (see Figure 4-10 b) and c)).
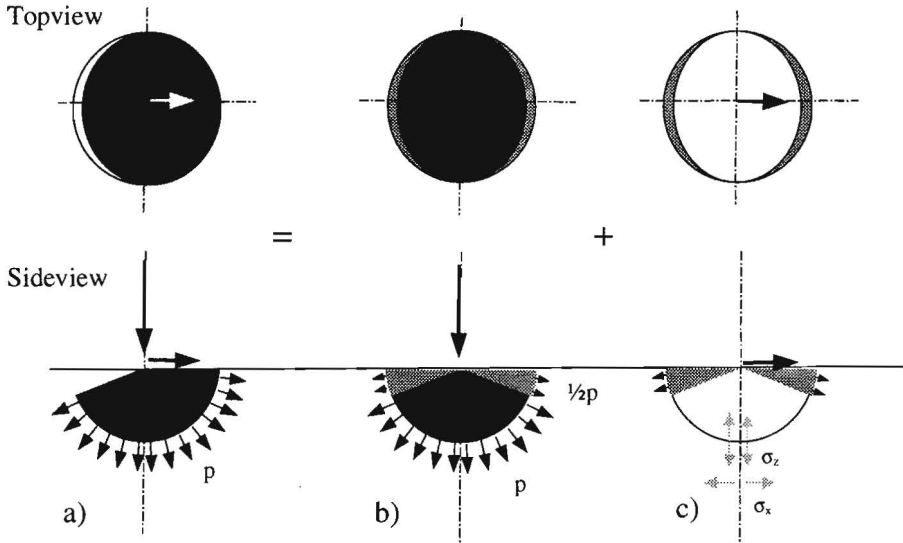
Figure 4-10: Schematic representation of the stress field exerted by the plastic zone on the surrounding material (a), split in its symmetrical (b) and its anti-symmetrical part (c).

Symmetry reasoning with Figure 4-10c shows that the anti-symmetrical case does not lead to a crack opening stress for median cracks (σ_x) and will not influence the strength reduction of the substrate. Nor does it influence the initiation stresses for lateral cracks (σ_z). The stress field generated will, however, influence the development of the lateral crack, but its influence downstream of the impact is opposite to that upstream. These two contributions will counteract in the total contribution to the erosion process. So the influence of the anti-symmetrical part on both erosion and substrate strength can be expected to be very small.

The influence of the tangential force is, however, not limited to the anti-symmetrical part of the loading. As the top view in Figure 4-10b shows it decreases the area where the pressure p acts. The same normal force thus requires a larger plastic zone with a tangential force than without. This effect is probably only noticeable at relative large ratio tangential/normal force (low impact angles). In the direction perpendicular to the particle movement the larger plastic zone will lead to larger lateral cracks (erosion) and radial/median cracks (lower strength).

The increased erosion at glancing impact originates more likely from this increased lateral crack development than from a contribution of ploughing wear. The amount

of material removed by ductile erosion mechanisms is generally very small compared to that removed by lateral cracking. It is therefore not very likely that ductile erosion will induce measurable effects, even at glancing impact.

Please note that the situation discussed above differs fundamentally from that of an elastic contact. For the elastic contact of a sliding sphere, analytical models are available for the stress field [15, 16, 17]. They illustrate that the stress fields change considerably with increasing tangential force. Unlike in the situation of well-developed plasticity discussed above, the changes in stress field have for elastic contact a large influence on the initiation of damage. Since here the cracks initiate at the surface of the substrate, the increased tensile stresses from the tangential force behind the moving contact result in the forming of (half) ring shaped cracks at far smaller normal forces.

Rebound characteristics

The influence of the air on the particle trajectory leads to errors in the measured rebound velocity and rebound angle. The effect on rebound angle is probably larger than on rebound velocity, since the airflow will decelerate the particles in the direction normal to the surface and accelerate them tangential to it. So the actual rebound angle is most likely larger than the measured ones.

The effect of the air jet reducing the rebound velocity is expected to increase at higher impact angles, since the rebounding particles experience more headwinds. Although the measured decrease of rebound velocity at increasing impact angle is consistent with this airflow effect, it is also compatible with the findings of Hutchings et al. [18]. Shooting hard steel spherical particles against mild steel substrates they observed a clear decrease of rebound velocity with increasing impact angle. Describing particle impact as fully plastic, they derived a model that predicts the observed phenomena nicely. Rebound in this model is obtained by the particles having lost their vertical velocity at impact still having part of their horizontal velocity. The remaining horizontal velocity forces the particle from the indentation it has made. Estimating the airflow effect shows that it may only be partially responsible for this effect.

The decrease of rebound velocity at high impact velocities and glancing impact is significant and probably caused by an increase in ploughing wear. This is consistent with Sheldon and Kanhere [19] who remark that angular particles have the tendency to imbed in the surface of ductile materials at glancing impact.

Studying the rebound velocity and angle data collected in Figure 4-9, the striking observation remains that the measured rebound parameters do not seem to depend

on the impact velocity itself. Although the impact velocity is varied almost a factor two the rebound parameters are quite comparable. This finding is not supported by data in the literature. For pure ductile impacts Hutchings et al. [18] found, theoretically and experimentally, a roughly linear dependency of rebound velocity on impact velocity. The elastic-plastic theory of Yoffe [20] confirms these findings by predicting that a fixed fraction of the impact energy is stored in elastic deformation. This energy can later be released to rebound the particle.

The limitations set by the measuring technique make it impossible to draw firm conclusions whether the observations are an artefact of the measuring method or a physical effect. To enable a conclusion, measurements are needed which exclude the airflow effect on the rebounding particles, for example by using a two dimensional Laser Doppler system close to the surface of the target.

4.7 List of symbols

E_r The erosion rate (mass of removed substrate per mass of erodent used) [g/J], Section 4.1 and Equation 2.17.

U_{kin} The kinetic energy of an impacting particle [J], Figure 4.5.

a Fit coefficient of the oblique erosion and surface roughness, Figure 4.4.

b Fit coefficient of the oblique erosion and surface roughness, Figure 4.4.

k Velocity exponent in relation for erosion rate [-], Section 4.1.

p Normal stress at the outside of the plastic zone [Pa], Figure 4.10.

x The coordinate in the oblique impact direction of the substrate surface, Figure 4.2.

y The coordinate perpendicular to the oblique impact direction of the substrate surface, Figure 4.2.

α_{out} The particle rebound angle [°], Figure 4.3.

θ Impact angle of abrasive particles [°], Figure 4.3.

σ_x Normal stress component at the bottom of the plastic zone in the direction perpendicular to the surface [Pa], Figure 4.10.

σ_z Normal stress component at the bottom of the plastic zone in the direction lateral to the surface [Pa], Figure 4.10.

4.8 Literature

1   I.M. Hutchings, *Transitions, threshold effects and erosion maps*, Key Eng. Mat. 71 (1992) 75-92.

2   J.L. Routbort and R.O. Scattergood, *Solid particle erosion of ceramics and ceramic composites*, Key Eng. Mat. 71 (1992) 23-50.

3   B.J. Hockey, S.M. Wiederhorn, H. Johnson, *Erosion of brittle solids by solid particle impact*, in R.C. Bradt, D.P.H. Hasselman, F.F. Lange (eds), *Fracture mechanics of ceramics*, 3 Plenum Press, NY (1978) 379-390.

4   C.T. Morrison, J.L. Routbort, R.O. Scattergood, *Solid particle erosion of mullite*, Wear 105 (1985) 19-27.

5   G.L. Sheldon, *Similarities and differences in the erosion behavior of materials*, J. Basic. Eng. (1970) 619-626.

6   J.G.A. Bitter, *A study of erosion phenomena*, Parts 1 and 2, Wear 6 (1963) 5-21, 169-190.

7   S. Wada, N. Watanabe, *Solid particle erosion of brittle materials. V. The effect of impingement angle*, J. Ceram. Soc. Japan. International Ed 95, no 10 (1987) 976-983.

8   S. Srinivasan, R.O. Scattergood, *Erosion of Mg-PSZ by solid particle impact*, Adv. Ceram. Mat. 3, no 4 (1988) 345-352.

9   A.T. Ibrahim, Y. Ballout, J.E. Talia, *An attempt to unify the models used for ductile and brittle solid particle erosion*, J. Mater. Eng. 13 (1991) 63-70.

10 Y. Ballout, J.A. Mathis, J.E. Talia, *Solid particle erosion mechanisms in glass*, Wear 196 (1996) 263-269.

11 S. Srinivasan and R.O. Scattergood, *On lateral cracks in glass*, J. Mater. Sci. 22 (1987) 3463-3469.

12 S.M. Wiederhorn, B.R. Lawn, B.J. Hockey, *Effect of particle impact angle on strength degradation of glass*, J. Am. Ceram. Soc. 62, no 11-12 (1979) 639-640.

13 P.J. Slikkerveer, P.C.P. Bouten, F.H. in 't Veld, H. Scholten, *Erosion and damage by sharp particles*, Wear 217 (1998) 237-250.

14 F.P. Bowden, D. Tabor, *The friction and lubrication of solids Vol II*, Clarendon Oxford (1964).

15 G.M. Hamilton, L.E. Goodman, *The stress field created by a circular sliding contact*, Trans ASME, J. Appl. Mech. 33 (1966) 371-389.

16 G.M. Hamilton, *Explicit equations for the stresses beneath a sliding spherical contact*, Proc. Inst. Mech. Eng. 197C (1983) 53-61.

17 K.L. Johnson, *Contact Mechanics*, Cambridge University Press (1989).

18 I.M. Hutchings, N.H. Macmillan, D.G. Rickerby, *Further studies of oblique impact of a hard solid against a ductile solid*, Int. J. Mech. Sci. 23 no 11 (1981) 639-646.

19 G.L. Sheldon and A. Kanhere, *An investigation of impingement erosion using single particles*, Wear 21 (1972) 195-209.

20 E.H. Yoffe, *Elastic stress fields caused by indenting brittle materials*, Phil. Mag. A 46, no 4 (1982) 617-628.

5 A model for patterned erosion[*]

To obtain structures by the powder-blast process some parts of the surface need to be shielded against the abrasive particles. Although it is possible to obtain selective exposure by writing a pattern with a small erosive jet, the most convenient and accurate way is to use a mask of patterned erosion-resistant material that protects the covered surfaces from erosion.

While the previous chapters considered homogeneous erosion of surfaces, the next two chapters focus on patterned erosion. Where chapter 6 concentrates on the wear of elastomeric mask materials, this chapter considers the shapes formed in masked substrates. Starting from the erosion models presented in the previous chapters, a model is developed to describe the forming of three-dimensional structures.

The mathematical model is studied extensively to understand the way the structures develop and to find analytical solutions. An extended model is solved numerically. The results are compared with experimental data to find that the character of the solutions agrees well with that displayed experimentally. Simplifications in the model give rise to quantitative differences.

---

[*] Combines P.J. Slikkerveer, F.H. in 't Veld, *Model for patterned erosion*, ICEAW conference, Cambridge 1998, accepted for Wear and parts of P.J. Slikkerveer, J.H.M. ten Thije Boonkkamp, *Mathematical modeling of erosion by powder blasting*, submitted to Surveys on mathematics for industry.

5.1 Introduction

Patterned sandblasting is a well-known process for patterning window glass and mirrors. It has been used for many years for decoration purposes. The scattering of light at the eroded surface contrasts nicely with the smooth non-affected surfaces. To this aim relative low requirements are set to the dimensions of the patterns and the surfaces are often eroded only superficially.

For the industrial etching of large displays the technique needs to be developed into a process with high positional and shape accuracy and a high reproducibility and homogeneity over large surfaces. The application moreover requests patterns with an aspect ratio (depth/width) larger then 1.

To enable structures with fine dimensions the powder-blast process makes use of erosion resistant mask as sketched in Figure 5-1. One or more abrasive jets are scanned over the substrate with the purpose to obtain a homogeneous exposure of the surface to abrasive particles. For a homogeneous exposure the movement of the nozzles need to be well controlled, as well as their powder and air fluxes. The dimension of the jet is usually much larger than the structures desired.
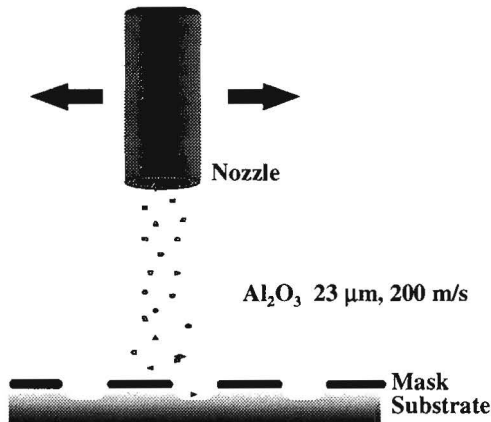
Figure 5-1: Schematic representation of erosive etching using a mask.

The substrate is covered with an erosion-resistant mask. Since it specifies which areas will be eroded and which not, the accuracy of the mask defines both the positional and shape accuracy of the patterns created. Since the mask can be made by photolithography a high precision in patterning can be obtained. The erosion process itself creates the eroded shape.

Figure 5-2 illustrates the development of a hole during the powder-blasting process. The pictures have been made using time-lapse photography of a fixed

powder jet over a metal mask with one circular hole. The substrate is soda-lime glass. The pictures show a number of general characteristics of the shapes produced with the powder-blasting process: the patterns tend to have tipped points, they develop dimpled walls at greater depths and the erosion speed decreases with the depth of the pattern.
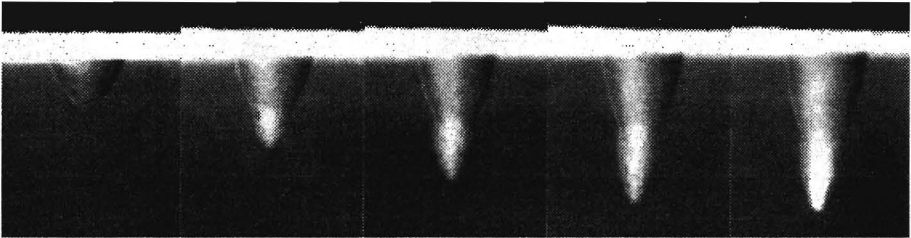
Figure 5-2: An example of the evolution of patterns by erosion using a single-round-hole mask.

The surface development during unmasked erosion of ductile materials has been studied by Carter et al. [1, 2], using a mathematical formulation derived in the field of ion sputtering [e.g. 3]. The difference in angle dependency of erosion and the presence of a mask make their results not applicable for the powder blasting of brittle substrates as studied in this chapter.

The chapter focuses on understanding the forming of shapes like the ones shown in Figure 5-2. To do so models were formulated and solved both analytically and numerically. Section 5.2 describes the development of a first model, which can be solved analytically. Although limited in describing the shapes formed, the analytical study discovers much of the basic behaviour of the shape evolution. Section 5.3 describes an extended model, which must be solved numerically. In section 5.4 the results of the models are compared with shapes of wide and narrow trenches obtained experimentally showing a reasonable resemblance, after which a number of conclusions will be drawn.

5.2   First model and analytical solutions

5.2.1   Model construction

The first model is based on the hypothesis that the fundamental shape of the eroded patterns originates from the dependence of erosion on impact angle as described in the previous chapter. Since for brittle materials erosion is most efficient at normal impact, the rate of erosion decreases with an increasing slope of the walls, which agrees with the observed behaviour.

In this chapter we will concentrate on the evolution of two-dimensional structures like the one sketched in Figure 5-3. It contains an unprotected area between $x = 0$ and $x = W$, that is initially flat, i.e. $z = 0$. This geometry includes trenches or round holes.

To simplify the model, the scanning nozzles are replaced with their idealistic representation, where the whole surface is homogeneously exposed to abrasive particles. The flux of kinetic energy of these particles is denoted with J (J/m^{2}s). Although a particle jet usually displays some divergence, in the model all particles are assumed to have a vertical velocity.

The mask is modelled simply by assuming zero erosion at the masked parts ($x < 0$ and $x > W$). In doing so effects of mask-thickness or mask-erosion are being neglected.

The models neglect effects of rebounding particles. Experiments show that the powder is readily removed from eroded profiles, probably by the combination of the airflow from the jet and its scanning motion. The rebounding particles, however, might give an increased flux-effect (see Chapter 8), which is ignored in the models.
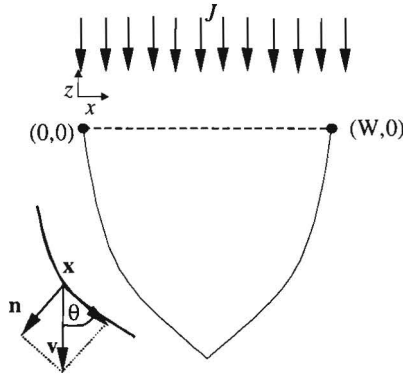
Figure 5-3: Definition of the geometrical parameters used in the models.

The model starts from the universal erosion relation for normal impact derived in chapter 2 [4]. Formulated in the erosion efficiency it is independent of particle size. The erosion efficiency (E_{eff}), defined as the amount of eroded material in grams per amount of kinetic energy in the particles of the jet (Joule), is found to be a function of the kinetic energy of the individual particle

$$E_{eff} = C_{eff} \left(\tfrac{1}{2} m v^2 \right)^p . \tag{5.1}$$

Here $\tfrac{1}{2} m v^2$ denotes the kinetic energy of the average particle in the powder jet. C_{eff} and p are model parameters determined in chapter 2 [4] to be 0.0475 and 0.247,

respectively, for the boro-silicate substrate-alumina erodent combination considered in this paper.

The erosion velocity of the surface ($\partial x/\partial t$) can be obtained by multiplying the erosion efficiency by the flux of kinetic energy (J) and dividing it by the specific mass of the substrate (ρ_t). Note that the surface removal rate is directed along the inward normal of the geometry (**n**, see Figure 5-3)

$$\frac{\partial \, \mathbf{x}}{\partial t} = \frac{E_{eff} \, J}{\rho_t} \, \mathbf{n} = C_{eff} \left(\tfrac{1}{2} mv^2\right)^p \frac{J}{\rho_t} \, \mathbf{n} \qquad (5.2)$$

To obtain the erosion velocity at oblique impact the velocity can be replaced with its component normal to the surface (v_n) using the "sin(θ)-rule" demonstrated in chapter 4.

The energy flux of the abrasive jet can be calculated as half the mass flux of the jet per unit substrate surface times the particle velocity squared.

$$J = \frac{1}{2} \, \Phi v^2 \qquad (5.3)$$

Φ is the mass flux of powder. At normal impact it equals that of the jet (Φ_{jet}). At oblique impact the mass flux of the jet needs to be multiplied with sin(θ), where θ is the impact angle of the beam (see Figure 5-3). At oblique impact the velocity is of course replaced with its component normal to the surface (v_n).

Equation 5.2 describes the evolution of the surface in the direction of its normal vector. It is convenient to describe the evolution of the surface in the vertical direction, $z = z(x,t)$. To obtain a vertical displacement of the calculation points, we substitute

$$\frac{\partial \, z}{\partial t} = -\left|\frac{\partial \, \mathbf{x}}{\partial t}\right| \frac{1}{\sin \theta} \qquad (5.4)$$

Combining equation 5.2 to 5.4 and substituting $v_n = v_{jet}\sin(\theta)$ gives an evolution equation of the surface.

$$\frac{\partial \, z}{\partial t} = -C_{eff} \left(\tfrac{1}{2} mv_{jet}^2\right)^p \frac{\tfrac{1}{2} \Phi_{jet} v_{jet}^2}{\rho_t} (\sin \theta)^{2+2p} \qquad (5.5)$$

By expressing sin(θ) in the slope of the local geometry, we obtain a first order, non-linear, partial differential equation for the evolution of the geometry. For

convenience the power $2+2p$ will now be replaced with k, which can be recognised as the velocity dependence of the erosion rate (usually between 2 and 4)

$$\frac{\partial z}{\partial t} = C_{eff} \left(\tfrac{1}{2} m\right)^p \frac{\tfrac{1}{2} \Phi_{jet} v_{jet}^k}{\rho_t} \left(\frac{1}{\sqrt{1+\left(\partial z / \partial x\right)^2}}\right)^k . \tag{5.6}$$

The boundary conditions for the trench-erosion problem representing the ideal mask are $z(0, t)=0$ and $z(W, t)=0$ (see Figure 5-3), while the initial condition – an undamaged surface - is given by $z(x, 0)=0$.

It is both convenient and illustrative to bring equation 5.6 in a dimensionless form by introducing the characteristic length scale L^* and time scale t^*. The width of the pattern (W) is the obvious choice for L^* and by choosing the characteristic time scale to be equal to

$$t^* = \frac{2W\rho_t}{C_{eff} \left(\tfrac{1}{2} m\right)^p v_{jet}^k \Phi_{jet}} \tag{5.7}$$

equation 5.6 reduces to

$$\frac{\partial z'}{\partial t'} = -\left(\frac{1}{\sqrt{1+\left(\partial z'/\partial x'\right)^2}}\right)^k . \tag{5.8}$$

The initial and boundary conditions now become: $z'(0,t') = 0$, $z'(1,t') = 0$ and $z'(x',0) = 0$.

The dimensionless relation does not contain any dimensionless groups. This means that according to the model all trench shapes are isomorphic, having the same relative shape, although this shape may have been obtained after a different time of erosion.

The model does not show any influence of particle size. The model for homogeneous erosion [Chapter 2] on which the model is based shows that particle size is not an independent parameter, but influences erosion only via the kinetic energy of the particles. In the patterns considered here an effect of geometrical hindering may be expected where particles do not fit in (details of) the geometry. The model neglects this effect, which means that the solutions to equation 5.8 must be regarded as obtained with infinitely small particles. Experimental verification will show the effect of this assumption.

5.2.2 First analytical model

Equation 5.8 is a first-order, non-linear hyperbolic partial differential equation, which can be solved using the method of characteristics. Along so-called characteristic lines the partial differential equation is reduced to a set of ordinary differential equations, which can be solved via direct integration. To do so the differential equation (equation 5.8) is brought in canonical form by replacing $\partial z'/\partial t'$ by p and $\partial z'/\partial x'$ by q and rewriting to

$$F(x,z,t,p,q) = p + (1+q^2)^{-k/2} = 0.$$
(5.9)

The following set of ordinary differential equations describes the characteristics themselves and the solution along these as function of a parameter s along the characteristics [5]

$$\frac{dx'}{ds} = \frac{\partial F}{\partial q},$$

$$\frac{dz'}{ds} = p\frac{\partial F}{\partial p} + q\frac{\partial F}{\partial q} = p + q\frac{\partial F}{\partial q},$$

$$\frac{dt'}{ds} = \frac{\partial F}{\partial p} = 1,$$
(5.10)

$$\frac{dp}{ds} = -\left(p\frac{\partial F}{\partial z} + \frac{\partial F}{\partial t}\right) = 0,$$

$$\frac{dq}{ds} = -\left(q\frac{\partial F}{\partial z} + \frac{\partial F}{\partial r}\right) = 0.$$

The equations above show that p ($= \partial z'/\partial t'$) and q ($= \partial z'/\partial x'$) are constant along the characteristics. They show that the parameter s differs from time t' by an arbitrary constant (for example t_0), so we may replace s with t'-t_0. The remaining two relations can be solved with aid of the original equation to a parameter description of the characteristic line. Each characteristic is defined by the value of the invariant $q = q_0$ at some position in the time-space frame (x_0, z_0, t_0)

$$x' = x_0' - \frac{kq_0(t'-t_0)}{\left(1+q_0^2\right)^{k/2+1}}$$

$$z' = z_0' - (t'-t_0)\left(\frac{1}{\left(1+q_0^2\right)^{k/2}} + \frac{kq_0^2}{\left(1+q_0^2\right)^{k/2+1}}\right).$$
(5.11)

As the equations 5.11 show, the characteristics are straight lines as function of time. The shape of the surface can be found by plotting the position at the same time along all characteristics.

Since the initial condition for equation 5.8 is $z'(x',0)=0$ the initial value for $q_0 = \partial z/\partial x|_{t'=0}$ equals zero. Substituting this into equation 5.11 we find the characteristics as vertical lines, while the evolution equation for the surface is

$$z'(x',t') = -t' \tag{5.12}$$

except for the two boundary points that do not move. This (trivial) solution is in fact the solution for homogeneous erosion of a surface, which is fully unprotected. Although it is a solution of the mathematical model, the discontinuities near the boundary points make it no solution of the physical problem (see Figure 5-4).
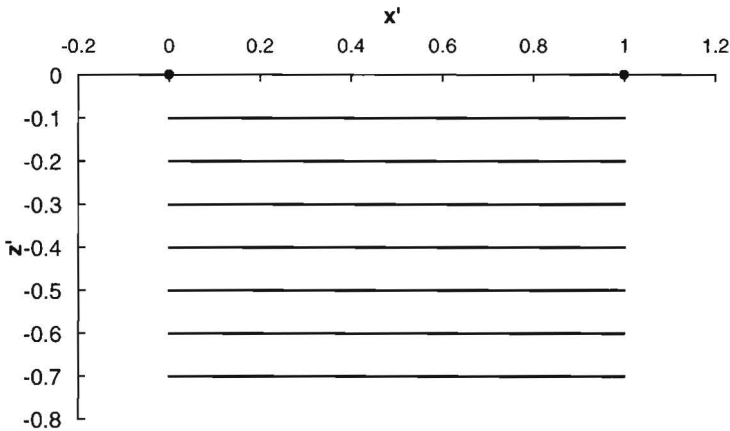
Figure 5-4: The trivial solution of the mathematical model.

5.2.3 Extended analytical model

A non-physical solution is often included in a differential equation by an omission of a physical effect. Comparing the solution with the actual erosion process, it is very unlikely that real particles will travel at an infinitesimal distance from the vertical walls near the boundary points without touching it. Since actual particles have a finite size they will not be able to hit the bottom at an infinitely small distance from the sides of the step. To overcome this non-physical description near the boundary points a flux boundary layer is introduced as sketched in Figure 5-5.

The particle size effect is obtained by abandoning the constant particle flux over the width of the structure, and introducing two flux boundary layers, were mask hindering make fewer particles hit. Considering that the mask usually has a thickness of over 50 μm, the assumption seems reasonable. The boundary layer of variable width (δ) is used to study the effect of "particle size" on the solution.
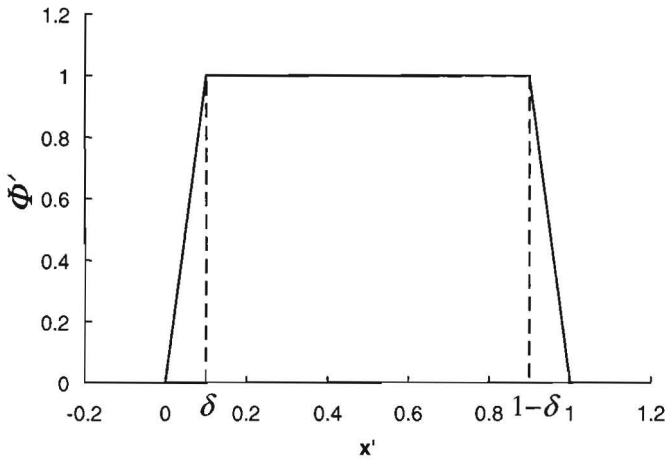
Figure 5-5: The dimensionless mass flux distribution (Φ') as function of width.

With the introduction of these flux boundary layers the geometry $0<x'<1$ is divided in three regions: two flux boundary regions and one central zone. In the central zone the original differential equation holds yielding the characteristic solution 5.11. The surface evolution, however, does not follow the trivial solution in Figure 5-4, since the introduction of the flux boundary layers introduce two new families of characteristics that emerge from the flux boundaries to the centre of the geometry. The central zone is therefore divided in three regions itself, the central region following the trivial solution and two slope boundary layers that originate from the flux boundaries.

To construct the solution we start at the solution in the flux boundary layers. We will describe the solution method for the layer $0< x'< \delta$. The solution in the second flux boundary is obtained in an analogous way. In the boundary layer considered, the varying flux modifies the differential equation to

$$\frac{\partial z'}{\partial t'} = -\frac{x'}{\delta}\left(\frac{1}{\sqrt{1+(\partial z'/\partial x')^2}}\right)^k \tag{5.13}$$

The canonical form leading to the solution becomes

$$F(x',z',t',p,q) = p + \frac{x'}{\delta}(1+q^2)^{-k/2} = 0 \tag{5.14}$$

Like in the previous case we find that the parameter s can be replaced with $t'-t_0'$ and p $(= \partial z/\partial t)$ is constant along the characteristics. The slope q, however, is not constant but follows the relation

$$\frac{dq}{dt} = -\frac{1}{\delta}\left(1+q^2\right)^{-k/2}. \tag{5.15}$$

This relation cannot be solved in a closed form (to $q = q(t)$) and must be solved numerically. By studying the limit cases $q \ll 1$ and $q \gg 1$ its character becomes clear. Using the initial condition $q=0$ at $t'=0$, the solutions for these cases are

$$
\begin{aligned}
q &= -\frac{t}{\delta} && \text{for} \quad q \ll 1 \\
q &= \left(-(k+1)\,t/\delta\right)^{\frac{1}{k+1}} && \text{for} \quad q \gg 1
\end{aligned}
\tag{5.16}
$$

As the limit solutions already revealed, the solution of the equation is independent of lateral position, since both the differential equation 5.15 and the initial condition do not depend on x'. Therefore at any time the slope $(q = \partial z/\partial x)$ is constant over the width of the flux boundary layer. The evolution of q in the flux boundaries can therefore be plotted in a line graph as is done in Figure 5-6.

With $q(t')$ the equations 5.10 can be integrated to find $x'(t')$ and $z'(t')$ in the boundary layers. With $q = q(t')$ calculated numerically, the differential equations for x and z (the first two differential equations of the set relations 5.10) can be integrated numerically. By plotting $x'(t')$ against t' the characteristic curves become visible as drawn schematically in Figure 5-7 revealing the direction of information transfer.

In the figure three families of characteristics can be identified. In the centre the vertical characteristics originate from the homogeneous erosion. One new family emerges from each flux boundary, starting vertically bending inwards and then curving downwards again. As soon as the characteristic curve leaves the flux boundary it becomes a straight line as shown by equation 5.11. As the families of characteristics intersect discontinuities are generated, which in mathematics are usually called shocks. They will be visible in the solution as sudden changes in the slope. Heavy lines indicate the locations of those shocks.
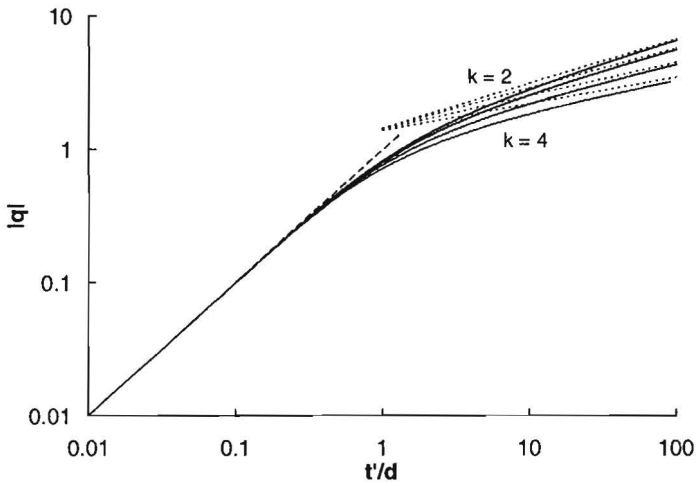
Figure 5-6: The increase of the slope |q| in the flux boundary with time for k=2, 7/3, 3 and 4 respectively. The dashed lines represent the limit approximations (equation 5.16).
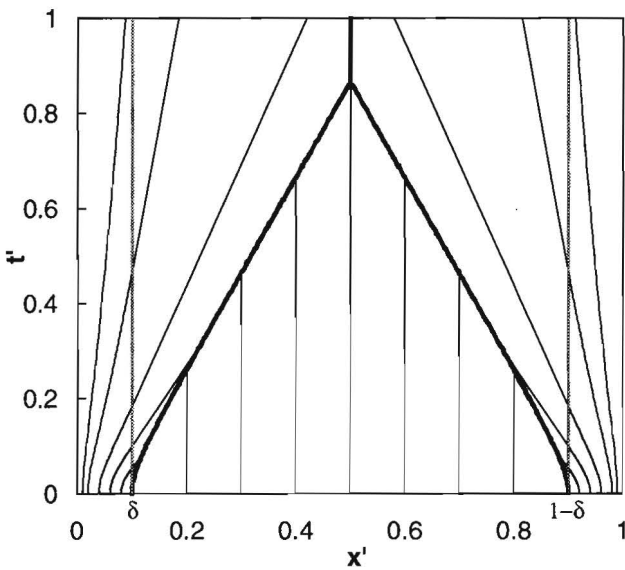
Figure 5-7: A sketch of the shape of the characteristics for δ=0.1. The heavy lines represent the position of the shocks.

The shocks between the two slope solutions and the homogeneous solution in the central region initiate "vertically" from the flux boundaries ($x=\delta$ and $x=1-\delta$) and move inwards where they approach the characteristic with q the solution of

$$1+q^2+kq^2-\left(1+q^2\right)^{k/2+1}=0. \tag{5.17}$$

For arbitrary value of k this equation must be solved numerically. As shown in [6] a set of differential equations can be derived for the position of the shock, but they could not be solved analytically.

With the knowledge on the characteristics and the position of the shocks, the evolution of the surface can be constructed. We again start the construction of the surface in the flux boundary layers working inward focussing on the left boundary layer.

Since above is shown that the slope q is constant in the flux boundary layers, the surface shape in these regions is consequently a straight line

$$z = xq(t'/\delta). \tag{5.18}$$

At intersection with the border of the flux layer the characteristics in fact set the boundary condition for the characteristics in the centre zone described by equation 5.11. The boundary conditions can be described schematically as

$$\begin{aligned}
x_0 &= \delta, \\
q_0 &= q(t_0/\delta), \\
z_0 &= \delta\, q(t_0/\delta).
\end{aligned} \tag{5.19}$$

Here t_0 is the time at which the characteristic intersects the line $x=\delta$, while $q(t'/\delta)$ describes the solution of q as a function of t presented in Figure 5-6. In the central zone the homogenous solution applies as sketched in Figure 5-4. The solution at the right boundary is found analogously with the one described above.

By collocating the parts, a solution is obtained as presented in Figure 5-8. It shows the evolution of the geometry with time for $\delta=0.01$ and $\delta=0.1$. The shapes are continuous showing sudden changes in slope where the shocks are located. The homogeneous erosion solution is recognisable by the flat bottom at the centre of the geometry. Two boundary layers are visible extending gradually with time originating from the boundary conditions. They are not confined to the introduced flux boundary layers, but extend to fill the width of the geometry. This shows that the flux boundaries only initiate the forming of the boundary layers. The width of the boundary layer does not influence the forming of the boundary layers. The shape of the slopes, however, is influenced. The wider the flux boundary the less

steep the slope at the sides of the structures as could be expected. The width of the flux boundary determines the distance between zero erosion at the mask boundary and full erosion at the central zone.
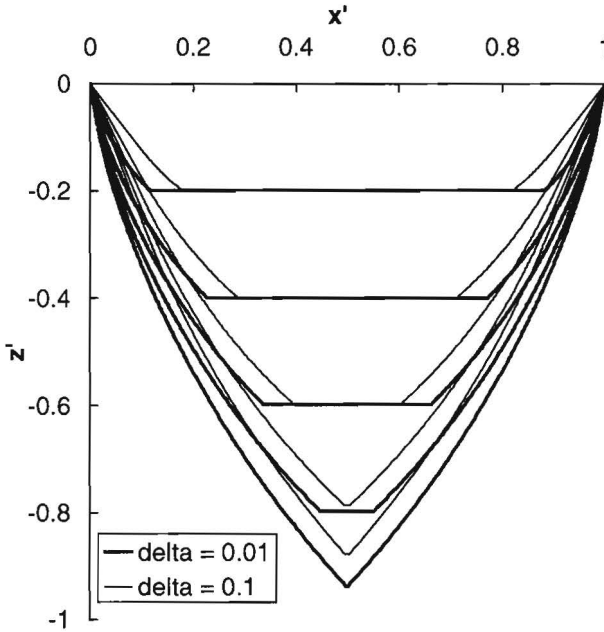
Figure 5-8: The solution for a trench at time level t' = 0.2, 0.4, 0.6, 0.8 and 1. The heavy lines represent the solution for $\delta = 0.01$ and the fine lines for $\delta = 0.1$.

5.2.4 Simplified analytical model

The previous sections have shown that a straightforward formulation of the model led to non-physical steps in the geometry. The introduction of a particle size effect near the boundary points was needed to obtain a continuous solution that compares well with experiments. By this introduction the model looses its simplicity and must be solved numerically. In this section we will investigate the limit of small particles in the extended model. It will regain the simplicity of an analytical solution without loosing the continuity of the solution as the first model did.

The simplification of the analytical model starts with the observation that although the shape of the solution depends on the width of the flux boundary, for all widths the solution is continuous. The presence of a flux boundary layer introduces an extra family of characteristics that generate the desired slopes near the edges of the

pattern. For small widths of the layer its contribution can be considered as prescribing the boundary condition to the central zone. This boundary condition can be described schematically as $q = q(t/\delta)$ at $(x, z) = (\delta, \delta q(t/\delta))$ (see equation 5.19).

Now consider the limit for $\delta \to 0$. Since the width of the flux boundary has been introduced as a model for particle size influence, this limit can be seen as a limit for small particle sizes. Since the physical erosion process develops at finite time-scales, the differential equation for q (equation 5.15) can be replaced with its solution for large t'/δ. Substituting this relation in the relations for the boundary condition gives

$$q = -\left((k+1)\, t/\delta\right)^{\frac{1}{k+1}}$$
$$x = \delta \qquad\qquad\qquad (5.20)$$
$$z = -q\delta$$

The obtained set of equations shows that when δ approaches zero the position were the boundary condition is prescribed (x, z) approximates the boundary point $(0, 0)$, while prescribed slope changes in a decreasing time from zero at $t=0$ to large values. In the limit the boundary condition will be prescribed in the boundary point itself. There is however a fundamental difference with the boundary conditions of the first analytical model. At this boundary point now the slope q is prescribed to change from $q = 0$ to $q = -\infty$ in an infinitesimal time. In fact all these slopes can be considered to be present in this boundary point at $t = 0$.

To illustrate the concept of multiple slopes present in the same point at the same time, we show a situation giving similar results. For this the initial surface shape is supposed that is sketched in Figure 5-9. This geometry can be obtained for example by a short isotropic etch. When the etching time is reduced, the etching depth approaches zero ($\varepsilon \to 0$) and the situation is obtained with a range of gradients in the boundary points.
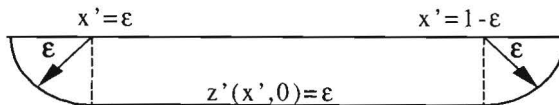
Figure 5-9: An alternative way to introduce a range of slopes in the boundary points.

Using this concept the boundary conditions are found to be $-\infty < q < 0$ in $(0, 0)$ and $0 < q < \infty$ in $(1,0)$. With these conditions the shape of the geometry can be calculated directly with equations 5.11. Being the limit for $\delta \to 0$ of the shapes in

the extended model, the obtained shapes differ only marginally from the shape calculated with $\delta = 0.01$ in Figure 5-8.

Comparing these results with those obtained earlier with the same equations (Figure 5-4) we must conclude that the original boundary conditions $z(0,t) = 0$, $z(1,t) = 0$ are not sufficient to obtain a physical relevant solution.
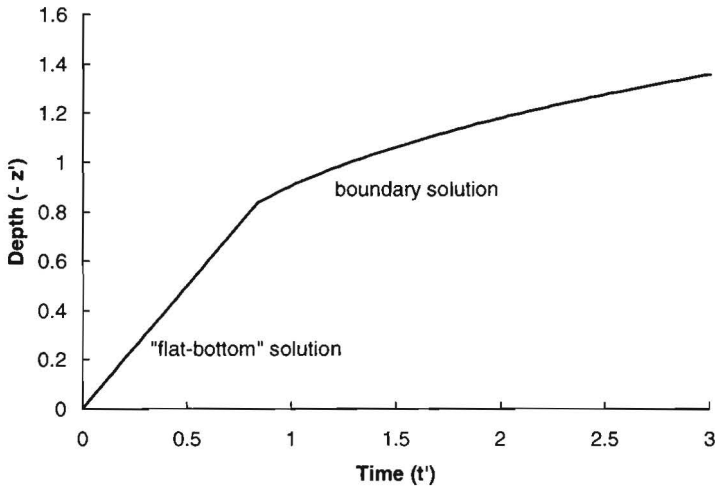
Figure 5-10: The depth of an eroded trench as function of time.

5.2.5 Discussion

The solution to the analytical model exhibits part of the phenomena observed in the erosive etching of patterns like the one in Figure 5-2. It predicts the forming of sharp tips in the shapes and a decrease in erosion speed with time. At short times the depth growth is linear ($z(x,t) = t$), but from the moment that the two boundary conditions meet, the growth velocity decreases drastically (see Figure 5-10).

The analytical model, however, does not predict the forming of dimpled walls. The origin of this phenomenon will be discussed in the next section, where it will lead to an extension of the model.

For trench-like structures the model equations have been made dimensionless by using the width of the structure as a length-scale. For a description of the boundary shape of very wide – shallow structures it is very helpful to choose the length-scale equal to the amount of material removed in homogeneous erosion. Since both the homogeneous erosion solution and the boundary solution scale linearly with time (see equation 5.11), this reduces the solution to one single curve as illustrated in

Figure 5-11. It predicts with deeper erosion also a larger zone of influence of the boundary solution.
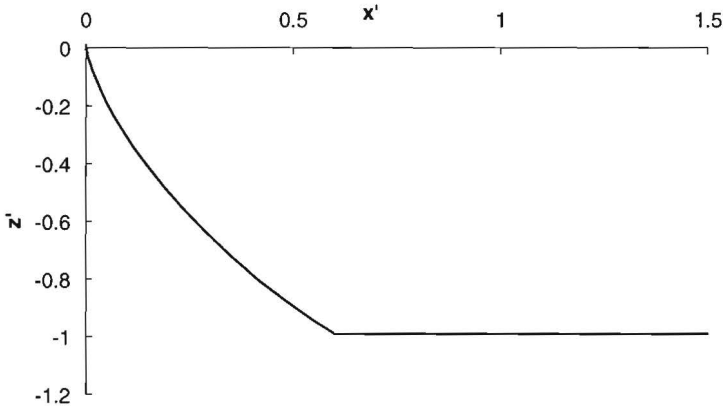
Figure 5-11: The boundary solution scaled with the depth of the homogeneous erosion (k = 7/3).

The technique for constructing the shape of the pattern is not limited to the trench geometry used here. In fact, within the limitations of the analytical model, the shapes of all mask patterns can be constructed in a comparable way; the shape perpendicular to the edge of the mask is the shape presented in Figure 5-11. The shape inside the influence area of the boundary solutions is given by the "flat-bottom" solution. Note that according to the model in this section, the shape obtained for a round hole –like the experimentally obtained one shown in Figure 5-2- is identical to that of a trench shown here.

5.3 Extended model and numerical solution

5.3.1 Model construction

Although the solutions of the analytical model compare well with the general development of the eroded structures, they do fail to describe the forming of the convex-concave walls as visible in Figure 5-2. Since the character of the solutions do not show any tendency to forming those, an extension to the physical model is needed to obtain these shapes.

The basic mechanism behind the dimpled walls is assumed to originate in the effect of particles rebounding from the steep slopes at the edges of the hole. The previous chapter has shown that rebounding particles still have a significant velocity, specifically at glancing impact. The particles rebounding from the sides of the hole are redirected to the centre of the pattern, where they generate additional erosion.

The particles may have lost a considerable amount of energy at first strike, the higher impact angle at second strike compensates the resulting effect on erosion partially.

So the evolution model is extended to include a second erosion term that models the effect of second-strike erosion.

$$\frac{\partial z'}{\partial t'} - F_1(q) - F_2(q) = 0 \tag{5.21}$$

In this relation $F_1(q)$ denotes the erosion by the first strike of particles (the second term in equation 5.8) while $F_2(q)$ adds all the contributions to erosion of the second strike ($q = \partial z'/\partial x'$).

To calculate the second-strike term, it is necessary to trace the trajectories of the rebounding particles to find the impact sites at second strike. Since this ray tracing could not be performed analytically, the model had to be treated numerically.

As the previous chapter illustrated the literature gives little data on rebound characteristics of alumina particles from glass surfaces. Measuring the rebound parameters with a one-dimension Laser Doppler Anemometer has been only moderately successful. In absence of substantial data on particle rebound very simple rebound rules will be used in the model to prevent complication of the model. The rebound velocity for example is taken as a constant fraction (F_v) of the incident velocity with typical values for F_v between 0.2 and 0.5. The rebound angle is chosen as a factor (F_a) of the angle of incidence. Although chapter 4 (Figure 4.9) suggests a factor of 0.5, values in a range between 0.8 and 1.2 were used in the model to account for the airflow effect. To include some measure of the random character of particle impact a spreading angle was included (α) which is supposed to describe the width of the rebounding beam.

5.3.2   Numerical procedures

To enable a numerical solution the parameter space (x, t) was divided into equal time intervals and a number of equally spaced nodes with segments in between. The equation was solved with a slightly adapted Roe's algorithm, i.e. an explicit Euler time-stepping and a first-order upwind along the geometrical axis. For each segment the functions F_1 and F_2 were calculated using the slope q of the segment itself. The integration of equation 5.11 for each node uses the value of ($F_1 + F_2$) of the segment just upwind of the node. The sign of the wave velocity (A_{wave}) gives the upwind direction

$$A_{wave} = \frac{\partial(F_1(q) + F_2(q))}{\partial q}$$

(5.22)

The second-strike contribution was calculated using ray tracing. For each segment the direction of the rebounding beam is calculated using the angle of incidence. The segment where this beam impinges was sought. With the spreading angle (α_s) and the distance between the locations of the first and secondary strikes, a spreading width was calculated, which dictates the distribution of the erosion over a number of segments. For each of the initial segments a contribution was added to F_2 using the dimensionless form of equation 5.5, where $\sin(\theta)$ is replaced by the inner product between particle velocity vector and inward normal to the surface. The contributions over the width of the beam were weighed with a linear function using the distance from the centre of the beam.

The algorithm was implemented on a personal computer using Borland Delphi as a programming environment.
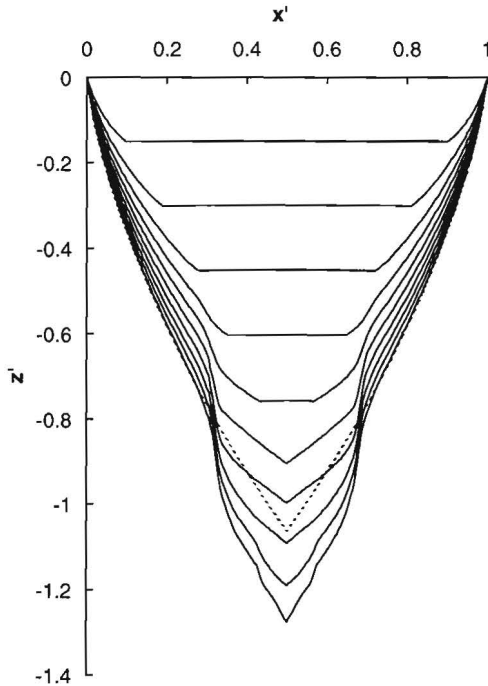
Figure 5-12: A typical solution of the extended model. The dashed line represents the analytical solution.

5.3.3   Solutions and conclusion

As Figure 5.12 shows, the model including second strike indeed forms dimples in the walls of the patterns. A comparison between the extended model and the analytical model (the dashed line in Figure 5-12) shows that the second-strike contribution is concentrated near the centre of the pattern. Near the boundaries the two solutions are comparable.

Figure 5-13 presents the results of a parameter study, showing the effect of variation in the power k, the rebound velocity factor F_v, the rebound angle factor F_a and the rebound spreading angle α.

As Figure 5-13 shows, the velocity-rebound factor has considerable influence on the size of the second-strike effect. This is obvious since the greater loss of kinetic energy at the first strike results in a lower second-strike contribution.
The rebound angle factor governs the width of the second-strike contribution; larger rebound factors give wider second-strike effects and because of the increased angle of impact at second strike, also greater overall effects. A smaller rebound-spreading angle increases the apparent second-strike effect, because the second-strike particles are more concentrated.

The velocity exponent k has a drastic effect, because an increase in k increases the angle of incidence (θ) at which a particle impact results in significant erosion.
Since the values of the most parameters are only known with a limited accuracy, we have chosen to perform the comparison between model and experiments with a fixed set of parameters ($F_v = 0.4$, $F_a = 1$, $\alpha = 3°$ and $k = 2.6$).
The angle-rebound coefficient ($F_a=1$) was deliberately chosen considerably higher than the one measured in section 4.5 to account for the airflow effect in these measurements.

5.4   Validation experiments

For verifying the calculated structures with experimental data, trench shapes were powder-blasted in AF45 (boro-silicate glass, Schott). To this end a 100-μm-thick, line shaped ORDYL mask (Tokyo Ohka Kogyo) was applied to the glass at a pitch of 600 μm and a line-width of 230 μm (see Figure 5-14). These samples were powder-blasted with a converted Schlick industrial sandblasting machine, using 23 μm alumina particles. The samples were exposed to different amounts of powder, resulting in a range of shapes characterising the evolution of the patterns.
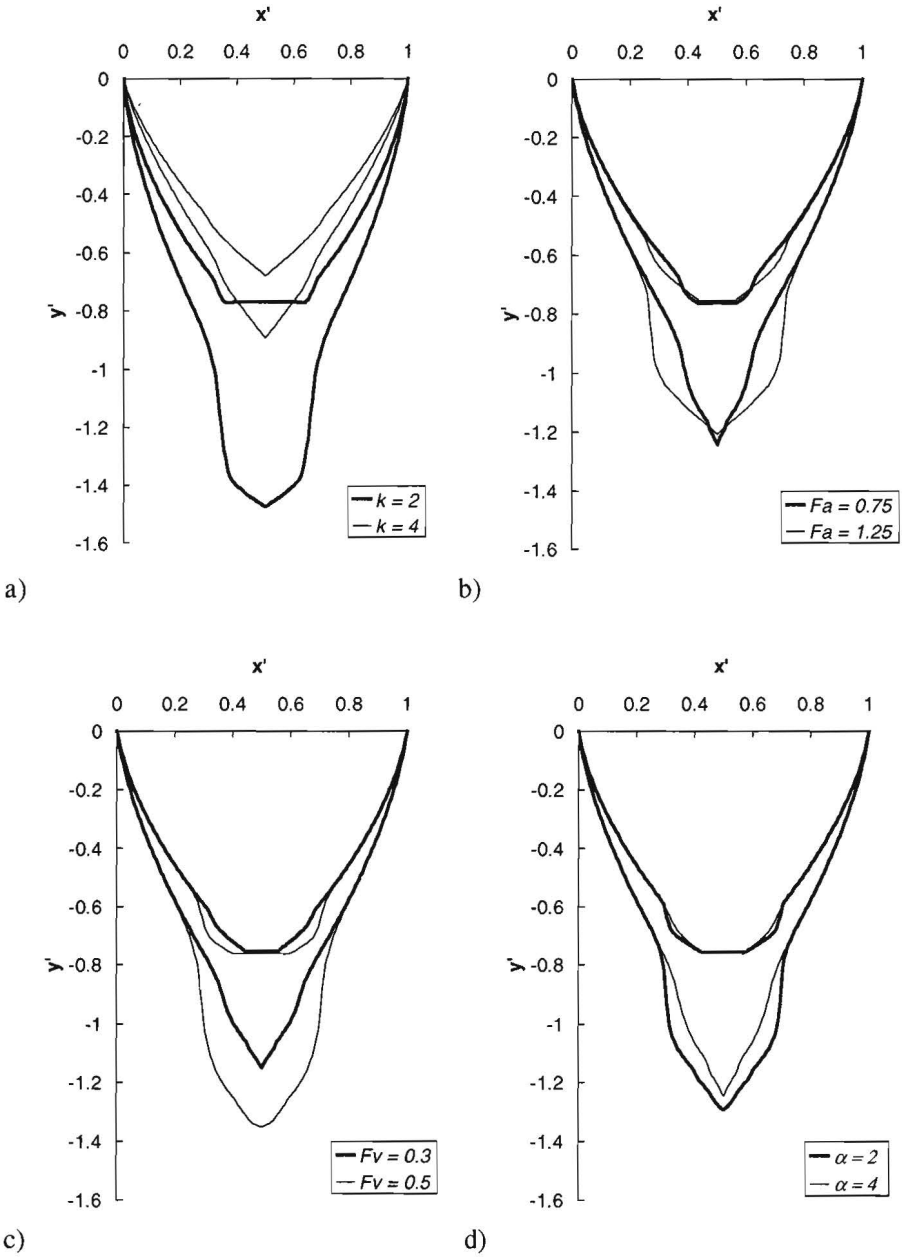
Figure 5-13: The results of the parameter study.

After removing the mask the samples are cross-sectioned. Since the samples have been covered with a thin layer of gold, optical microscopy in transmission produce images like the one presented in Figure 5-14. The cross-sections show two types of shapes: the trenches between the lines and the slopes at the ends of the line patterns. Illustrative in Figure 5-14 is the difference between erosion depth of the wide structure and the trenches.
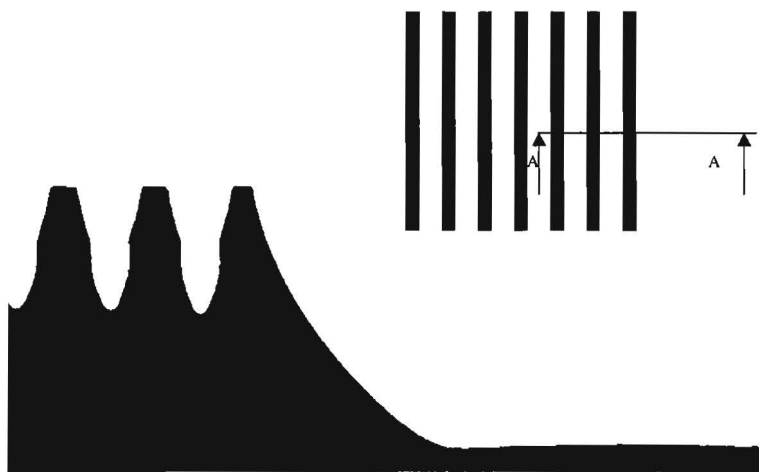
Figure 5-14: A cross-section A-A of the mask sketched in the right hand top corner after erosion. Remark the difference in eroded depth of the trenches and the homogenous part.

When the shapes are scaled with the width of the patterns as discussed in section 5.4, the trenches represent deep holes, while the slopes represent the wall effects of a shallow pattern. The images of all the samples were imported into an image-processing program (Image Pro Plus), which traced the shape of the geometry. The measured shapes of the slope and the trenches are presented in Figure 5-15 and Figure 5-16, respectively.

Since the slopes form part of a very wide structure, they represent the boundary solution presented in Figure 5-11. Scaling the curves in Figure 5-14 with their depth can check this. As a reference, the dashed curve represents the theoretical solution shown in Figure 5-11. The curves in Figure 5-15 show a reasonable conformity. At increasing erosion depths they change systematically and approach the theoretical curve.

A number of effects may be involved in this evolution of the scaled geometry. The model does not incorporate particle size effects. At greater erosion depths, the curvature of the shape reduces and so does the particle size effect.

The shape of the curve at the least erosion shows an indication of a flux-shadow near the boundary. The cross-section of the mask is initially rectangular, but the top corners become rounded quite early in the process, reducing the shadow effect of the mask. Since the surface evolves, the deviation created at the start of the process remains, but since the erosion increases the dimensions of the curve its relative contribution decreases.

The theoretical curve does not incorporate second-strike effects, which are visible in the experimental curves.
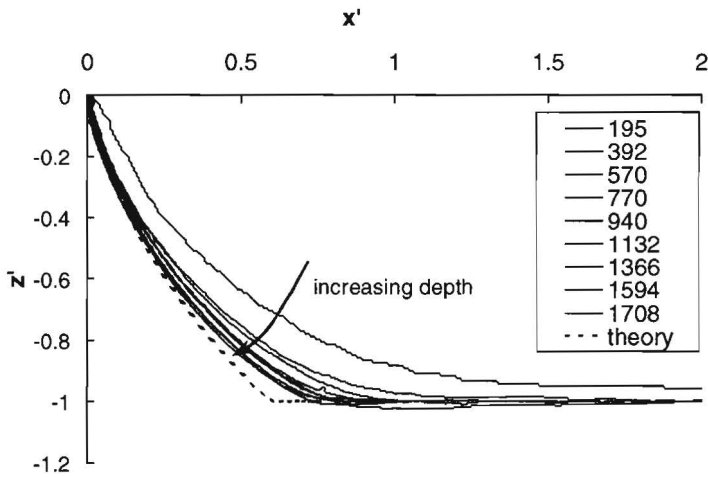
Figure 5-15: The experimental slopes scaled with the depth of the homogeneous erosion given in the legend in microns. The dashed line represents the analytical model.

Figure 5-16 combines the measured trench profiles. The experimental curves are made non-dimensionless using the procedure described in section 5.2.1. They show a distinct dimple shape and quite rounded "noses". They also show the mask wearing during the process, resulting in a widening of the top part of the geometry.

In Figure 5-17 the measured profiles are combined with calculated ones for dimensionless times up to $t'=2$. Although the calculated curves show comparable shapes (e.g. $t' = 1$ calculated and $t' = 1.5$ measured), the model does not compute profiles that are close to the measured ones. In the case of deeper patterns the deviation between model and experiment increases.
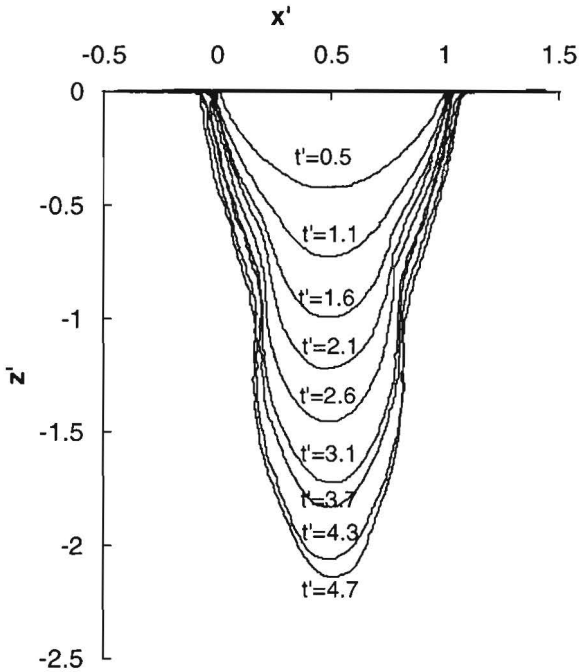
Figure 5-16: The experimental evolution of a trench. The solution scaled according the rules in section 5.2.1.

One of the dominant factors in this deviation is probably the absence of particle size effects in the model. The experimental shapes show rounded points with curvatures of about 50 μm, while the model predicts sharp points. Incorporating the effect of spatial hindering will reduce the calculated depth in favour of a rounded and wider tip.

Several other factors can be mentioned, which may contribute to the deviation between model and experiment. The effects of the non-ideal mask, like wear and shadowing by its thickness, have already been mentioned above. The description of erosion based on the normal component of the impact velocity also has limitations, as was shown in chapter 4.

The decision to use $z = z(x, t)$ in the numerical model for the description of deep holes with steep walls is not very fortunate. Especially since the experimental profiles are vertical and show a tendency to develop overhangs, the profile needs to

be modelled with a parameter description like $z = z(s,t)$, $x = x(s,t)$ with s being a parameter along the profile.
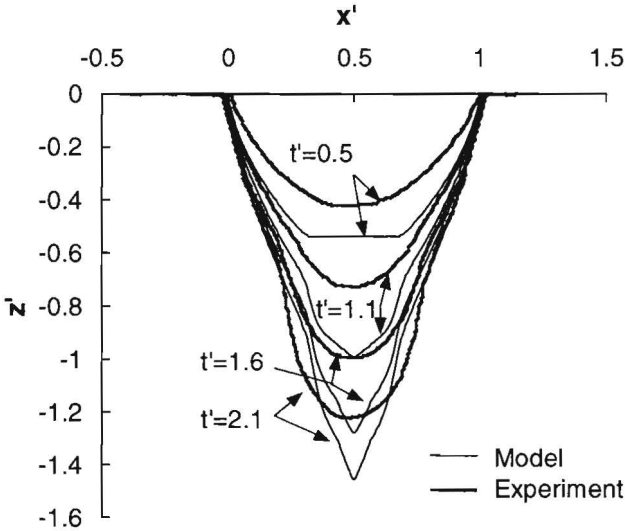
Figure 5-17: A comparison between experiment and extended model.

5.5 Conclusion

The model presented in this paper gives a good qualitative description of the development of powder-blasted structures. It shows that the forming of patterns in powder blasting is governed by the dependence of erosion on the impact angle. Rebounding particles provide a significant contribution.

The quantitative agreement between the calculated shapes and the measured ones is reasonable. This is probably attributable to the simplifications in the model, like the simplified description of the angle dependence of erosion and the omission of particle size effects and the effect of the presence of a mask.

An improvement of the model will require more quantitative experimental data on, for example, the angle dependence of the erosion and the rebound characteristics of particles. An improved model should also incorporate a parameterisation of the surface for a better description of steep walls.

The analytical model, although simple, can be used to obtain first-order predictions of the eroded shapes in complex mask patterns. The scaling rules derived from the model provide a valuable insight of the pattern formation. They show that to first order the shape of the patterns does not depend on the erosion conditions used; at a

certain depth to width ratio the shape of the pattern will be constant. For wide structures it shows that the width of the slopes at the sides of the pattern scales linearly with the depth of the homogeneous erosion.

The independence of shape on erosion conditions makes powder blasting an interesting industrial process, unless the obtained shape differs from the one desired.

5.6   *List of symbols*

A_{wave}	The dimensionless wave velocity of the hyperbolic differential equation, Equation 5.22.
C_{eff}	Pre-factor for the kinetic energy dependency of erosion efficiency [g/J^p], Equation 5.1.
E_{eff}	The erosion efficiency (mass of removed substrate per amount of kinetic energy of erodent used) [g/J], Equation 5.1 and Equation 2.18.
$F_1(q)$	The first strike contribution in the extended model, Equation 5.22.
$F_2(q)$	The second strike contribution in the extended model, Equation 5.22.
F_a	The angle rebound coefficient (= rebound angle/impact angle), Sections 5.3.1 and 4.5.
F_v	The velocity rebound coefficient (= rebound velocity/impact velocity), Sections 5.3.1 and 4.5.
J	The flux of kinetic energy in the abrasive jet [J/s], Equation 5.2.
L^*	The characteristic length scale (for the trench problem $L^* = W$), text above Equation 5.7.
W	The width of the channel geometry [m], Figure 5.3.
k	Exponent in the surface evolution equation (= $2p+2$), Equation 5.6.
m	The mass of an abrasive particle [kg], Equation 5.1.
n	The inward directed, local normal vector to the eroded surface, Figure 5.3.
p	The exponent of the kinetic energy in the relation for the erosion efficiency [-], Equation 5.1.
q	The local slope of the eroded surface ($=\partial z/\partial x$) [-], Equation 5.9.
q_0	The local slope of the initial surface ($=\partial z/\partial x|_{t=0}$) [-], Equation 5.11.
s	The parameter describing the position along the surface [-], Below Equation 5.9.
t	Time [s], Equation 5.2.
t^*	The characteristic time scale for the surface evolution [s], Equation 5.7.
t'	The dimensionless time scale (= t/t^*) [-], Equation 5.8.
t_0	The time at the start of an erosion experiment [s], Equation 5.11.
v	The velocity vector of an impacting particle [m/s, m/s], Figure 5.3.
v	The velocity of an impacting particle [m/s], Equation 5.1.
v_{jet}	The velocity of the abrasive particles in the jet [m/s], Equation 5.5.
v_n	The component of velocity normal to the substrate surface [m/s], above Equation 5.5.

x The coordinate along the original surface [m], Figure 5.3.

$\mathbf{x}$ Vector describing the position of a point on the eroded surface, Equation 5.2.

x' The dimensionless x coordinate $(= x / L^*)$ [-], Equation 5.8.

x_0' The dimensionless x coordinate of the root of the characteristic [-], Equation 5.11.

z The coordinate perpendicular to the original surface [m], Figure 5.3.

z' The dimensionless z coordinate $(= z / L^*)$ [-], Equation 5.8.

z_0' The dimensionless z coordinate of the root of the characteristic [-], Equation 5.11.

Φ The mass flux of abrasive particles at a local part of the surface [kg/s], Equation 5.3.

Φ_{jet} The mass flux of abrasive particles in the jet [kg/s], text below Equation 5.3.

α The rebound spreading angle, section 5.3.1.

δ The dimensionless width of the flux boundary [-], Figure 5.5.

ε The curvature at the boundary points of the initial geometry [m], Figure 5.9.

θ The local angle of incidence of the abrasive particles [°], Figure 5.3.

ρ_t The specific mass of the substrate [kg/m^3], Equation 5.2.

5.7 Literature

1   G. Carter, M.J. Nobes, K.I. Arshak, *The application of erosion slowness theory to prediction of surface contour generation during particulate ablation of solids*, Wear 53 (1979) 245-261.

2   G. Carter, M.J. Nobes, *A kinematic wave description of ripple development on sand-blasted ductile solids*, Wear 96 (1984) 227-238.

3   G. Carter, J.S. Colligon, M.J. Nobes, *Analytical modelling of sputter induced surface morphology*, Radiation Effects, 31 (1977) 65-87.

4   P.J. Slikkerveer, P.C.P. Bouten, F.H. in 't Veld, H. Scholten, *Erosion and damage by sharp particles*, Wear 217 (1998) 237-250.

5   R. Courant and D. Hilbert *Methods of mathematical physics,* Vol. 2, Interscience, New York (1962).

6   P.J. Slikkerveer, J.H.M. ten Thije Boonkkamp, *Mathematical modeling of erosion by powder blasting*, submitted to Surveys on Mathematics for Industry (1999).

6 Erosion of elastomeric masks[*]

For patterned erosion the parts where no erosion is wanted, need to be shielded from solid particle impact. Since no material is insensitive to erosive wear, for high quality results a masking material is needed with minimum erosion.

Of all materials, elastomers show the best erosion resistance. These materials are of interest since photosensitive variants exist that enable a precision patterning by photolithography obtaining high accuracy in both shape of geometry and in position.

This chapter studies the erosion mechanism of elastomeric materials. A study of the literature reveals that the wear mechanism of elastomers differs from that of ductile and of brittle materials. The erosion behaviour of three photo-sensitive materials is determined to show these differences. From the results a model is derived for the erosive wear of masks, comparable with the one derived in chapter 5 for the eroded pattern itself.

6.1 Introduction

In environments where high-speed airborne particles may hit surfaces there is a need for protective coatings to decrease or prevent solid particle erosion of these surfaces. The field of application includes aircraft structures, equipment for pneumatical transport of granular material and mechanical etching by powder blasting. Coatings with minimal erosive wear are needed for optimum protection, which is why much use is made of elastomeric coatings.

Characterisation and ranking of the erosion resistance of materials of this type is complex. The erosion of ceramics is well described by brittle material behaviour and that of metals by a ductile mechanism. Polymeric materials, to which elastomers belong, may show brittle, ductile or rubber-like erosion behaviour, depending on temperature and deformation time scale.

This paper illustrates the complexity of erosion characterisation by studying the behaviour of three coatings intended as masking material for powder-blasting processes [see e.g. ref. 1]. This application requires a high erosion resistance, but apart from that, the materials must also be photosensitive to enable photolithography and they must retain their resistance in discontinuous layers.

After reviewing the literature and describing the experimental procedures, we will determine the erosion behaviour of the three materials as a function of particle velocity and impact angle. Using the erosion data determined for the materials, the paper derives a model for the erosive wear of elastomeric surfaces. Applied to discontinuous coatings, this model predicts an unexpected wear behaviour that has, however, been verified by experiments.

6.2 A review of the literature

6.2.1 Classification of erosion behaviour

The erosion mechanism of rubber-like materials differs fundamentally from that of brittle materials or ductile materials. Unlike ceramics [e.g. 2] or brittle polymers as PMMA and bismaleimide [3, 4, 5], no lateral cracks are formed in elastomers. Neither do rubbers show any evidence of cutting or ploughing wear as found in metals of ductile plastics such as polyethylene and polypropylene [6, 7]. Single impacts seem to cause no visible damage at all [8], which is in agreement with the incubation time observed in the erosion process before a steady state is established [8, 9, 10, 11]. In this incubation time the substrate may even add some weight as particles becoming embedded in the surface. Tilly [12, 13] observed the existence of an incubation time in the case of polyurethane (PU) elastomers. The incubation time is found to decrease with increasing brittleness [9]. It is specifically present at normal impact and decreases with the angle of attack [14, 11].

At oblique impact, maximum erosion is found at glancing impact, as with ductile materials. The erosion rate of polyurethanes, for example, is found to differ by an order of magnitude between normal impact and 30° incidence [15]. The surface structure is also quite different. During oblique erosion, ridges form perpendicular to the direction of the incoming particles. These ridges resemble those observed in sliding wear of rubbers [16]. They are detected with harder rubbers but not with softer ones [11]. The ridges run perfectly parallel at low impact velocities and start to crumble at higher velocities [8].

The distinction of polymeric materials showing brittle, ductile or rubber-like behaviour in erosion using the phenomena mentioned above is not always straightforward, because materials may show a combination of two different types of behaviour. In oblique impact, for example, brittle PMMA and polystyrene show a second maximum at about 20 degrees incidence beside the maximum at normal impact. This second maximum may be caused by a plastic erosion mechanism [17]. Some "ductile" polymers like polycarbonate and PTFE [18], and sometimes polyethylene [6, 18], show an incubation time characteristic of rubber-like erosion behaviour.

The difficulty in erosion classification is fundamental to polymeric materials. Depending on the temperature and rate of deformation, the same material might behave dominantly ductile, rubber-like or brittle [see e.g. 19]. Allowance should be made for this changing material behaviour when translating erosion test results to practical situations. Preferably tests should be performed under conditions comparable with those of the practical situation.

The complex behaviour and the variety of material properties of the rubber-like materials make it difficult to compare results reported in the literature [18, 20]. This is further complicated by the range of different types of erosion tests used (for a review see [21]). Also erodents of different materials and sizes are used among which iron pellets [5], glass beads [17] and silica or alumina particles [11, 12, 13, 14] with sizes from 120 μm [20] to 4 mm [5] and impact velocities varying from 40 m/s [22] up 500 m/s [23].

Not all papers refer to the presence of an incubation time, so it is unclear whether the measured erosion rates hold for the steady-state erosion process.

The testing method used may also introduce a specific wear pattern. In one of the common erosion test methods, in which the nozzle is held at a fixed position relative to the sample [3, 6, 9, 11, 17, 18], characteristic plateau-shaped craters are formed in polymers. The plateau forming has been observed for a variety of materials: elastomers such as polyurethane [24], ductile targets like PTFE [18, 24] and more brittle ones like polycarbonate [18]. Material is removed as a result of

lateral crack growth near the edges of plateaus and the removal of fragments from the edges of these plateaus [17]. In the case of polyurethane, subsurface cracks have been observed [25]. This plateau formation is specific to this type of test method and its effect on the measured erosion rate is unclear.

6.2.2   Erosion correlation

Quantitative comparison of experimental data is hence difficult, but the correlation obtained from ranges of experiments yields valuable information.
The erosion resistance of rubbers is not correlated with cavitation erosion or sliding wear [20]. Its dependence on modulus is even opposed to that of sliding wear, where a higher modulus increases resistance [8, 15].

In the transitional region between brittle materials and rubbers a low brittleness index correlates with low erosion [9, 26]. The brittleness index is defined as the ratio of material hardness and fracture toughness. An attempt to extend this concept to semi-brittleness to describe the angular dependence of erosion at oblique impact was not successful in the case of elastomers [27].

Hutchings et al. [11] found that a high rebound-resilience resulted in good erosion resistance, the rebound resilience being defined as the ratio of the rebound height and the height from which a steel ball fell onto the substrate. For the eight unfilled rubbers and polyurethanes tested, they found a correlation with the rebound resilience (RR)

$$E_r \therefore (1 - RR)^{1.4} \tag{6.1}$$

with E_r being the erosion rate defined as the weight removed from the substrate per weight impacting particles. At constant rebound resilience, a low material hardness correlates with a good erosion resistance for a range of polyurethane elastomers [15]. Low brittleness index, high rebound resilience and low hardness correlate partly with a low glass transition temperature, which is also mentioned separately as correlating with good erosion resistance [11].
Other parameters correlating with high erosion resistance are high yield stress [9], low modulus [3, 18, 20], high strain to failure [3, 9, 18, 20], high impact strength and high degradation temperature [3, 18]. Two papers [28, 29] mention high breaking energy as a measure of high erosion resistance. The breaking energy, being the amount of energy stored per volume of material at breaking, is the product of the stress and the strain at the instant of breaking.

Chemical degradation or oxidation of the rubber seems to be important only at very low erosion rates. Degradation visible as a change in colour around impact craters

[3, 18] was confirmed with infrared spectroscopy [14] at a very low powder flux. At a moderate or high flux no chemical degradation of the surface was observed. The erosion apparently removed the degraded material too fast to be measurable.

6.2.3   Fatigue-based models

The presence of an incubation time, the patterns of surface and subsurface cracks [8] and the resemblance between the surface pattern at oblique impact and sliding wear patterns that are known to be fatigue-based [30], indicate that the erosion of elastomers is based on a fatigue mechanism. The correlation of erosion with rebound resilience [8] agrees with the dependence of polymer fatigue life on mechanical damping in the material [19].

Arnold and Hutchings set a first step towards modelling rubber erosion on the basis of fatigue. They presented two models: one for normal impact [31] and another for oblique impact [32].

The model for normal impact [31] starts at the fatigue crack growth measured on a fatigue tester. It assumes the surface of the substrate to be covered with a large number of micro-cracks. The stresses of one particle impact result in slight growth of these micro-cracks. In a steady state the growth of the micro-cracks balances the loss of material at the surface.

The model considers friction between a particle and the substrate to be the driving force behind erosion, since Hertzian indentations of incompressible materials (having a Poisson ratio (v) of 0.5) do not generate radial surface stresses. The model gives the following correlation between erosion rate (E_r) and the erodent properties

$$E_r \therefore R^{\beta-1} v^{2\beta} \rho^{\beta-1} \tag{6.2}$$

where R is the particle radius, v its velocity and ρ its specific mass. The exponent β was found to be between 2 and 8 in rubber fatigue tests.

The model at oblique impact [32] is based on the theory for sliding wear of rubbers with steel blades developed by Southern and Thomas [16]. It regards each particle as a small blade sliding across the surface. Using the crack growth theory of rubbers, the model arrives at

$$E_r \therefore \rho^{\frac{\beta-1}{2}} v^{\beta+1} R^{\beta-1} E^{\frac{\beta-1}{2}} F(\theta) \tag{6.3}$$

Here E is the modulus of the target material and θ is the angle between the incident beam and the substrate surface. $F(\theta)$ is a short for the complex functions describing

the impact angle dependence of erosion; one for small impact angles and one for larger ones.

The models were verified in [31, 32] using three types of rubbers (natural rubber (NR), styrene butadiene rubber (SBR) and butyl rubber (BR)). The crack growth exponent β of the materials was inferred from fatigue exponents and from the velocity and size exponents at normal and oblique impact (see *Table* 6-1).

Table 6-1: A comparison of the values of β determined in different ways for normal and oblique impact [31, 32].

Material	β Tensile fatigue experiments	β Velocity exponent		β Size exponent	
		Normal incidence	Glancing incidence	Normal incidence	Glancing incidence
NR	2.0	1.8	2.1	2.0	1.9
SBR	4.6	2.5	2.9	2.3	2.9
BR	7.9	3.2	4.4	-	-

The table shows the values of the exponents measured in different ways. Some correlation is observable but values may vary to over a factor 2. Since the oblique model also predicts maximum erosion at an impact angle of about 30 to 40 degrees, whereas the measurements show maximum erosion at (less than) 15 degrees, the models although being of fundamental interest, are still unsuitable for material selection.

6.3 Characterisation three photo-sensitive elastomers

6.3.1 Experimental procedures

The three materials tested here have been selected for their suitability as a powder-blasting mask in a pre-screening test. They aptly represent the materials commercially available. One of the materials is a 100 μm thick laminate intended for use as a dry-film resist for powder blasting (Ordyl BF 410, Tokyo Oga Kogyo, Japan). The second material (LF55G1, Grace, France) was developed for the production of patterning plates for flexographic printing, while the last material (Ebecryl 270, UCB Chemicals, the Netherlands) is a half-fabricate of a well-known composition commonly used in the chemical industry. All the materials are based on polyurethane acrylates and can be patterned by means of photolithography.

Before the erosion tests the first material is laminated on a glass substrate, UV cured and post baked. The last two materials are liquids and applied to the glass

substrate using a doctor blade process to a thickness of about 100 μm before UV curing. The UV curing has been performed in accordance with the suppliers instructions.

The mechanical behaviour of the materials is characterised using Dynamic Mechanical Thermal Analysis in the tensile mode (DMTA Mk3, Polymer Laboratories). For this, freestanding films were prepared of the liquid substrates by spin-coating the material on a non-adhesive glass substrate, followed by UV illumination in nitrogen. The material is then peeled off the substrate.
In the DMTA samples of 8 mm by 10 mm by approximately 100 μm were exposed to a sinusoidal strain with amplitude of 16 μm at 1 Hz, while the required force and the phase difference between the force and the strain were recorded. The values obtained were used to compute the elastic component of the modulus (E') and the loss tangent (tan δ), being the ratio of plastic dissipation and elastic storage.
The accuracy of the determination of E' depends to a large extend on the accuracy of the sample dimensions. In the case of LF55G1 and Ebecryl 270 this is specifically important because the thickness homogeneity is not controlled very well. Although this leads to an uncertainty in E' of about a factor of 1.5, the shape of the individual curves will be considerably more accurate.

For the erosion tests coated glass substrates were cut into samples of 5×5 cm^2. By scanning a nozzle with a diameter of 1.5 mm across these samples an area of 3.5×3.5 cm^2 was homogeneously eroded. The scan rates in the x and y directions were 900 mm/min and 20 mm/min, respectively, with the nozzle-substrate distance is kept at 40 mm. The abrasive particles (29 μm Al_2O_3) were fed to the jet by a HP–1 abrasive jet machine (Texas Airsonics, Corpus Christi, Texas, USA) at a low mass flux of about 10 gram/min to limit the particle flux effect [33].
The average particle velocity could be varied between 50 and 250 m/s by adjusting the air-pressure. This velocity was monitored during the erosion process using a one-dimensional Laser-Doppler Anemometer (Dantec FlowLite and BSA, Skovlunde, Danmark) at about 1 cm above the surface.
The powder flux of the abrasive jet machine was recorded by placing the entire abrasive jet machine on a balance (Mettler PM 30-K) and monitoring its weight loss in time accurately to 1 gram. The loss in weight of the substrates was determined using a Mettler analytical balance (type 1801, accurate to 0.1 μg).

All three materials show an incubation time in erosion rate. Since the erosion rates in this chapter are defined by the value of the steady-state process, the weight loss of the sample must be determined at several moments during an experiment,

making determination of the erosion rate very time-consuming, especially in case of thin coatings. Figure 6-1 shows an example of the erosion rate determination. As reported in the literature the sample weight first increases as a result of the embedding of particles in the coating. Later a steady state is reached. The erosion rate is determined per interval. The erosion value is obtained by fitting the "horizontal" part of the line.
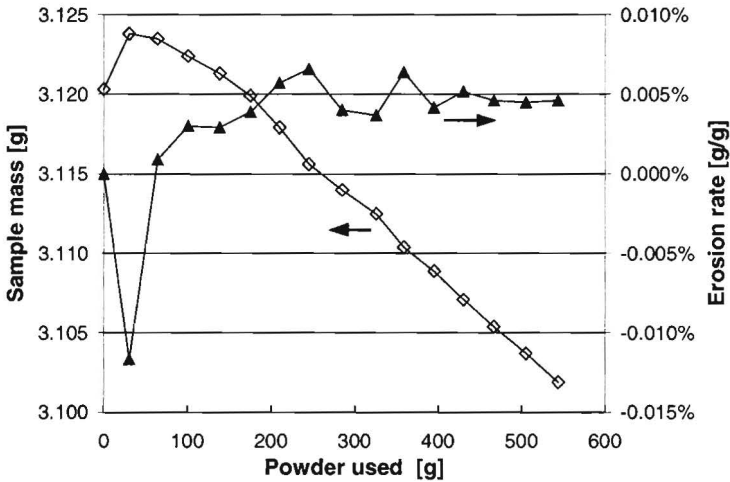
Figure 6-1: An example of the results of an erosion experiment.

Particles embedding in the substrate surface will locally influence the properties of the coating materials. The effect on the erosion rate will however be limited, since the embedded particles cover only a few percent of the substrate surface (e.g. 4% calculated from the weight gain shown in Figure 6.1).

6.3.2   Experimental results

Mechanical properties
Figures 6.2 and 6.3 summarise the DMTA results. Figure 6-2 compares the temperature dependencies of the elastic modulus of the three materials and Figure 6-3 compares the loss tangents. The curves in the figures are characteristic of polymeric materials showing a glassy behaviour at low temperatures and a transition to a rubbery stage. The glass transition temperatures (T_g) of Ebecryl 270 and LF55G1 are obtained from the peak in tan(δ) as 10 °C and −35 °C, respectively. BF410 shows two steps in log E' and two peaks in the tan(δ) trace. This is indicative of a two-phase system, with one phase having a T_g of −20 °C and the other phase a transition at 110 °C.
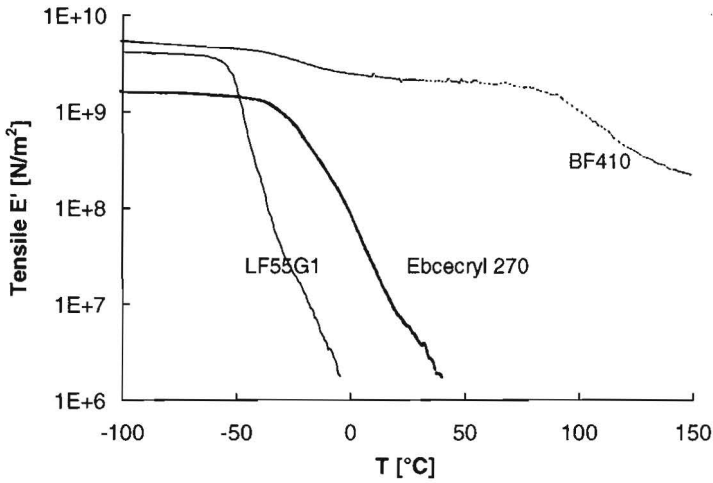
Figure 6-2: E' as a function of temperature for LF55G1, Ebecryl 270 and BF410.
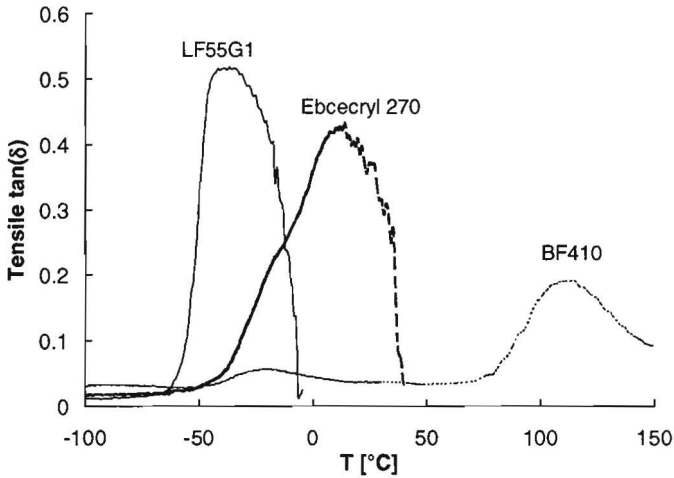
*Figure 6-3: The loss tangent (tan δ) as a function of temperature for LF55G1,
Ebecryl 270 and BF410.*

In determining the mechanical properties of coatings at solid particle impact it is important to account for the effect of deformation rate on the material properties. Using time-temperature substitution [19] the effect of deformation rate can be exchanged for a thermal effect; a 4-6 °C decrease in temperature for each order increase in the deformation rate. With a deformation timescale of 10^{-7} to 10^{-8} s

estimated by Hertzian impact depth and the impact velocity, the mechanical properties at room temperature and particle impact are comparable with 1 Hz deformation at –10 to –20 °C.

In this situation the relative energy loss at impact for LF55G1 and Ebecryl 270 will be comparable, both being considerably larger than that of the Ordyl BF410, as can be seen in Figure 6-3. The modulus of LF55G1 is in this situation considerably lower than those of Ordyl and Ebecryl. The LF55G1 coating differs from the other coatings in being above its main glass transition temperature and can be expected to behave most "rubber-like".
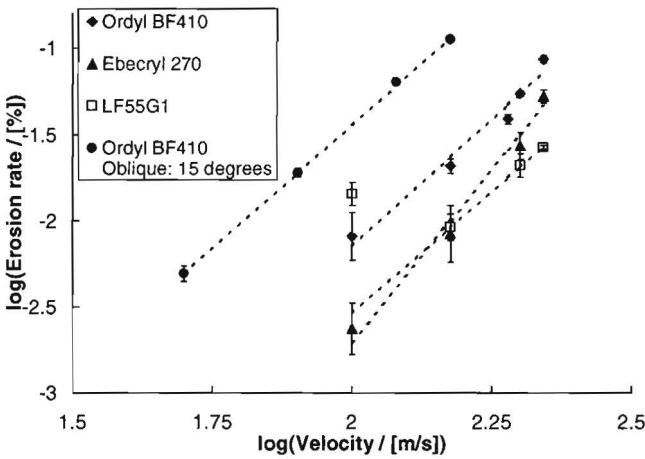
Figure 6-4: Erosion dependence on velocity measured for the three materials.

Velocity dependence of erosion

Figure 6-4 presents the erosion dependence on velocity at normal impact for the three materials. The velocity dependence of Ordyl BF410 at glancing impact (15 degrees relative to the substrate) is also included. The figure clearly shows the increased erosion at glancing impact.

The lines represent least-squares fits to the data obtained using a power law ($y = a \cdot x^b$, with a and b fit parameters). The obtained fit parameters are summarised in Table 6-2. As Figure 6-4 shows the power law fits the data reasonably except for the LF55G1 at 100 m/s. The deviation was found to be reproducible. The reason for it is, however, unclear.

The data show that the velocity exponents of the Ordyl and the Ebecryl samples at normal impact are comparable with those at oblique impact of the Ordyl sample.

The Ebecryl, however, shows a significantly higher velocity exponent. The models of Arnold and Hutchings predict a difference in velocity exponent at normal and oblique impact (2β at normal impact and $\beta+1$ at oblique impact, see equation 6.2 and 6.3). The fit parameter b of Ordyl does not show clear signs of such a difference between oblique and normal impact. The data available are, however, too limited to be conclusive.

Table 6-2: Fit values for the erosion rate versus velocity at normal impact ($E_r = a \cdot v^e$).

Coating	a	e	R^2
Ordyl BF410	$8.9 \cdot 10^{-9}$	2.96	0.95
„ 15 degrees	$6.5 \cdot 10^{-8}$	2.87	0.99
LF55G1	$1.9 \cdot 10^{-11}$	4.00	0.93
Ebecryl 270	$6.5 \cdot 10^{-9}$	2.86	0.93

Oblique impact

Figure 6-5 combines the erosion results at oblique impact of the three materials measured at an impact velocity of 180 m/s. All the materials displayed a maximum in the erosion rate at glancing impact at around 15 degrees relative to the substrate. The erosion rate of the Ordyl BF410 sample increases drastically at oblique impact. The erosion rate values at 15 and 30 degrees could not be measured directly, since the coating was removed before a steady state could be observed. The erosion rate value at 15 degrees was calculated via slight extrapolation of the velocity dependence of erosion (see Figure 6-4). This could not be accurately done for a 30 degrees impact angle.

The oblique impact results in Figure 6-5 clearly show the difference in erosion resistance of the three coatings. A closer look reveals that the curves do not differ by a constant factor, but that the increase in erosion with impact angle to a great extend depends on the coating material. The data are fitted with the following equation to quantify the differences

$$E_r = c\left(1 + d \cos^f \theta\right) \qquad (6.4)$$

with c, d, and f being fit parameters. The simple relation was selected for fitting the limited amount of data available. The oblique impact model of Arnold and Hutchings (equation 6.3) is far too complex for this. For the same reason the (not-measured) absence of erosive wear at zero impact angles was omitted from the fit equation.

The fit parameter c can be interpreted as the erosion rate at normal impact, d as the ratio of erosion rate at oblique impact and at normal impact and f a coefficient

describing the transition from oblique to normal impact erosion rate. The fit parameters obtained are presented in Table 6-3.
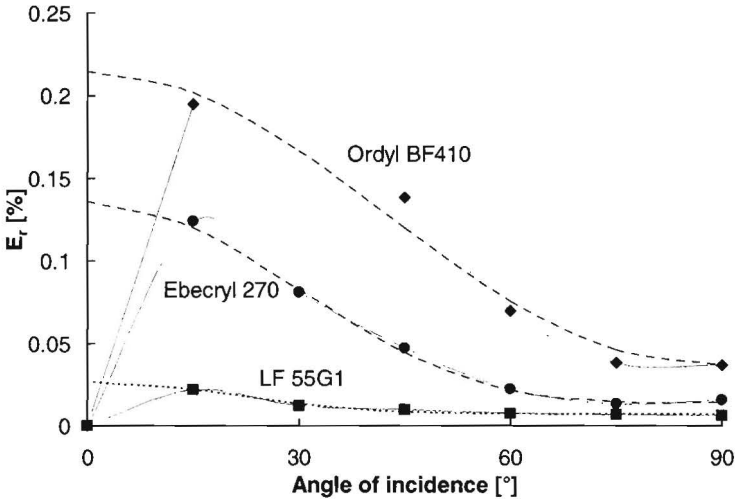
Figure 6-5: The erosion rates of Ordyl BF410, Ebecryl 270 and LF 55G1 as a function of the impact angle at 180 m/s impact velocity. The dashed lines represent the fit with equation 6.4.

As Figure 6-4 shows, is the erosion at normal impact a strong function of impact velocity, which translates to the parameter c being a function of velocity. There is insufficient data to conclude whether the fit parameters d and f depend on velocity. Equation 6.4 must therefore be treated as a fit for an impact velocity of 180 m/s.

Table 6-3: Fit data at oblique impact

| | c | d | f |
	[%]	[-]	[-]
Ordyl BF 410	0.037	4.8	2.2
Ebecryl 270	0.014	8.7	4.0
LF 55G1	0.0072	2.7	8.0

The fit parameters in Table 6-3 clearly show the difference in the increase in the erosion rate with the angle of impact. The erosion of LF55G1 increases by a factor 2.7 only, whereas that of Ebercryl increased by 8.7. The increase factor of 4.8 found for Ordyl might be lower than the true value. The erosion curve suggests a maximum around 30 degrees. Since no erosion value is available for this maximum, the maximum could not be considered in the fit.

Although the values of exponent f obtained in the fitting of the oblique data are within the range obtained in fatigue tests shown in Table 6-1 and they show some correlation with values obtained from the velocity dependency of erosion, the models are apparently still too unrefined to allow quantitative comparison of data.

6.4 Erosion model

The oblique erosion experiments show a considerable difference in erosion behaviour between the three coatings. To study the effect of this different erosion behaviour this section derives an analytical evolution model for the eroding surface of the coating. The results are verified by comparing model predictions and experimental results for a non-continuous coating/mask in a powder-blasting process.

6.4.1 Analytical model

Starting from equation 6.4, an erosion model can be built that describes the erosion behaviour of protective coatings under practical conditions. In these situations the angle of impact may depend on the position of the surface and may also change with changes in the eroding surface. Although the model derived has a more general use, we will use it here to model the erosion of a powder-blasting mask. The model starts with an erosion relation differing from that of the pattern formation in brittle materials [34, 35]. The model is derived from the erosion equation in an analogous way.

Figure 6-6 sketches a geometry characteristic of the powder-blasting process. A patterned elastomeric mask with a certain height and width is created on a brittle substrate. The model assumes the presence of a(n infinitely) small curvature ε at the top corners of the mask. The mask-substrate combination is uniformly exposed to a flux of erosive particles (Φ [kg/m^{2}s]) normal to the substrate surface. In this environment both the brittle material and the mask will start to erode.
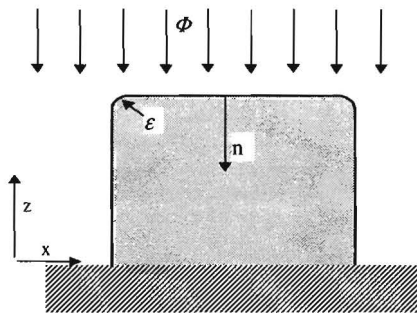
Figure 6-6: A schematic representation of the powder-blasting mask geometry.

The erosion velocity of the rubber surface ($\partial \mathbf{x}/\partial t$, [m/s]) in the direction of the inward normal to the surface ($\mathbf{n}$) can be calculated from the erosion rate (E_r) by multiplying it by the erodent particle flux at the surface (Φ) and dividing it by the specific mass of the rubber [ρ_t, kg/m^3].

$$\frac{d\mathbf{x}}{dt} = \frac{E_r \Phi}{\rho_t} \mathbf{n} \tag{6.5}$$

Please note that the erosion rate (E_r) is a function of the angle between the incident beam and the normal to the surface. For convenience we will describe the geometry of the surface during erosion as $z = z(x,t)$. Transforming relation 6.5 to this coordinate system requires the incorporation of the decrease in particle flux at oblique angles and the transformation from the inward normal of the surface to the z-coordinate. Incorporating all this we obtain an evolution equation of the surface of the geometry.

$$\frac{\partial z}{\partial t} = \frac{\Phi}{\rho_t} c\left(1 + d\cos^f\theta\right) = \frac{\Phi}{\rho_t} c\left(1 + d\left(\frac{\frac{\partial z}{\partial x}}{\sqrt{1 + \left(\frac{\partial z}{\partial x}\right)^2}}\right)^f\right) \tag{6.6}$$

In the second part of the relation the $\cos(\theta)$ is replaced with its representation in the x-z coordinate system. The above equation is a first-order, non-linear, hyperbolic partial differential equation, which can be solved using the method of characteristics [35, 36].

This results in a parameter representation of the evolution equation for each point on the original surface as a function of its initial position and its initial slope ($q = \partial z/\partial x |_{t=0}$).

$$x|_t = x|_{t=0} - t\,c\,\frac{\Phi}{\rho_t}\frac{\beta|q|^f}{q}\frac{d}{\left(1+q^2\right)^{f/2 + 1}} \tag{6.7a}$$

$$z|_t = z|_{t=0} - t\,c\,\frac{\Phi}{\rho_t}\left(1 + \frac{d|q|^f}{\left(1+q^2\right)^{f/2}} + \frac{df|q|^f}{\left(1+q^2\right)^{f/2 + 1}}\right) \tag{6.7b}$$

6.4.2   Analytical results

The evolution of the mask surface can be constructed with the aid of the parameter description (equation 6.7). Note that the curvatures of the top edges of the initial geometry are required to generate a continuous range of slopes ($-\infty < \partial z/\partial x < \infty$).

In the calculation we assume that such rounding is present, but is has a very small radius ($\varepsilon \to 0$).

Figure 6-7 shows the predicted erosion behaviour of a 100 μm wide line of 100 μm thick material eroded at the conditions used for determining the angle dependence of erosion presented in Figure 6-4 (alumina F320 particles at 180 m/s).

The figures show several remarkable features. First, it confirms the earlier ranking of the materials in erosion resistance. The Ebecryl 270 is more resistant than the Ordyl BF410, but the LF55G1 is evidently the most resistant.

They show a sudden change (a mathematical shock) in slope at the top end of the geometry separating the erosive wear from the top of the geometry and the wear originating from curvature at the top corners. The profiles of more advanced erosion of Ordyl and Ebecryl surprisingly show that the patterns seem to be eroded sideways. A study of the equations reveals that this erosion is caused by oblique impact erosion initiated at the edges of the initial geometry. The horizontal lines near the top of the structure show that only a limited amount of material has been removed by normal impact erosion from the top, relative to the amount of material eroded from the sides. The maximum thickness can be seen to decrease swiftly, as soon as the wear from the sides of the geometry meet.

The decrease in the mask width observed in the two less resistant materials is an unwanted phenomenon, as it means a loss of definition in the erosive etched pattern in the brittle substrate. The figures show that definition loss occurs in these materials quite early in the process, when the mask thickness itself is more than sufficient for protection.

That the difference in erosion resistance of the three materials is not related only to the erosion velocity at normal impact is illustrated in Figure 6-8. Here the profiles of the three materials are given at the instant that they have an equal amount of material removed at normal impact. The LF55G1 displays the least sidewards erosion, while Ebecryl 270 shows the most, which is consistent with the ratio between oblique erosion rate and the normal one (coefficient d in Table 6-3). As for good erosion resistance of powder-blasting masks, the model shows that the material's resistance at oblique impact is probably more important than its resistance at normal impact.

It is interesting to note the agreement between the profiles obtained after solid particle erosion of rubbers and those obtained in much smaller dimensions as result of sputtering [see for example 37, 38, 39]. Comparable impact angle dependence of erosion results in comparable surface evolution and models have been derived to describe this evolution in 2D and 3D.
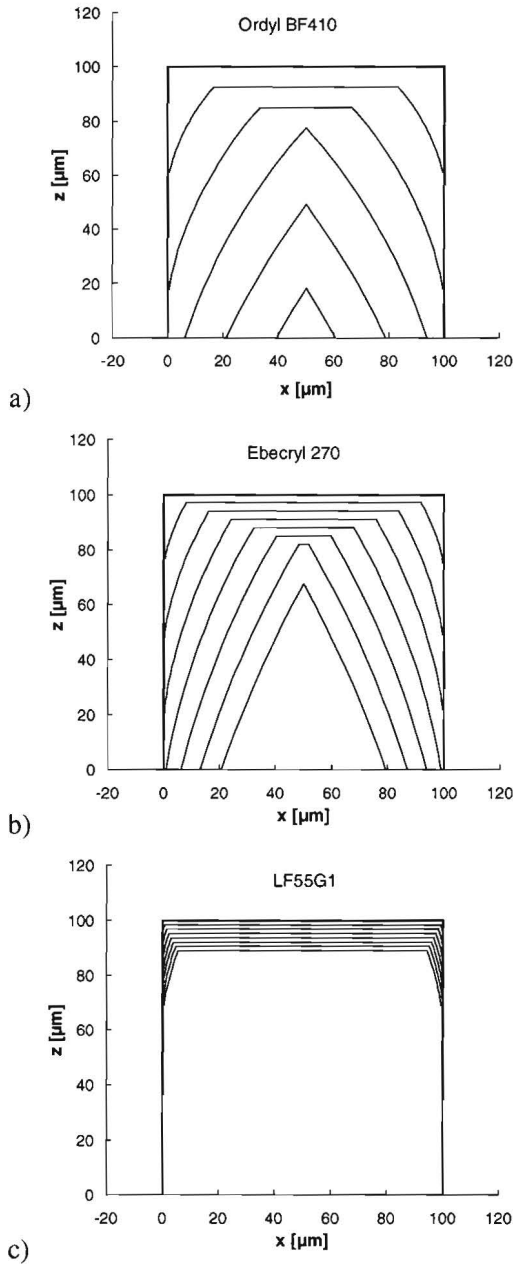
Figure 6-7: The predicted evolution of a 100 μm thick, 100 μm wide mask profile during powder blasting at 180 m/s. The lines represent a powder dose of 2 g/cm²: a) Ordyl BF410, b) Ebecryl 270 and c) LF55G1.
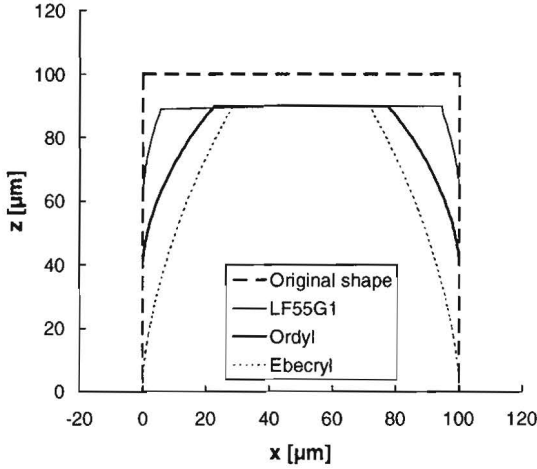
Figure 6-8: Comparison of the erosion profiles of the three materials at equal erosion from normal impact.

The results obtained above used a fit of the erosion dependence on impact angle that does not describe zero erosion at a zero impact angle (see Figure 6-5). By multiplying the fit relation (equation 6.4) with $\sin(\theta)^{\alpha}$, refitting the experimental data and deriving the erosion model for the new, more complex equation, it was verified that the model presented here does not differ significantly from this extended model. The solutions of the two models differ only near the vertical walls of the pattern, the simple model presented here giving a smooth transition between the "corner effect" zone and the vertical and the extended model showing a discontinuity (shock). For transparency and since the limited experimental data in fact does not allow fitting complex functions, here only the simplified model is presented.

6.4.3   Verification

To verify the model predictions of the mask wear, we prepared patterned samples and eroded them using a Schlick industrial powder-blasting machine. The samples consisted of soda-lime glass substrates with a 100-µm layer of LF55G1 or a 50-µm layer of Ordyl. The layers are structured by photolithography to obtain lines with widths of 100, 300 and 500 µm. The samples were then eroded with 23 µm alumina particles at 180 m/s in different doses. After powder blasting the samples were cross-sectioned by breaking them in liquid nitrogen to obtain a clear fracture of the elastomeric masking material.

Figure 6-9a presents a cross-section of the unexposed, 100-μm wide LF55G1 line. The slight trapezoidal shape and the shoulders at the interface with the substrate can be attributed to imperfect development of the structures. Cross-sections of the Ordyl structures show comparable shapes but are little more rectangular.

The exposed profile of LF55G1 (Figure 6-9b) shows a minimum amount of erosion both from the top and from the sloping sides even after a considerable amount of erodent. The top edges show some rounding.
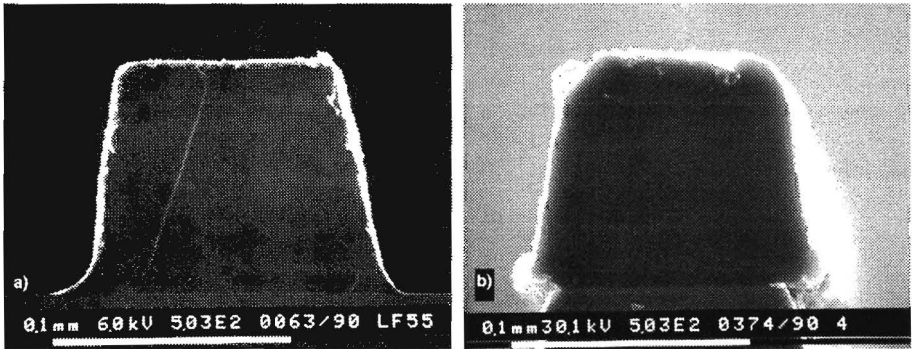
Figure 6-9: The 100 μm line profiles of LF55G1: a) before powder blasting, b) after exposure to 27 g/cm². Remark the narrow edge of glass substrate visible at the bottom of the pictures.
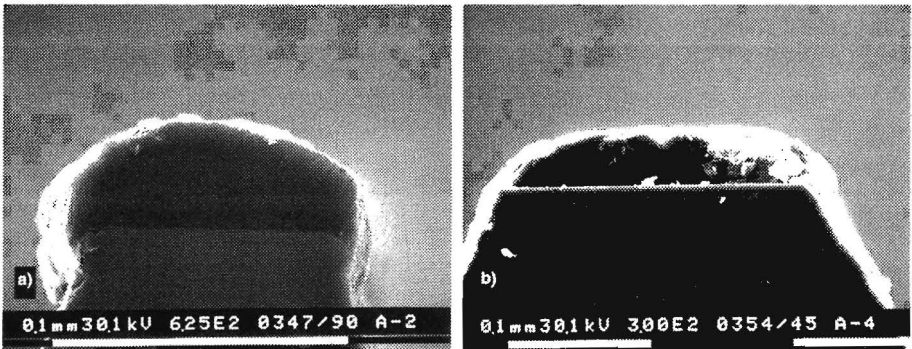
Figure 6-10: Ordyl profiles: a) the 100 μm line after exposure to 7 g/cm², b) the 300 μm line after exposure to 20 g/cm². Note the difference in slope of the eroded profile in the glass substrate.

The Ordyl profiles already display significant rounding of the top edges early in the process (see the 100 μm line after 7 g/cm² in Figure 6-10a). At 20 gr/cm² all 100 μm mask lines had been completely removed. The 300-μm wide line in Figure

6-10b shows that the erosion at normal impact is not responsible for this removal. Of the original thickness of 50 μm still about 30 μm remains. Little over 200 μm is left of the original line width of 300 μm, illustrating that the 100 μm line has been removed by lateral wear of the profiles.

So the phenomena visible in the SEM photographs agree well with the mask erosion model predictions. The images are unfortunately not suitable for a quantitative comparison between model and experiment since artefacts introduced by the breaking of the sample and the presence of abrasive particles on the coating complicate the extraction of the surface geometry from the SEM images.

6.5 Conclusion

The literature review shows that no method is currently available to predict the erosion resistance of polymeric materials on basis of material parameters like modulus or fracture energy. Neither are models available that predict the effect of changing erosion conditions on resistance. Erosion-resistant materials should therefore be tested under conditions closely resembling their intended use.

In this chapter three coating materials selected for their erosion resistance have been characterised for use as powder-blasting masks. The three urethane materials show considerable differences in both erosion resistance and the dependence of erosion on impact angle.

A comparison of the erosion data with thermal mechanical parameters of the materials seems to confirm some of the correlations found in the literature. The erosion resistance is found to be higher at lower glass transition temperatures. The same may hold for the erosion at oblique angles. The materials do not show any correlation between erosion and the loss angle (tan δ).

A model describing the surface evolution reveals a surprising phenomenon. Even for patterns consisting of surfaces parallel and perpendicular to the incident beam, oblique erosion dominates the wear process of fine patterns. Experiments have confirmed the deterioration mechanism caused by oblique erosion. In fine structures the erosion is completely governed by this process. In wider structures the mechanism leads to a very poor detail of the patterns.

Since the increased wear at oblique impact may be a dominating factor even at normal impact, protective materials should be ranked in their order of resistance to erosion at glancing impact angles (for example 15 degrees).

6.6 List of symbols

E The Young's modulus of the substrate [Pa], Equation 6.2.

E_r The erosion rate (mass of removed substrate per mass of erodent used [g/g] or [-]), Equation 6.1.

R The radius of the impacting particle [m], Equation 6.2.

RR The rebound resilience (rebound height/falling height of steel ball falling on a rubber-like substrate) [-], Equation 6.1.

a Fit parameter of velocity dependency of erosion [-], Table 6.2.

b Fit parameter of angle dependency of erosion [-], Equation 6.4.

c Fit parameter of angle dependency of erosion [-], Equation 6.4.

d Fit parameter of angle dependency of erosion [-], Equation 6.4.

f Fit parameter of velocity dependency of erosion [-], Table 6.2.

n A length scale along the local inward normal to the surface [m], Equation 6.5.

q The initial slope $(\partial z/\partial x)$ at a point at the initial mask shape [-], Equation 6.7.

t The time [s], Equation 6.5.

v The impact velocity of the particle [m/s], Equation 6.2.

x A length scale lateral to the incoming particles [m], Figure 6.6.

z The coordinate in de upstream direction of the incoming particles [m], Figure 6.6.

Φ The mass flux of abrasive particles [kg/m^{2}s], Equation 6.5.

β The exponent in erosion models derived from fatigue theory [-], Equation 6.2 and 6.3.

δ The loss angle of the visco-elastic material response [°], Figure 6.3.

ε The curvature of the initial mask shape [m], Figure 6.6.

θ The angle of incidence of the particle [°], Equation 6.2.

ρ The specific mass of the particles [kg/m^3], Equation 6.2.

ρ_t The specific mass of the target material [kg/m^3], Equation 6.5.

6.7 Literature

1   H.J. Ligthart, P.J. Slikkerveer, F.H. in 't Veld, P.H.W. Swinkels, M.H. Zonneveld, *Glass and glass machining in Zeus panels*, Philips J. Res. 50 (1996) 475-499.

2   P.J. Slikkerveer, P.C.P. Bouten, F.H. in 't Veld, H. Scholten, *Erosion and damage by sharp particles*, Wear 217 (1998) 237-250.

3   P.V. Rao, D.H. Buckley, *Spherical microglass particle impingement studies of thermoplastic materials at normal incidence*, ASLE Trans. 27, no 4 (1984) 373-379.

4   A. Brandstädter, K.C. Goretta, J.L. Routbort, D.P. Groppi, K.R. Karasek, *Solid particle erosion of bismaleimide polymers*, Wear 147 (1991) 155-164.

5   J.G.A. Bitter, *A study of erosion phenomena*, Part 2, Wear 6 (1963) 169-190.

6   S.M. Walley, J.E. Field, *The erosion and deformation of polyethylene by solid particle impact*, Phil. Trans. Roy. Soc. Lond. A 321 (1987) 277-303.

7   S.M. Walley, J.E. Field, P. Yennadhiou, *Single solid particle impact erosion damage on polypropylene*, Wear 100 (1984) 263-280.

8   J.C. Arnold, I.M. Hutchings, *The mechanism of erosion of unfilled elastomers by solid particle impact*, Wear 138 (1990) 33-46.

9   K. Friedrich, *Erosive wear of polymer surfaces by steel ball blasting*, J. Mater. Sci. 21 (1986) 3317-3332.

10 Y.I. Oka, M. Matsumura, T. Kawabata, *Relationship between surface hardness and erosion damage caused by solid particle impact*, Wear 162-164 (1993) 688-695.

11 I.M. Hutchings, D.W. Deuchar, A.H. Muhr, *Erosion of unfilled elastomers by solid particle impact*, J. Mater. Sci. 22 (1987) 4071-4076.

12 G.P. Tilly, W. Sage, *The interaction of particle and material behaviour in erosion processes*, Wear 16 (1970) 447-465.

13 G.P. Tilly, *Erosion caused by airborne particles*, Wear 14 (1969) 63-79.

14 C. Arnold, I.M. Hutchings, *Flux rate effects in the erosive wear of elastomers*, J. Mater. Sci. 24 (1989) 833-839.

15 J. Li, I.M. Hutchings, *Resistance of cast polyurethane elastomers to solid particle erosion*, Wear 135 (1990) 293-303.

16 E. Southern, A.G. Thomas, *Studies of rubber abrasion*, Plastics and Rubber: Materials and applications (1978) 133-138.

17 C.M. Thai, K. Tsuda, H. Hojo, *Erosion behaviour of polystyrene*, J. Testing and Eval. (1981) 359-365.

18 P.V. Rao, D.H. Buckley, *Angular particle impingement studies of thermoplastic materials at normal incidence*, ASLE Trans. 29, no 3 (1985) 283-298.

19 D.W. van Krevelen, *Properties of Polymers*, Elsevier (1990).

20 H. Bohm, S. Betz, A. Ball, *The wear resistance of polymers*, Tribology Intern. 23, no 6 (1990) 399-406.

21 H. Uuemois, I. Kleis, *A critical analysis of erosion problems which have been little studied*, Wear 31 (1975) 359-371.

22 R.A. Doyle, A. Ball, *On thermomechanical effects during solid particle erosion*, Wear 151 (1991) 87-95.

23 S.M. Walley, J.E. Field, M. Greengrass, *Impact and erosion study of polyether-etherkethone*, Wear 114 (1987) 59-71.

24 J. Zahavi, G. F. Schmitt, *Solid particle erosion of polymeric coatings*, Wear 71 (1981) 191-210.

25 S.W. Zhang, W. Deguo, Y. Weihua, *Investigation of abrasive erosion of polymers*, J. Mater. Sci. 30 (1995) 4561-4566.

26 B. Lamy, *Effect of brittleness index and sliding speed on the morphology of surface scratching in abrasive or erosive processes*, Tribology Intern. 17, no 1 (1984) 35-38.

27 A.G. Evans, M.E. Gulden, M. Rosenblatt, *Impact damage in brittle materials in the elastic-plastic regime*, Proc. Roy. Soc. Lond. A. 361 (1978) 343-365.

28 M. Vaziri, R.T. Spurr, F.H. Stott, *An investigation of the wear of polymeric materials*, Wear 122 (1988) 329-342.

29 D.C. Evans, J.K. Lancaster, *The wear of polymers*, Treatise on Mater. Sci. and Techn. 13 (1979) 85-139.

30 A. Schallamach, *On the abrasion of Rubber*, Proc. Phys. Soc. Lond. B 67, no 12 (1954) 883-891.

31 J.C. Arnold, I.M. Hutchings, *Erosive wear of rubber by solid particles at normal incidence*, Wear 161 (1993) 213-221.

32 J.C. Arnold, I.M. Hutchings, *A model for the erosive wear of rubber at oblique impact angles*, J. Phys. D: Appl. Phys. 25 (1992) A222-A229.

33 F.H. in 't Veld, P.J. Slikkerveer, *Towards prediction of flux effects in powder blasting nozzles*, Wear 215 (1998) 131-136.

34 P.J. Slikkerveer, F.H. in't Veld, *Model for patterned erosion*, ICEAW conference Cambridge (1998) accepted for Wear.

35 P.J. Slikkerveer, J.H.M. ten Thije Boonkkamp, *Mathematical modeling for erosion by powder blasting*, submitted to Surveys on Mathematics for Industry (1999).

36 R. Courant en D. Hilbert, *Methods of mathematical physics*, Vol. 1, Interscience, NewYork (1953).

37 G. Carter and M. J. Nobes, *The theory of development of surface morphology by sputter erosion processes*, in O. Aucello and R. Kelly (eds), *Ion bombardment modification of surfaces*, Elsevier, Amsterdam, (1984) 163-224.

38 A.J. Walker, M.T. Borchert, C.J. Vriezema, P.C. Zalm, *Influence of surface topography on depth profiles obtained with secondary-ion mass spectroscopy*, Appl. Phys. Lett. 57, no 22 (1990), 2371-2373.

39 I.V.Katardjiev, G. Carter, M.J. Nobes, S. Berg, H.O. Blom, *Three dimensional simulation of surface evolution and erosion*, J. Vac. Sci. Technol. A 12 vol. 1 (1994) 61-68.

7 Particle degradation[*]

For powder blasting large amounts of abrasive powder are used. At a reasonable erosion rate of 0.02 g/g for the removal of one millimetre substrate an amount of powder is required that may form a layer of roughly 50-mm thick. Although abrasive powders are not very expensive, to obtain a cost-efficient mass production process the powders must be reused many times (over 100 times). To enable this reuse degradation (fracture) of the abrasive powder should be minimal.

This chapter studies the degradation behaviour of alumina abrasive powders and tries to find the cause of the type of behaviour the powders exhibit. For this three techniques have been used: degradation experiments to monitor the particle size reduction of the powders, single particle crushing tests to determine the particle breaking forces and X-ray diffraction to study the strains present in the particles.

7.1 Introduction

The fracturing and fragmentation of particles is a well-known phenomenon in solid particle impact. In the industrial powder blasting process patterns are etched in brittle materials like glass to obtain well-defined structures [1]. In this process, hard particles (e.g. alumina or SiC) are used to reduce the amount of powder degradation. Reuse of erodent is essential in these processes for both economic and environmental reasons. Although the particles are considerably harder than the glass, particle-size degradation is still observed.

The amount of particle size degradation is found to be greatest when soft particles hit hard surfaces. In several papers [2, 3, 4], the ratio (H_p/H_t) is used as a parameter where H_p is the hardness of particle and H_t that of the target. At high values, deformation takes place predominantly in the substrate where cracks may form, whereas at low values deformation will occur predominantly in the particle and will eventually lead to particle fracture and degradation.

Extensive particle degradation is however still observed at a hardness ratio of about one, as Sparks and Hutchings [5] have shown for the erosion of glass by silica particles. The powder degradation and fragmentation continue with repeated use of the abrasive.

In case of softer particles, particle degradation is assumed to decrease the erosion rate [6, 7, 8]. Since part of the energy is absorbed in the deformation of the particle, it is not available for inflicting deformation and causing damage to the substrate.

There is some experimental evidence that larger particles are more susceptible to fracture than smaller ones [8]. This may be consistent with a weakest link model, where larger particles, having a larger volume, are the most likely to contain weak spots.

This paper studies the degradation behaviour of alumina particles shot against a "soft" target (boro-silicate glass). In the study, particle degradation measurements obtained after repeated use, the results of crushing experiments of individual abrasive particles and the results of an X-ray diffraction analysis of the lattice strain in the powders are combined. The degradation experiments showed that the particle degradation decreased upon reuse, which is in agreement with the increase in particle strength found in the crushing tests. Using the latest peak deconvolution algorithm, X-ray diffraction reveals the cause of this behaviour. The paper will sequentially address the degradation experiments, the crushing tests and the X-ray diffraction analysis and will end with some conclusions.

7.2 Particle degradation

7.2.1 Experimental procedure

Erosion experiments

Powders of three sizes were used in the erosion experiments, classified according to the FEPA rules (Starck Rhinalox, white fused alumina EW F320, F240 and F150). The mass averaged particle sizes were 29, 44 and 94 μm respectively. These powders were shot at boro-silicate glass samples (Schott AF 45) using a Texas AirSonic HP-1 abrasive jet machine and a mass flux of about 10 grams/min. This machine has a nozzle with an inner diameter of 1.5 mm. In the experimental set-up the nozzle scans across the substrate to distribute the erosion damage evenly across the surface of the substrate. The velocity of the particles was measured before and after each experiment using a double-disk device.

To study the particle fracture behaviour in repeated use, the impact velocity is adapted such that the kinetic energy of an individual particle is about 1 μJ in all experiments and for all powders. This translates for example to impact velocities of original F320, F240 and F150 of 200 m/s, 120 m/s and 35 m/s respectively. The impact energy was kept constant in the experiments since Slikkerveer et al. [9] showed that the erosion process is governed by the impact energy of the particles.

The used powder was collected in the dust-bag of a Nilfisk professional vacuum cleaner, which was in continuous operation to extract air and dust from the experimental enclosure. It was experimentally verified that the collected sample was representative for the size distribution of the powder when the collected amount was larger than 80 grams. In our experiments we used powder batches larger than 200 grams.

In the repeated-use experiments we started with 1 kg of abrasive powder. After each time of use, a sample of 200 grams was set apart, while the rest of the powder was re-used. Since the powder was not separated from the chips removed from the target, the fraction of glass chips increases with reuse from 3% after the first use to about 15% after five times use. Since this considerable amount of glass chips generated powder agglomerates that clogged the abrasive jet machine, the powder could not be reused more than five times (F320: four times).

Particle size measurements

The particle sizes of the original and reused powder were measured using a sedimentation technique (Sedigraph 5100). The liquid used in this instrument consisted of ethylene glycol (90%), water (10%) and 0.2 g/l $Na_4P_2O_7$ to prevent agglomeration. Since all powders contain a comparable distribution of particle

sizes, the size distribution is described in this section by the mass-averaged particle size.

Before each measurement, the glass chips were removed from the reused samples with an etching procedure using HF (10% weight in water) for five minutes followed by HNO_3 (3% weight in water) for two minutes. The effect of this etching procedure is shown in Figure 7-1 for F320. The glass chips are visible in the used powders as an elongated particle size distribution below 10 µm.

The HF etching removes the majority of these particles but resulted in a small amount of particles of about 1 µm. These particles arise from the barium present in the AF45 glass which is not dissolvable in the HF etch and are removed in a short HNO_3 etching step. By etching and measuring non-used powders it was verified that the etching procedure had no significant effect on the particle size distribution of the Al_2O_3 particles.
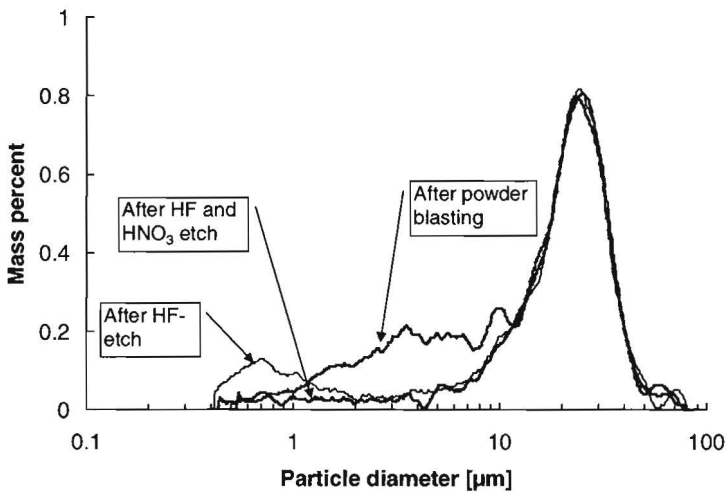
Figure 7-1: The removal of glass chips from collected F320 powder by the etching process.

7.2.2   Results and discussion

The first set of experiments investigated the effect of particle velocity on degradation in single use. The particle size reduction was found to increase with increasing impact velocity, as expected. The data in Figure 7-2 permits the suggestion of a threshold in the velocity consistent with the findings of Tilly and Sage [10]. The threshold velocity seems to be lower for the larger particle size.
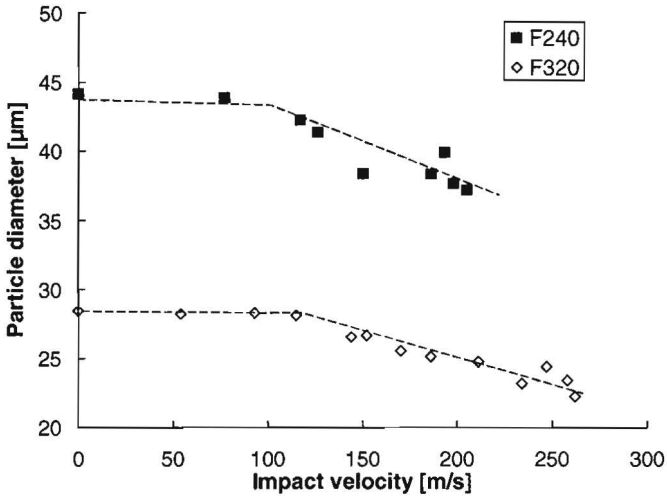
Figure 7-2: The degradation of particle size in single use as a function of impact velocity.

The results of the re-use experiments at constant impact energy ($\pm$ 1 μJ) are presented in Figure 7-3. The shapes of the curves show that the observed effect is a "start-up" effect, i.e. the degradation decreases with the number of times re-use. The powders with the smaller particles show roughly the same reduction in particle size of 25%, whereas the F150 powder displays a size reduction of just over 10% only.

Since the relative width of the particle size distributions of the used and unused powders are comparable, there are no signs of large-scale particle fragmentation. The decrease of 25% in particle size observed for the smaller particles can thus be interpreted as the particles splitting into two equal parts (a factor 0.5 in particle weight corresponds to a factor 0.79 in particle diameter).

Interestingly, the degradation rate of the used powder is less than that of the original powder with particles of about the same size. The particles of the 4-times reused F240 ($\pm$ 33 μm) reduce 0.7 μm in size on the fifth impact, whereas the original F320 powder ($\pm$ 29 μm) degrades about 4 μm on the first impact. The reused powders thus seem to be more resistant to fracturing and fragmentation than the original ones.

This difference in degradation behaviour suggests that reused powders are stronger than unused powders. This hypothesis will be discussed in the next section, which presents the results of the single-particle crushing tests of the considered powders.
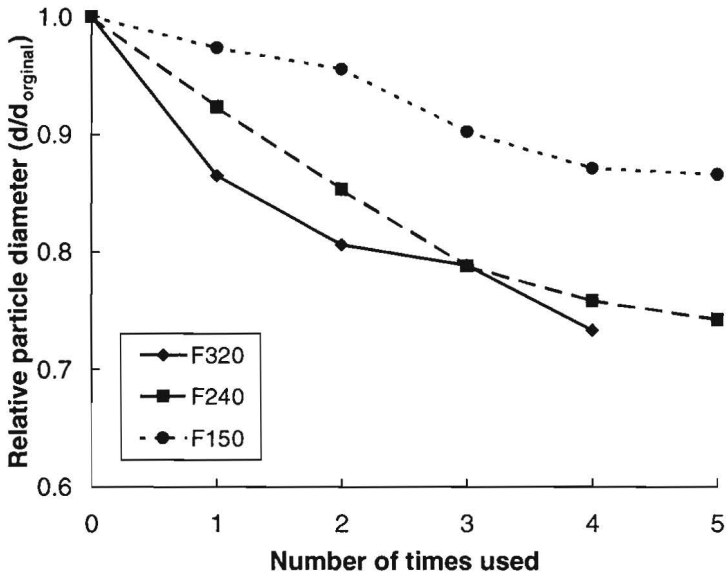
Figure 7-3: The particle size degradation in multiple reuse of the three powders.

7.3 Particle strength

7.3.1 Experimental procedure

The strength of the powders was determined using the single particle crusher developed at the Eindhoven University of Technology [11, 12]. In this crusher abrasive particles of sizes between 10 and 500 μm can be crushed individually between two diamond anvils. During an experiment the anvils move towards one another at a well-defined velocity, while the force to do so is measured. Since the anvils are transparent, a view of the particle can be recorded on videotape during the experiment using a stereomicroscope placed on top of the crusher.

The design of the crusher is based on an electromechanical principle (a voice coil) similar to the principle used by Rumpf and Schönert [13]. The current in the coil is a measure of the crusher force. The relative displacement between the lower and upper anvils is determined independently from the force using three inductive high-speed displacement transducers positioned around the measuring area. A control loop adapts the crushing force to obtain the required crushing speed.

During a test the force increases gradually. A sudden, considerable decrease in the force is interpreted as the breaking of the particle. This can be verified by examining the video recordings of the experiment.

To determine a breaking force distribution of the particles in each of the powders, about 100 individual particles were crushed. The tested samples contained; the three unused powders, the three powders after single use and the F240 and F150 powder after five times of use. Separating single particles from the four times reused F320 powder was found to be unworkable, so the strength of this powder could not be measured. The fracture forces of the particles within one sample were processed using Weibull statistics [14], which resulted in a mean fracture force and the Weibull modulus describing the width of their distribution. The particle strength distribution can be described reasonably well with the Weibull statistics [12].

7.3.2   Results and discussion

The results of the crushing experiments showed a Weibull modulus of about 1 for both the original and the used powders (see Table 7-1), indicating a large variation in strength. Low Weibull modulus values were also found for abrasives by Huang et al. [15] (2.5 for white corundum), Bertrand et al. [16] (approximately 1.5 for fused alumina) and Brecker [17] (3.5 for white alumina).

A slight increase in the Weibull modulus was observed for the alumina powders after erosion, which may have been caused by the failure of the "weaker" abrasive particles during the erosion process.

Table 7-1: The Weibull data of the tested samples.

Abrasive Powder	Particle diameter d [μm]	Mean fracture force F_{mean}[N]	Weibull modulus [-]	Number of particles tested
F320				
Original	28.8	0.27	1.09	88
Used 1x	24.9	0.29	1.04	98
F240				
Original	44.2	0.36	1.04	88
Used 1x	40.8	0.51	1.08	90
Used 5x	32.8	0.47	1.19	90
F150				
Original	93.8	0.74	0.85	80
Used 1x	91.3	0.91	1.04	93
Used 5x	81.2	0.95	1.09	87

In the case of brittle materials, failure is usually connected with the distribution of flaws in the specimens. The largest flaw present in the tested area of the substrate

surface will limit the strength of the sample. The surface of small particles is too small to contain a full distribution of flaws. The strength of these particles is coupled with the presence of a flaw in the particle and the size of this flaw. Flaws are probably micro-cracks and pores created during the manufacturing process prior to the testing [15]. Since a particle may contain a single flaw, or no flaw whatsoever, a wide distribution in fracture strength is to be expected.

The mean fracture forces of the seven tested powders are shown in Figure 7-4 as a function of the mean particle size. The figure shows a roughly linear increase in the mean fracture force with particle size. When the strength of the particles is correlated with the breaking stress ($\propto F_{mean}/d^2$), the particle strength is found to increase with decreasing size in accordance with the findings of Routbort and Scattergood [8]. Very small particles will be even impossible to break since the amount of elastic energy that the particle can store is too small to generate fracture, according to [18]. For alumina this particle size (predicted 3.3 µm, [19]) is still considerably smaller than the size of the particles investigated here.
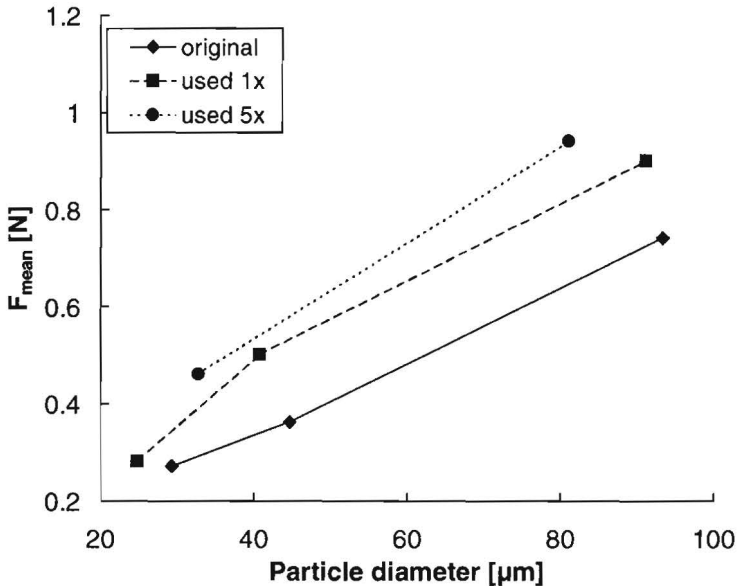

Figure 7-4: The mean fracture forces of all the measured samples plotted as a function of their particle sizes.

The original and reused samples differ in both particle size and breaking force, which makes comparison of the breaking forces difficult (see Table 7-1). The lines

connecting the data of the original and the reused powders in Figure 7-4 show a systematic shift, suggesting that the powders become stronger in reuse. Considering the wide distribution in the fracture forces and particle sizes of the particles within one sample, the significance of the suggestion above needs to be tested.

To do this first the size of each crushed particle was determined from its projected area in the video image. Now each tested particle can be characterised by its particle size and its breaking force and could be individually plotted in Figure 7-4. Since the large scatter in values would hinder interpretation, two statistical methods were used to investigate whether the original and the used powders differed significantly in strength.

The Kruskal-Wallis test [20] was used to determine whether the particles of the different powders derive from the same strength/size distribution and whether the original samples differed from the used ones. No assumption needs to be made on the distribution function of the size or strength distribution. The employed method simply examines whether or not two sets of data derive from the same distribution. The results of the Kruskal-Wallis test show that the three original powders differed only marginally and may originate from the same population. The 5 times reused F240 sample differed significantly from this distribution in its greater strength. The 5 times reused and the original F150 samples did not show a significant difference in strength.

No statistical distribution function is required for the second method either. The bootstrap method [21, 22, 23] starts with a set of N data points, in our case each data point representing a particle with its size and fracture force. From this set new data sets are created by randomly selecting N points from the original data set, where each data point may be selected multiple times. Typical numbers of the bootstrap samples range from 50 to 200 for standard error estimates.

The mean particle size and fracture force can be calculated for each bootstrap sample. Figure 7-5 illustrates the average values obtained for some of the bootstrap samples. The figure clearly shows a significant difference between the distributions of the original F320 and F240 powders and those of the five times used F240 powder. The F150 samples show no significant difference.

The strength results for the F240 powder thus supports the hypothesis that the difference in powder degradation between the original and the reused powders derives from an increased strength of the reused abrasive grains. The cause of this increase in strength will be studied in the next section using an X-ray diffraction analysis.
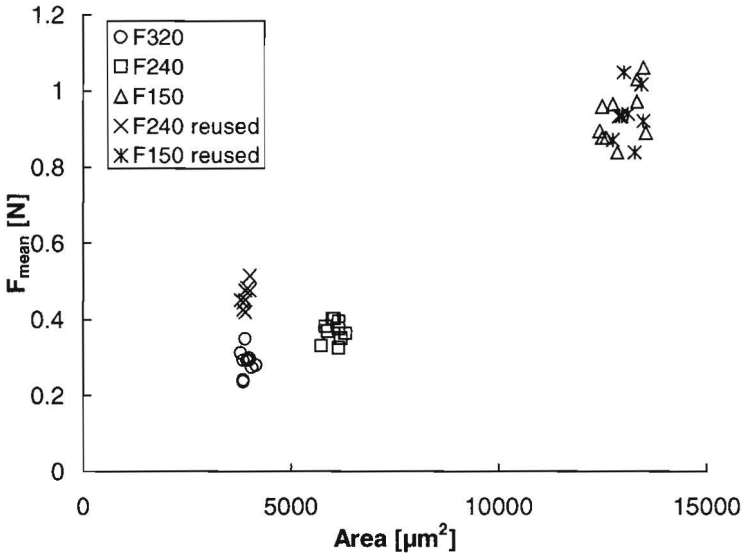
Figure 7-5: Some of the bootstrap results obtained for the strength of the original and the 5 times used powders.

7.4 Lattice strain in particles

X-ray diffraction is a generally used technique for the micro-structural analysis of crystalline media. Since the alumina abrasive powders are micro-crystalline, the technique can be used to study the micro-strain in the particles, which is visible as line broadening of the diffraction peaks [24]. The amorphous glass chips present in the reused powder do not influence the measurement and no not need to be removed.

7.4.1 Experimental procedure

The diffraction patterns of the original and the multiple times re-used F320 and F240 powders were measured using a Philips X'Pert diffractometer system. The F150 powder was not measured since its large particles will generate too much noise in the counting statistics. The instrument is equipped with a 1/2° divergence slit and a 0.1 mm receiving slit and used Cu radiation. The sample rotated around its normal during the measurements and the step size (2θ) in continuous mode typically amounts to 0.005°. A standard Philips graphite secondary monochromator was used in all the experiments. With the aid of the novel profile analysis technique [25] the contribution of for example lattice strains to the reflection peak profiles can be separated from that of the measurement set-up. The low percentage

of noise generated in this deconvolution technique relative to that generated in the standard Fourier deconvolution technique enables the in-depth investigation described in this section, e.g. the lowest line width which can accurately be determined corresponds to a particle size effect of 1 μm particles.

To limit the influence of statistical noise on the deconvolution procedure the counting time was increased until the effect of the counting statistics error on the peak maxima was less than 1%. To enable a good comparison, all samples were prepared with approximately the same filling factor ($\approx$ 65 %).

7.4.2   Results and discussion

Since the hexagonal Al_2O_3 lattice contains an isotropic base plane for X-ray diffraction spanned by the [100] and the [010] direction, the lattice can be characterised by two directions only: the [001] direction and any [hk0] direction.

To enable interpretation of the diffraction results it is necessary to analyse peaks of a few orders of reflection in the same direction. Sufficient [hh0] peaks with adequate intensity are available for this analysis in the base plane. In the [001] direction only one peak [006] is strong enough to allow the use of the profile analysis technique. Therefore as an alternative, the [0k2k] peaks are used [012], [024], [048], whose directions are almost perpendicular to the [hh0] direction.

The deconvoluted peak profiles in the [hh0] direction ([110], [220], [440]) show a single narrow peak. No difference in the peak width is observable between the original and the used powder.

The peaks in the [0k2k] direction show a different characteristic. They seem to consist of a superposition of a high narrow peak and a low broad peak (see Figure 7-6). A comparison of the original and the reused powders reveals a reduction in the height of the broad peak relative to that of the narrow peak on reuse. To quantify the width and amplitude ratio of the peak contributions we fitted the overall profile with a function consisting of a sum of two gauss functions: one yielding a narrow contribution and one a broad peak.

$$I = \sum_{i=n,b} \frac{a_i}{\sqrt{2\pi}\sigma_i} e^{\frac{-(\theta-\theta_0)^2}{2\sigma_i^2}} \tag{7.1}$$

Here a_i and σ_i are fit parameters describing the amplitude of the contribution and the width of the peak contribution, respectively. The parameter θ_0 gives the central peak position. The index $i = n, b$ stands for the narrow and the broad contributions.

In the following discussion we will replace σ, the standard deviation of the gaussian distribution, with β - the peak width at half height - as is commonly used in X-ray diffractometry. Simple calculus shows that $\beta = 2.35\sigma$ for a gauss function.
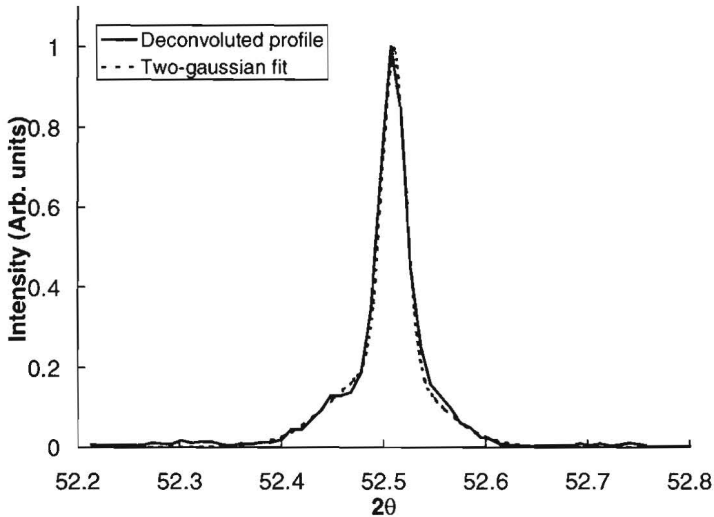
Figure 7-6: The sample contribution of the [024] peak of the original F320 powder. The dashed line represents the fit with equation 1.

To understand the meaning of the broad and narrow peak contributions, we made Williamson-Hall plots for the three peaks in the same direction [24] by plotting the width of the peak ($\beta \cos(\theta)$) as a function a sine of the reflection angle (the order of the reflection). Interestingly, the plots in Figure 7-7 show different behaviour for the narrow and the broad peak contributions for both powders. The width of the narrow peak contribution does not depend on the reflection angle, whereas the broad peak contribution displays a clear dependency on the angle.

An independence of the reflection angle is usually connected with a crystallite size effect. A calculation of the average crystallite size using the Scherrer equation [24] yields a size of about 0.25 μm. However, using scanning electron microscopy at a resolution below 4 nm at 1 kV (FEI-Philips XL30 SFEG) in combination with electron back scatter patterns (EBSP), it was found that the particles are single crystals. The explanation of the Scherrer equation as a crystallite size is apparently not appropriate here. In a second interpretation [26], such effects are very localised areas of strain, which may have arisen as a result of impurities or other point defects.
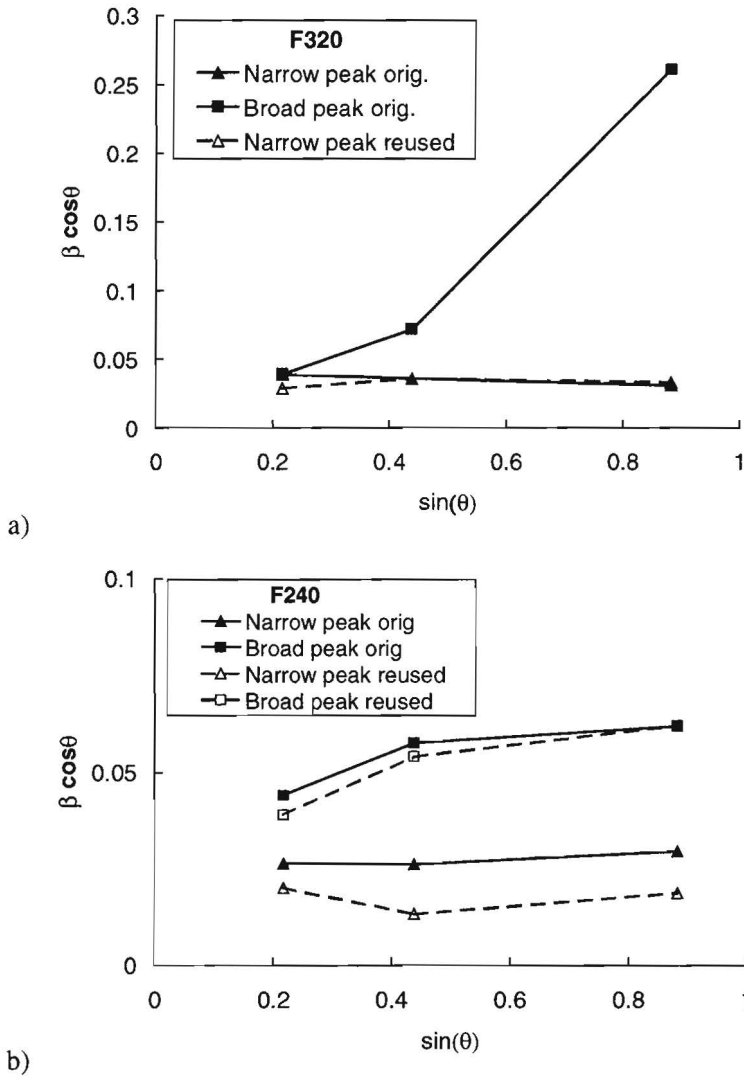
Figure 7-7: Williamson-Hall plots obtained for the [0k2k] direction of the F320 (a) and F240 powder (b). The solid lines represent the original powder, the broken lines the used powders (F320 used four times, F240 used five times).

The increase in the width with the reflection angle of the broad peak contribution is a classical example of strain broadening measured in the [0k2k] direction. This strain is apparently present in the [001] direction, because the [hh0] peaks do not display any sign of strain effects. Interestingly, the broad peak contribution in the original and the used F240 powders shows the same slope, which suggests that the

type of strain and its spatial distribution are the same. The broad peak contribution in the reused F320 may have shown the same phenomenon, but its amplitude was too low for detection in the fitting procedure. The original F320 apparently contained a considerably higher strain than F240, as the difference in the slope of the broad contribution shows. The lattice strain of F320 is very high (a RMS lattice distortion of $\Delta d/d$=0.003), as Reefman [25] calculated on the basis of the slope of the Williamson-Hall plot.
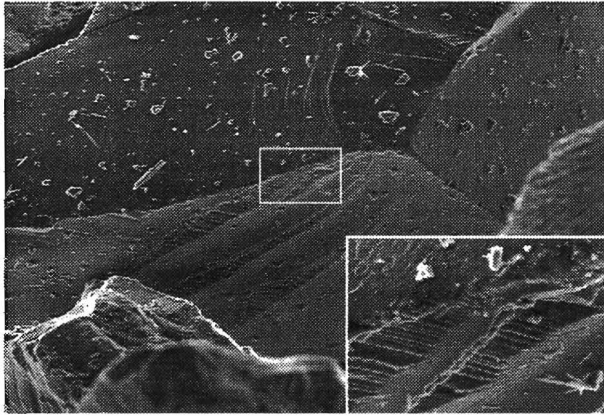
Figure 7-8: High-resolution SEM photograph of part of an original F320 grain. The width of the picture is 20 μm. The insert shows an enlargement of the section in the box.

As the width of the broad peak contribution correlates with the height of the localised strain, its amplitude (a_b) corresponds to the total amount of strained material present in the powder. The amplitude can also be interpreted as a measure of the number of strain sites in the powder, since the Williamson-Hall plot of F240 shows that the character of the strain fields remains unchanged in reuse. The relative reduction in the broad peak contribution to the peaks observed can be quantified in the ratio a_b/a_n. For the original powders this ratio was 1:5 for F240 and 1:6 for F320. With the five times reused F240 the ratio increased to about 1:15, which is about the detection limit of the fitting technique. The broad peak contribution observed for the reused F320 is apparently below this limit, because it could not be identified.

7.5 Discussion and conclusion

Degradation experiments have shown that particle degradation decreases with the number of times a powder is used in the powder-blasting process of glass. The

original powders exhibited a considerably higher degree of particle degradation than the reused powders having particles of comparable size.

Single-particle crushing tests indicated that used particles combine a decrease in size with an increased breaking force. The five times reused F240 powder showed to be considerably stronger than the original F240 and F320 powders. For different reasons this behaviour could not be confirmed for the F320 and the F150 powders. The measuring procedure could not handle the four times reused F320 particles, while the difference between the original and used F150 is found to be statistically not significant. This lack of significance might originate in the only limited amount of particle size degradation in the F150 particles (only 12 %) compared with the 25% of the other powders. Although the increase in particle breaking force could not be proven for the F320 and F150 powders, a comparable behaviour of the F240 powder can be expected.

Since impacting particles experience on impact a certain maximum force depending on the impact energy and particle shape, it is evident that the increased breaking force measured will lead to the decreased degradation observed in reused powders.

Generally the strength of brittle materials is governed by the distribution of flaws (often micro-cracks) in the material. The strength tests thus suggest that the used powders contain a lower concentration of flaws and/or smaller flaws than the original powder.

X-ray diffraction showed that the original powders contained large amounts of strain. The solid particle impact reduced the strain considerably. Although the measured strains point to the existence of dislocations storing a considerable amount of elastic energy, they do not necessarily correlate with flaws of a larger scale. If the dislocations are concentrated in part of the geometry they will effectively act as flaws that will limit the material strength. The other way round, material flaws or micro-cracks will generate the strain fields observed.

The strong reduction in strain after reuse suggests that the lattice strains be indeed localised. A dislocation generating the lattice strain can only be removed when it is moved to the surface of the particle enabling the release of the elastic energy stored. The most likely way to do this is to generate new surface, i.e. by fracturing the particle. Since a large amount of strain is taken away by generating only a limited amount of new surface area - the particle does not fragment -, it is probable that the dislocations are concentrated in parts of the particles.

The strain sites of the F240 powder not changing character at use supports this picture. The degradation of the powder is seen to reduce the amount of strain but not affecting the character of the remaining sites. Particle fracture apparently

removes a large part of the strain sites, the ones positioned at the newly found surface area, and unchanging the other ones.

Hence it is very likely that flaws in the original powder dominate the degradation behaviour of the alumina powder investigated. During the solid particle impact, some of the particles break at these flaws as a result of which the flaw is removed and the strength of the powder consequently increases. Interestingly, the impact of the particle on the glass substrates does not seem to generate a significant amount of new damage. The impact process must apparently be classified as "soft", relative to the crushing process that is used to produce the abrasive powders.

Acknowledgement

7.6   List of symbols

F_{mean}	Weibull mean fracture force [N], Table 7.1.
H_p	The indentation hardness of an impacting particle [Pa], Section 7.1.
H_t	The indentation hardness of the target material [Pa], Section 7.1.
I	Intensity of the X-ray backscattering beam [Arb. units], Equation 7.1.
a_i	Amplitude of the Gauss function fitting the broad peak contribution ($i = b$) or the narrow peak contribution ($i = n$), Equation 7.1.
d	Diameter of a used particle [m], Figure 7.3.
$d_{original}$	Diameter of an unused particle [m], Figure 7.3.
β	The width of a X-ray backscatter peak at half height [°], $\beta_i = 2.35\sigma_i$ for a Gaussian peak shape, below Equation 7.1.
θ	The X-ray backscatter angle [°], Equation 7.1.
θ_0	The central angle of an X-ray backscatter peak [°], Equation 7.1.
σ_i	Width of the Gauss function fitting the broad peak contribution ($i = b$) or the narrow peak contribution ($i = n$) [°], Equation 7.1.

7.7 Literature

1   H.J. Ligthart, P.J. Slikkerveer, F.H. in 't Veld, P.H.W. Swinkels and M.H. Zonneveld, *Glass and glass machining in Zeus panels*, Philips J. Res. 50 (1996) 475-499.

2   S.M. Wiederhorn, B.J. Hockey, *Effect of material parameters on the erosive resistance of brittle materials*, J. Mater. Sci. 18 (1983) 766-780.

3   L. Murugesh, S. Srinivasan, R.O. Scattergood, *Models and material properties for erosion of ceramics*, J. Mater. Eng. 13 (1991) 55-61.

4   P.H. Shipway, I.M. Hutchings, *The role of particle properties in the erosion of brittle materials*, Wear 193 (1996) 105-113.

5   A.J. Sparks, I.M. Hutchings, *Effects of erodent recycling in solid particle erosion testing*, Wear 162 (1993) 139-147.

6   I.M. Hutchings, *Transitions, threshold effects and erosion maps*, Key Eng. Mat. 71 (1992) 75-92.

7   L. Murugesh, R.O. Scattergood, *Effect of erodent properties on the erosion of alumina*, J. Mater. Sci. 26 (991) 5456-5466.

8   J.L. Routbort, R.O. Scattergood, *Solid erosion of ceramics and ceramic composites*, Key Eng. Mat. 71 (1992) 23-50.

9   P.J. Slikkerveer, P.C.P. Bouten, F.H. in 't Veld, H. Scholten, *Erosion and damage by sharp particles*, Wear 217 (1998) 237-250.

10   G.P. Tilly, W. Sage, *The interaction of particle and material behaviour in erosion processes*, Wear 16 (1970) 447-465.

11   M.A. Verspui, G. de With, E.C.A. Dekkers, *A crusher for single particle testing*, Rev. Sci. Instrum. 68, no 3 (1997) 1553-1556.

12   M.A. Geltink-Verspui, *Modeling abrasive processes of glass*, PhD. Thesis, Eindhoven University of Technology (1998).

13   K. Schönert, H. Rumpf, *Versuche zur zerkleinerung von einzelteilchen zwischen zwei flächen, Symposion Zerkleinern*, Frankfurt am Main, edited H. Rumpf (1962) 108-127.

14   W. Weibull, *A survey of statistical effects in the field of material behaviour*, Appl. Mech. Rev. 5, no 11 (1952) 449-451.

15   H. Huang, X.H.Zhu, Q.K. Huang, X.Z. Zu, *Weibull strength distributions and fracture characteristics of abrasive materials*, Eng. Fract. Mech. 52, no 1 (1995) 15-24.

16   P.T. Bertrand, S.E. Laurich-McIntyre, R.C. Bradt, *Strengths of fused and tabular alumina refractory grains*, J. Am. Ceram. Soc. 67, no (1988) 1217-1222.

17   J.N. Brecker, *The fracture behaviour of abrasive grains*, J. Eng. Ind; Trans. ASME, 96 (1974) 1253-1257.

18 L. Sikong, H. Hashimoto, S. Yashima, *Breakage behaviour of fine particles of brittle materials and coals*, Powder Techn. 61 (1990) 51-57.

19 J.T. Hagan, *Impossibility of fragmentation small particles: brittle ductile transition*, J. Mater. Sci. Letters, 16 (1981) 2909-2911.

20 W.J. Conover, *Practical nonparametric statistics*, 2nd edition (1980) John Wiley & Sons Inc. 229-237.

21 P. Diaconis, B. Efron, *Computer intensive methods in statistics*, Scientific American, 248 (1983) 96-108.

22 B. Efron, *Computers and the theory of statistics: thinking the unthinkable*, SIAM review 21 (1979) 460-480.

23 B. Efron, R.J. Tibshirani, *An introduction to the bootstrap,* 1st edition, Chapman & Hall Inc. (1993).

24 H.P. Klug and L.E. Alexander, *X-ray diffraction procedures*, 2nd edition, J. Wiley, New York (1974).

25 D. Reefman, *Detailed study of strains in Al_2O_3 powder by a novel profile analysis technique*, Proc. Size and Strain, Materials Structure 3, no 3 (1996) 195-200.

26 J. van Berkum, *Strain fields in crystalline materials*, PhD. Thesis, Delft University of Technology (1994).

8 Upscaling: The flux effect[*]

For an industrial production of displays, large areas need to be patterned by powder blasting (over 10^6 m²/year). To achieve this at reasonable process times, machines are needed that operate with high powder feed rates, which can be obtained by using a considerable number of larger-size nozzles in parallel.

However, increasing the powder flux and nozzle size reduces the efficiency of the erosion process. Particles rebounding from the surface interact with incoming particles before being removed from the jet. Collisions with rebounding grains decrease the energy of impacting particles, reducing their efficiency. Anand et al. derived a single-parameter fit model for this so-called "flux effect". Although this fit parameter was assumed to be constant, experiments have yielded a wide range of values for it, making the model unsuitable for flux-effect predictions.

This chapter correlates - for glass eroded by alumina particles - the fit parameter to the impact velocity of the particles for nozzles from 1.5 to 12 mm in size. Within this range the correlation can be used for interpolation between process conditions and nozzle sizes and to develop and optimise a large scale industrial process. This result may be seen as a first step to a universal model for prediction of flux effects for all type of erosion processes.

8.1 Introduction

The rate of material removal is an important parameter for abrasive processes. In erosive wear it characterises the lifetime of the substrate, whereas in industrial powder-blasting processes (see e.g. [1]) it dictates the process time. In case of solid-particle erosion the process rate is usually expressed in the erosion rate - the ratio between the weight of the removed material and the weight of the used powder.

Several papers have shown that the erosion rate is a function of particle flux [2, 3, 4, 5, 6]. The higher the particle flux, the lower is the measured erosion rate. Decreases in erosion rate with particle flux of 30% [4] and even 90% [7] have been reported.

Although the particle flux has a major influence on the erosion rate, models of the erosion processes [e.g. 8, 9, 10] do not include this effect. These models describe erosion as caused by the processes that occur when a particle hits a surface. In the basic erosion mechanisms no effects of particle flux on the erosion rate are expected.

The so-called "flux effect" originates in the processes in the particle jet before the particle hits the surface. Several authors [2, 4, 7, 11] suggested that rebounding particles effectively shield the substrate from incoming particles. The incoming particles hit rebounding particles and loose part of their energy. Andrew and Horsfield [11] and Shipway and Hutchings [5] have presented photographic evidence of particle collisions in the jet confirming this hypothesis.

Andrews and Horsfield [11] have presented a stochastic model for calculating the frequency of collisions and particle motion as a function of particle flux. They validated their model using high-speed photography. They concluded that particle collisions do not reduce the number of impacts on the target but reduce the impact velocity and giving both the velocity and impact angle a wider variance.

Though the model of Andrew and Horsfield is probably the most advanced model for particle interaction in jets, it contains no link to erosion rate.

Anand et al. [7] derived a mechanistic model for the flux effect resulting in an exponential dependence of erosion rate on particle flux. Their experiments validate the exponential dependence. The model contains only one fit parameter that, considering the derivation, was thought to be a constant. The experiments of Anand et al. showed that the parameter is not constant, but varied up to a factor of 3 between the experimental conditions.

For estimating efficiency and process time in industrial application of the powder-blast process it is advantageous to be able to predict the flux effect. It is also interesting in erosion testing. Since the flux effect is unknown, it is currently

advisable to perform these tests at very low fluxes, at which the flux effect is negligible [5]. For erosion-resistant materials this is a time-consuming process.

In this paper we show that the flux effect model of Anand et al. can be used for interpolation between different nozzle sizes with the same erosion process by replacing the "constant" with a simple two-parameter fit. This may be a first step towards a prediction of the flux effect in all cases.

We will first review the model of Anand et al. After describing the experimental methods, we will search for correlation's between Anand's fit parameter and process parameters. Finally, we will discuss the possible physical meaning of this extended fit and draw some conclusions.

8.2 The flux effect model of Anand et al.

Anand et al. rationalised the flux effect in terms of a first-order particle collision model. They calculated the probability of an incoming particle hitting a rebounding particle. The incoming particle was assumed to contribute nothing to the erosion process.

The model is based on several assumptions. Anand et al. considered a normal incident beam of particles with a homogeneous distribution of particles. The particles in the beam were assumed to rebound normally and move over a length L in the incidenting beam before being removed from the beam.

The probability (P) of an incoming particle not hitting a rebounding particle is

$$P = \exp(-ALC) \tag{8.1}$$

where A ($= \pi D^2$ with D being the diameter of the particle) is the collision cross-section of the particle, L the rebound height and C the concentration of the rebounding particles.
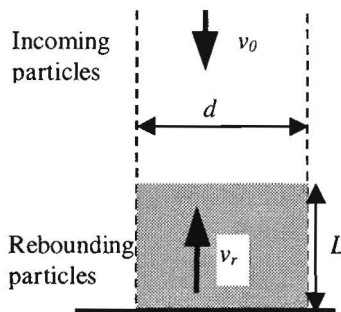

Figure 8-1: The principle of the flux effect model of Anand et al.

Translating this model to practical parameters of the erosion process Anand et al. arrive at

$$E_f = E_r \exp\left(\frac{-24\,\tau\,J}{\pi\,\rho\,D\,d\,v_0}\right) \tag{8.2}$$

where

E_f	=	the actual erosion rate [kg/kg].
E_r	=	the erosion rate at zero flux (no flux effect) [kg/kg].
d	=	spot size or diameter of the particle beam [m].
τ	=	fit coefficient [-].
ρ	=	density of the particles [kg/m^3].
D	=	diameter of the particles [m].
v_0	=	impact velocity of the particles [m/s].
J	=	incoming particle flux [kg/s].

The coefficient τ contains a number of unknowns but can be seen as a dimensionless rebound height

$$\tau = \frac{L}{d}\frac{1}{\alpha} \tag{8.3}$$

where α is the rebound coefficient defined as the ratio of rebound velocity (v_r) and impact velocity (v_0). On the basis of an order of magnitude approach, Anand et al. estimated τ to be between 5 and 10 for physically realistic conditions. They actually found the values of τ fitted to experimental data to vary from 4.5 to 11.5. This range of values makes the model hard to use in practical circumstances. In this paper we will discuss a first step towards an improved model.

8.3 The experiments

In order to study the flux effect, series of experiments were performed with three nozzle sizes (1.5 to 12 mm), different particle velocities (100-270 m/s) and distances between the nozzle and the substrate ("nozzle heights"). In each experimental series we varied the mass flux over a wide range to determine the size of the flux effect.

In the 1.5-mm nozzle experiments we used a pressure feed abrasive jet machine (Texas Airsonic HP-1). In the 6- and 12-mm nozzle experiments an industrial sandblast machine supplied by Schlick was used. The 1.5-mm nozzle consisted of a 16-mm-long cylindrical alumina tube placed at the end of a polyurethane tube transporting the air-powder mixture. The two larger nozzles were commercially available sandblast nozzles. The 6-mm nozzle was a 6-mm nozzle of Laval type with an exit diameter of 8 mm and a length of 115 mm. It was operated in combination with a 4.5-mm air nozzle. The 12-mm nozzle was a cylindrical nozzle

with a length of 115 mm, which was operated in combination with a 9-mm air nozzle. All the nozzles had circular openings. In all experiments the nozzle performed a scanning motion relative to the sample, to prevent crater formation.

Table 8-1: The measurement series.

Series no	Nozzle diameter (d_0) [mm]	Sample-nozzle distance (h) [mm]	Particle velocity (v_0) [m/s]	Particle diameter (D) [μm]
1	1.5	40	127	29
2			181	
3			200	
4	6	50	227	23.5
5		75	200	
6		100	177	
7			221	
8	12	85	260	23.5
9			271	29
10		170	230	

Since all jets were found to be divergent, the nozzle height was varied to obtain independent means for changing the spot size on the target.

The particle velocity was measured using a one-dimensional Laser Doppler Anemometer (LDA) system (Dantec BSA & Flowlite, Skovlunde, Denmark). Since the LDA system was equipped with frequency shifting, positive and negative velocities could be distinguished. The measured particle velocities showed a distribution with a variation in the order of 20 m/s. We used the mean velocity, which we were able to measure reproducibly to within 3 m/s.

In the rebound experiments we measured the horizontal and vertical velocities of the particles scanning along a line through the centre of the jet 16-mm above the target. These velocities we used to calculate the mean velocity and the directions of the incoming and rebounding particles.

Angular alumina particles (Starck Edelkorund F320 - 29 μm mean particle size) were used in all our experiments. Some experiments were performed using an industrial sandblast machine in which the abrasive was recycled. The particle size of this recycled alumina powder was 23 μm. The particle sizes were determined with sedimentometry (Sedigraph 5100).

Two different types of glass were used as target materials (Schott AF45 borosilicate and Glaverbel soda-lime float glass). These glasses differ only marginally in erosion rate [9]. The absolute value of the erosion did not influence our measurements because we studied only the relative decrease in this erosion rate with increasing flux.

The erosion rate was calculated by dividing the mass loss of the target by the total mass of the used powder. Most experiments were performed in duplicate; the reproducibility of these experiments was found to be within 2 % of the average value.

The amount of abrasive powder used was calculated from the powder flux and the time that the jet acted on the sample. The powder flux in the industrial machine was measured by collecting the powder for a defined time before and after each experiment. The powder flux of the small abrasive jet machine (HP-1) was found by placing the complete machine on a balance and measuring its weight loss with time.

Table 8-1 shows an overview of the experimental series performed. Each series in this table consists of a set of erosion rate experiments varying the powder fluxes at least a factor of 10.

8.4 Data processing

For each of the ten measurement series mentioned above, the fit parameter τ of the model of Anand et al. is obtained using a least-squares method. Prior to this we calculate the spot size of the jet (d) and correct for influences of velocity changes with variations in particle flux.

8.4.1 The spot size

Since the abrasive jets are divergent, the diameter of the particle beam (spot size) is larger than the nozzle diameter. To determine the spot size, we used the general correlation found by van Zandvoort et al. [12] for the nozzles considered in this paper. They measured the erosion profile of a fixed nozzle in a soda-lime glass substrate. After fitting this profile with a gaussian curve, they defined the spot size at three times the standard deviation (σ) of this gaussian fit. Correlating the spot size (d) with nozzle height (h) gave the general correlation

$$d = d_0 + 2 h \tan (\phi) \tag{8.4}$$

with d_0 the exit size of the nozzle and ϕ the divergence angle of the jet fitted to 5°. Figure 8-2 shows the comparison between the correlation and the measurements for the 6-mm nozzle.

Note that fully developed turbulent air-jets have a constant divergence [13]. The divergence angle depends on the choice of the jet's boundary, but is comparable (4°) with the one obtained by van Zantvoort et al.

The conclusions in this paper are found to be insensitive to the exact value of ϕ. We used relation 8.4 with $\phi = 5°$.
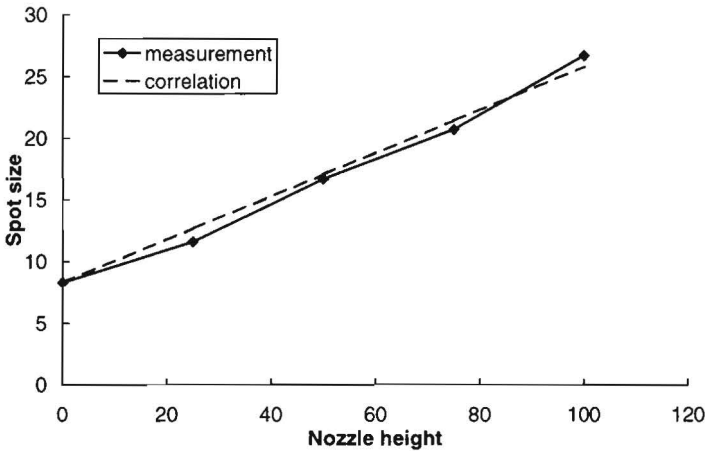
Figure 8-2: The correlation between beam diameter and nozzle height for a 6-mm nozzle [12]. The broken line is the correlation over the three sizes of nozzle.

8.4.2   Velocity correction

One of the important parameters in erosion rate is the particle velocity. Since the particle loading of the abrasive jets is varied considerably, the particle velocity may have differed between experimental situations within one measurement series. Although previous literature [5] claims that the variation in particle velocity caused by different powder fluxes is only limited, we correct our results to allow for this effect to prevent it from influencing the flux effect itself.

We measured a decrease in velocity of up to 3% with a three-fold increase in powder flux. We therefore corrected the measured erosion rates according to

$$E_{corr} = E_{meas} \left(\frac{v_0^*}{v_0} \right)^{7/3} \tag{8.5}$$

171

where the power 7/3 is a commonly found velocity dependence of erosion [8, 9]. For the reference velocity (v_0^*) the velocity at minimum flux is chosen. This is an arbitrary decision that does not influence our results. The choice for a reference velocity does only alter the pre-factor E_r in the fit, while we are interested in the parameter τ (see equation 8.2)

Fitting procedure

For each measurement series the corrected erosion rates were fitted against powder flux with the aid of the model of Anand et al. using a least-squares method. A representative example is given in Figure 8-3. Here τ was found to be 7.19. The results of all the measurement series are presented in Table 8-2.
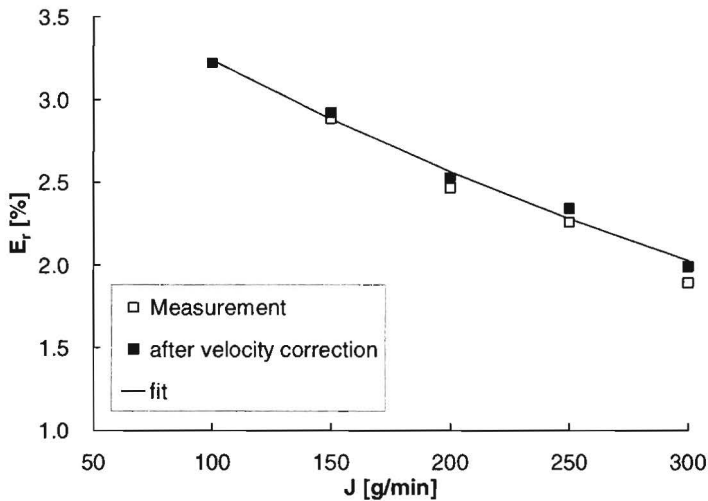
Figure 8-3: An example of the erosion rate fitted against the particle flux graph (6-mm nozzle, h = 75 mm, v= 200 m/s). Note the limited effect of the velocity correction.

8.5 Results and discussion

As Table 8-2 shows, we found the same wide range of values for the fit constant τ as Anand et al. Since the applicability of the model with such a variation in model constant is very limited, we searched for correlation's between the fit parameter τ and any of the process parameters already used in the flux effect model. A strong correlation was found between the coefficient τ and the incoming particle velocity (see Figure 8-4).

The linear fit shown here is given by:

$$\tau = a - bv_0 \tag{8.6}$$

where $a = 20.54$ and $b = 0.066$ s/m with standard deviation of respectively 0.65 and 0.005 s/m.

Table 8-2: The calculated spot sizes and fit coefficients.

Series no	Nozzle diameter (d_0) [mm]	Nozzle height (h) [mm]	Spot diameter (d) [mm]	Particle velocity (v) [m/s]	Fit coefficient τ
1	1.5	40	8.5	127	12.42
2				181	8.610
3				200	7.540
4	6	50	16.7	227	4.535
5		75	21.1	200	7.195
6		100	25.5	177	7.720
7				221	6.135
8	12	85	26.9	260	2.877
9				271	3.160
10		170	41.7	230	5.570

Figure 8-4: The correlation between the fit coefficient τ and the impact velocity v_0.

The other correlation's found were weak and could be attributable to the slight dependency between the measurement series; the experiments with the smaller
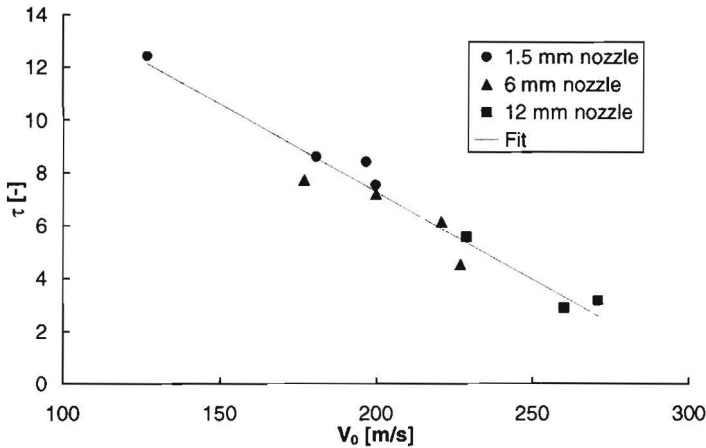
nozzle were performed at lower velocities than the experiments with the larger nozzles.

When the fit parameter is replaced by a two-parameter fit containing the incident particle velocity, the wide scatter in the fit parameter reduces to a workable correlation. It is valuable to investigate a possible physical meaning of the dependence of τ on the particle velocity found statistically,

The velocity dependence of τ suggests that when the particle velocity increased, the particles are removed from the abrasive jet faster than the original model assumes. The expansion of this parameter according to the derivation of Anand et al. might give a clue (equation 8.3)

$$\tau = \frac{L}{d} \frac{v_0}{v_r} \tag{8.7}$$

We distinguished two groups in this relation: the rebound coefficient (v_r/v_0), defined as the ratio between the velocity of the rebounding particles and that of the incoming particles, and a group L/d, which we interpreted as the tangent of the angle of the rebounding particles (see Figure 8-5)

$$\frac{L}{d} = \frac{1}{2} \tan \theta \tag{8.8}$$
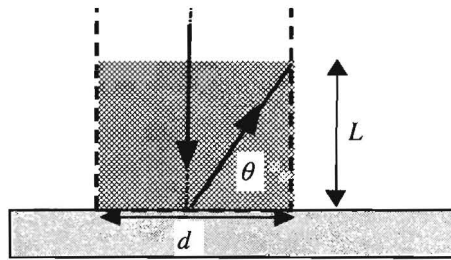
Figure 8-5: The ratio L/d seen as a measure of the angle of rebounding particles.

To investigate the dependence of the rebound coefficient and the rebound angle on the particle velocity we performed some simple rebound experiments. In these experiments we measured the horizontal and vertical components of the particles along a line parallel to the surface through the centre of the beam. From these values the particle velocity and angle along this line for both the incidenting and rebounding particles are calculated. We defined the angle and velocity of the jets at the values of the maximum incident and rebounding velocity, respectively.

The rebound angle at normal impact is difficult to measure in this way. The rebounding jet is widely scattered. To illustrate the tendencies of the rebound parameters we measured them at angles of 60, 75 and 90 degrees. The results are presented in Table 8-3. We have bracketed the rebound angle values at normal impact to indicate the inaccuracy of the measurements.

Table 8-3: Rebound coefficients and angles measured with a 1.5-mm nozzle.

Velocity [m/s]	Measured						"Required" (calculated)
	60 ° incidence		75 ° incidence		90 ° incidence		90° incidence
	v_r/v_0	θ	v_r/v_0	θ	v_r/v_0	θ	θ
	[-]	[°]	[-]	[°]	[-]	[°]	[°]
115	0.14	48	0.12	38	0.19	(73)	78
165	0.09	28	0.08	35	0.17	(70)	73
205	0.07	23	0.06	34	0.17	(75)	67

The data in the Table 8-3 show that v_r/v_0 tends to decrease with increasing velocity. This effect cannot explain the observed correlation of τ, since it predicts the opposite influence. The rebound angle θ also decreases with increasing velocity. The results obtained for normal impact are unreliable but both other angles clearly show this tendency. It is this effect that might cause the decrease in τ with velocity.

We found no confirmation of our measurements in the literature. Hutchings et al. [14] did find different rebound correlation's for steel spheres (10 mm) on metal targets. But since their impact conditions were very different from our small angular particles on brittle substrates, an opposite correlation could very well be possible.

To illustrate the change in rebound angle required accounting for the observed correlation we calculated the angle using equations (8.6) and (8.7). Since the variation at normal impact is small, we used a constant rebound coefficient of 0.18. It shows that a variation of 10 degrees in rebound angle is needed to produce an effect comparable with the observed fit of τ.

So it seems reasonable to conclude that the dependence of the parameter τ is caused by a slight change in rebound angle with increasing velocity. The cause of this is uncertain, but an explanation might be found in the airflow from the nozzle. An increased particle velocity is accompanied by higher air speeds. The rebounding particle that moves at a relatively low velocity (10 to 30 m/s) will experience drag from the airflow. This flow is towards the substrate and near the

substrate outwards of the beam. It is likely to contribute to an early removal of the particle from the incident beam at higher velocities. An increase of just 6 m/s in radial velocity of the rebounding particles is needed to explain the change in rebound angle in Table 8-3. This change seems reasonable at estimated change in radial air speed of over 50 m/s.

Although the extended model works well for our erosion process, it is not possible to generalise the model to other erosion processes. We have found no literature that could be used to validate the model outside our measurement range. Anand et al. presented some values for τ, which confirm the decrease of τ with increasing velocity.

When the parameter τ is a function of the rebound angle and rebound coefficient as suggested above, it is possible that the values found here are not generally applicable. If air drag is indeed the responsible mechanism for the decrease in rebound angle, larger particles will be less influenced and the velocity dependence of the fit parameter may be assumed to be less than that found here. The erosion process may affect both the rebound angle and the rebound coefficient at hand, such as the elasticity of impact.

8.6 Conclusions

For an erosion process of alumina particles on glass substrates we have expanded the flux effect model of Anand et al. to make it suitable for interpolation and extrapolation between different abrasive jet machines over a considerable range of nozzle sizes. This expansion involves the incorporation of a velocity-dependence in the fit parameter τ. We have found evidence that this dependence might originate in a decrease in the rebound angle with an increasing velocity, possibly resulting in early removal of the rebounding particle from the incident beam. This change in rebound angle might be caused by drag from the air jet used to accelerate the abrasive particles.

Although the extended model works well for our erosion process, it is not possible to generalise the model to other erosion processes. For such a model large numbers of experiments are needed for all kind of erosion conditions and an improved model is required for the particle removal from an erosive jet. This paper might be a first step towards a model that includes every erosion process.

8.7   List of symbols

A The collision cross-section of an individual rebounding particle $[m^2]$, Equation 8.1.

C The concentration of rebounding particles $[1/m^3]$, Equation 8.1.

D The diameter of a particles $[m]$, Equation 8.2.

E_{corr} The measured erosion rate corrected for velocity differences [-], Equation 8.5.

E_f The apparent erosion rate including flux effect (mass of removed substrate per mass of used erodent [g/g] or [-]), Equation 8.2.

E_{meas} The measured erosion rate in a flux series [-], Equation 8.5.

E_r The erosion rate at zero flux (mass of removed substrate per mass of used erodent [g/g] or [-]), Equation 8.2.

J The incoming particle flux [kg/s], Equation 8.2.

L Rebound height of rebounding particles $[m]$, Figure 8-1.

a Fit parameter [-], Equation 8.6.

b Fit parameter [s/m], Equation 8.6.

d Diameter of particle jet $[m]$, Figure 8-1.

d_0 Diameter of the nozzle $[m]$, Equation 8.4.

h The sample-nozzle distance $[m]$, Equation 8.4.

v_0 The velocity of incoming particles [m/s], Figure 8-1.

v_0^* The reference velocity for the velocity correction [m/s], Equation 8.5.

v_r The velocity of rebounding particles [m/s], Figure 8-1.

α The velocity rebound coefficient (v_r/v_0) [-], Equation 8.3.

ϕ The divergence angle of a jet [°], Equation 8.4.

θ The rebound angle of rebounding particles [°], Equation 8.8.

ρ The specific mass of the particles $[kg/m^3]$, Equation 8.2.

τ The dimensionless fit coefficient from the model of Anand et al. [7], Equation 8.2.

8.8   Literature

1   H.J. Ligthart, P.J. Slikkerveer, F.H. in 't Veld, P.H.W. Swinkels, M.H. Zonneveld, *Glass and Glass Machining in Zeus Panels*, Philips J. of Res. 50, no 3/4 (1996) 475-499.

2   H. Uuemóis and J. Kleis, *A critical analysis of erosion problems which have been little studied*, Wear 31 (1975) 359-371.

3   G.P. Tilly and W. Sage, *The interaction of particle and material behaviour in erosion processes*, Wear 16 (1970) 447-465.

4   M. Liebhard and A. Levy, *The effect of erodent particle characteristics on the erosion of metals*, Wear 51 (1991) 381-390.

5   P.H. Shipway and I.M. Hutchings, *A method for optimising the particle flux in erosion testing with a gas-blast apparatus*, Wear 174 (1993) 160-175.

6   B. Lindsley, K. Stein and A.R. Marder, *The design of a high-temperature erosion apparatus for studying solid particle impact*, Meas. Sci. Technol. 6 (1995) 1169-1174.

7   K. Anand, S.K. Hovis, H. Conrad, R.O. Scattergood, *Flux effects in solid particle erosion*, Wear 118 (1987) 243-257.

8   I.M. Hutchings, *Transitions, Threshold Effects and Erosion Maps*, J.E. Ritter (ed), *Erosion of Ceramic Materials*, Key Eng. Mat. 21 (1992) 75-92.

9   M. Buijs, *Erosion of glass modelled by indentation theory*, J. Am. Ceram. Soc. 77, no 6 (1994) 1676-1678.

10   S.M. Wiederhorn and B.J. Hockey, *Effect of Material Parameters on the Erosion Resistance of Brittle Materials*, J. Mater. Sci. 18 (1983) 766-780.

11   D.R. Andrews and N. Horsfield, *Particle collisions in the vicinity of an eroding surface*, J. Phys. D: Appl. Phys. 16 (1983) 525-538.

12   J. van Zantvoort, J. Jacobs, R. van As, personal communication (1995).

13   H. Tennekes and J.L. Lumley, *A first course in Turbulence*, P 4.4 *Turbulent jets*, MIT Press, Cambridge (1972).

14   I.M. Hutchings, N.H. Macmillan and D.G. Rickerby, *Further studies of the oblique impact of a hard sphere against a ductile solid*, Int. J. Mech. Sci. 23, no. 11 (1981) 639-646.

9 General discussion and conclusions

This thesis presents a scientific study into the fundamentals of the powder blasting process initiated by a technological need. The work was started to find answers on a number of technological questions mentioned in paragraph 1.3. To keep the discussion clear, this chapter is therefore split into two parts, the first focussing on the fundamental issues of the work and the second part concentrating on the implications for the technological background. The final section presents some reflections on the powder blasting process as an industrial process.

9.1 Fundamental issues

Homogeneous erosion
In the chapters 2 and 3 we derived relations correlating erosion parameters of respectively sharp and spherical particles with erodent and material parameters. Equations were obtained for the boundaries of erosion regimes, process parameters like erosion rate and properties of the substrate surface as a result of the erosion process, i.e. its surface roughness and its reduction in strength.
The relations for the process parameters for sharp particles predict that the influence of the erodent particle is fully determined by its kinetic energy. This has been verified with experimental data for a number of erodent materials. The

predicted relations give a good description of the dependence of erosion and surface roughness on the kinetic energy of the particles.

The equations for spherical particles do predict the impact regimes found experimentally at single particle impact on non-eroded glass. A quantitative comparison with experiments is hindered by the protrusions present on the particles used. For this, new experiments will be required using perfect spherical particles.

The models for process parameters of spherical particles, like rate of material removal and resulting surface roughness, do not come close to the experimental results. It becomes evident that the starting point of the theory, namely that erosion can be seen as a repeated single particle event, does not apply for erosion by spherical particles, although it has been successful for sharp particles.
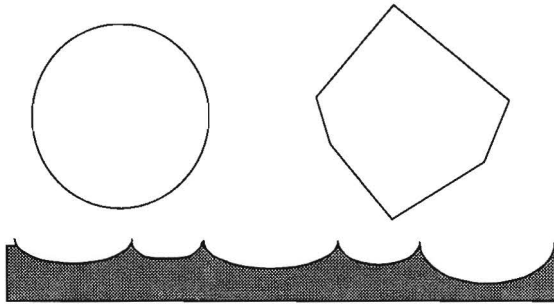

Figure 9-1: Comparing impacts of a spherical and an angular particle on a rough substrate.

A possible explanation is sketched in Figure 9-1. During an erosion process the surface of the target is no longer flat as assumed in the theory. Since sharp particles have a large probability of hitting the surface with a tip and the roughness being considerably smaller than the particle size, the majority of impacts will resemble impacts at a flat surface. A spherical particle most likely hits the tips of the surface roughness, giving a situation where only the far field of the stresses resembles the impact at flat substrates. To include these effects the erosion model for spherical particles requires an approach differing completely from that of sharp particles.

The work on erosion maps suggests that the impact regimes shift gradually when the particle shape changes from spherical to angular. Verification of this transition is of fundamental interest, although it might be difficult to verify experimentally since it would require rounded particles with well-defined tip curvatures. The erosion model for angular particles predicts no influence of particle shape on the material removal rate and should also be valid for spherical particles in the ductile impact regime. Though rejected for spherical particles, possibly because of the

mechanism depicted in Figure 9-1, it can be expected to be valid for particle shapes close to angular particles, e.g. particles with blunted tips.

At oblique impact angles, the erosion rate and resulting surface roughness is well described by the empirical $\sin(\theta)$-rule. Although this relation is found to be of universal value in the literature, no descriptive theory is available supporting this rule.

Patterned erosion
The model for the forming of patterns in glass describes the basic mechanisms for the development of the shapes observed experimentally. The main shape originates from the erosion behaviour of the substrate material at oblique impact, while rebounding particles from the walls of the patterns give additional erosion near the centre of the pattern. Since generally ceramic materials follow the $\sin(\theta)$-rule at oblique impact, the shapes obtained are relatively independent of substrate and process conditions.
Experiments confirm the basic tendencies predicted by the model. However, for a more accurate prediction of especially finer details, a number of effects should be included in the model, for example effects of mask wear and the size-induced hindering of particles in the formed structures and near the mask edges. The description of the particle rebound behaviour certainly needs improvement. This requires new rebound experiments using for example a 2D Laser Doppler Anemometer to be able to distinguish between incoming and rebounding particles.
It would be helpful to develop a mathematical model using a parameterised surface description ($x = x(s,t)$, $z = z(s,t)$) for an improved description of steep walls and enabling the description of overhangs.

The mask erosion model shows the dependence of rubber erosion at oblique impact to be also the primary factor describing the wear of mask patterns. For polymer material no model is available that describes the erosive wear quantitatively from primary material parameters. The materials tested show a considerable difference in erosion as a function of impact angle, where the erosion at normal impact does not correlate with the oblique erosion behaviour. Since the erosion model predicts the erosion at glancing impact to dominate mask wear, which is confirmed experimentally, a classification of materials for powder blasting masks should be performed at low impact angles (for example 15°).

Powder degradation and interaction
The alumina abrasive used in this research exhibits a considerable degradation at initial use, which can be attributed to damage from the production process of the powder still present in the particles. This damage is being removed by fracture of

the particles in the first few times of use, creating stronger and dimensionally more stable powders that can be reused many times in a powder blast process.

Interaction between impinging particles and rebounding particles lead to the so-called flux effect, which may strongly reduce the effectiveness of the incoming abrasive particles. A study of the effect revealed a correlation that can be used to predict the flux effect as function of for example abrasive beam size, particle velocity and powder flux. It shows that for larger nozzle sizes operating at high powder flux, the efficiency reduction can be dramatic giving powder efficiencies lower than 10%.

9.2 Technological implications

The research presented in this thesis was initiated by the technological need of a high accuracy process for the mass production of perforated glass sheets to be used in a novel flat display. To assist this development three fundamental questions were formulated in section 1.3. Here we present answers to these questions based on the results presented in this thesis and the experience gained by performing the work.

1. What are the parameters controlling the process (e.g. the processing speed) and its results (e.g. the surface structure and the shape of the patterns)?

⇨ *The basic process (homogeneous erosion)*
The erosion process is controlled by the amount of particles hitting an area of the substrate and the kinetic energy of those particles. The type of abrasive used, its size and its velocity have no independent effect. The shape of the abrasive particles is not of influence. Although this would include spherical particles, which was not confirmed experimentally, the conclusion is expected to hold for the sharp and rounded particles used in practice.

The efficiency of material removal is only a weak function of the kinetic energy of the particles. Although the material removal is slightly more efficient at higher kinetic energies, the larger chips removed from the substrate will generate a considerable higher surface roughness. In many practical situations the desired surface roughness will prescribe the kinetic energy at which the process should operate.

The resulting surface roughness might also be used as a rough process control parameter giving a first indication of the kinetic energy at which the erosion process operated to produce the sample measured.

The dependence on kinetic energy only, means that a powder blasting process can be operated with any hard, angular abrasive powder of any size, as long as the particle velocity is well chosen.

⇨ *Shapes*
The erosion model and experiments show that the shape of the formed structures is, in a first approximation independent of substrate material and process conditions like particle size and particle velocity. With the jet perpendicular to the substrate all patterns have the same shape at an equal depth over width ratio. The process is thus in a first approximation independent of process conditions, where the mask geometry and the amount of erosion define the shapes obtained. This is both an advantage and a disadvantage of the process, depending whether the shape obtained is the one that is desired.
A closer look reveals a number of refinements to the conclusion above. For example, particle size effects can be found to round off details of finer patterns, and the contribution of rebounding particles may be dependent on impact velocity.

⇨ *Substrate material*
Since the obtained shape of the geometry depends mainly on the dependence of erosion on impact angle and since this dependence is constant for most brittle materials, the shape obtained by erosion is independent of the substrate material. As long as the abrasive powder is harder than the substrate the process will follow the basic mechanism described in this thesis. The dependence of material removal rate (cm^3/Joule) on substrate properties is limited; most glasses differ less than a factor 1.5 of the results presented here. Only for very hard materials like alumina eroded with silicon carbide the material removal rate changes significantly. The insensitivity of the powder blasting process with respect to substrate material makes the process very versatile to apply.

⇨ *Process control*
Controlling the results of a powder blasting process requires controlling a number of process parameters listed below.
- **The mask.** Considering the importance of the mask for the final result, it is not only required to control the dimensions of the initial mask, but the mask material should also display either a negligible wear or a reproducible amount of wear. In the latter case a good control of mask material and processing is required.
- **The abrasive**. A constant powder size distribution is required. Interestingly in an industrial powder-blasting machine that recycles the powder, reused powder fulfils this demand better than original powder. For process control a regular

monitoring of the particle size should be performed to enable a gradual supplement of worn or lost powder.

- **The powder flux**. The main task of the powder-blasting machine is distributing an amount of powder at constant velocity evenly over the substrate surface. It is therefore needed to monitor the powder flow through the nozzles at a regular basis. Besides this the mechanisms that supply the relative movement between nozzle and substrate need to be checked at intervals.

- **The particle velocity**. The particle velocity is not only an important parameter for controlling the process, it is also the most suitable parameter to select the erosion regime. For process control it is usually sufficient to monitor closely the air pressure supplied to the nozzle or the airflow through the nozzle. Measuring the surface roughness of eroded surfaces can provide a rough selection of the erosion regime. A careful selection requires the preparation of an air pressure /airflow against velocity calibration curve.

2. *What are the essential process costs and what can be done to decrease those (e.g. machine, abrasive)?*

Since the accuracy of the patterns is predominantly defined by the mask pattern applied to the substrate, the powder-blasting machine suffices with a far larger inaccuracy than the actual patterns, giving a relative inexpensive machine. It should, however, permit the process control mentioned above.

In powder blasting large quantities of abrasive powder are used (an erosion rate of 1% translates to 100 kg powder per 1 kg material removed or in the order of 10 cm powder per mm substrate thickness). Although these powders are not very expensive, recycling is required. The alumina powder used in this thesis shows initially a considerable degradation, which decreased considerably in the first few times of reuse. Since this degradation originates from damage inflicted during the manufacturing process of the powders, which is removed during the same degradation, the reused powders have been found strong enough to allow reuse for hundreds of times.

3. *What scaling rules for the process should be used when scaling up from a small laboratory set-up to full mass production?*

When maintaining control over the process parameters mentioned above, scaling up could be performed almost straightforward by supplying more powder over larger surfaces. It is essential, though, to consider the flux effect in doing so. Since it takes longer to remove the particles after impact from the jet for larger size nozzles, a step to larger round nozzles might give a dramatic decrease in process

efficiency by this flux effect. Giving large nozzles a strongly elongated shape (line shape) can decrease the flux effect by minimising the distance a rebounding particle needs to travel to exit from the jet.

9.3 Reflections on powder blasting as an industrial process

Initiated by manufacturing issues of a new display concept (the Zeus display) the powder blasting process of glass has been developed into a high-accuracy industrial etching process. It is capable of patterning large surfaces at high precision and high process speeds. The powder blast machine itself can be relatively low-tech, but it might be bulky by the size of the powder recycling equipment. For etching fine structures photolithography equipment is required for making the masks.

A point of concern must be the potential health hazard formed by dust generated in the process. With appropriate containment measures the dust can be prevented from causing respiratory problems and skin irritation.

Although the Zeus display concept was abandoned in 1996 for commercial reasons, powder blasting has proved itself over the years in many other applications. It was found to be a flexible abrasive process delivering high accuracy for details larger than 100 µm in a wide range of substrate materials. Its specific process properties have enabled making products that can not be made with other processes. These properties make the process a valuable extension of processes available for brittle materials, worthy a position in many a workshop.

Dankwoord

Technologische en wetenschappelijke resultaten zijn zelden het resultaat van de inspanning van een enkel persoon. De resultaten in dit proefschrift zijn daarop geen uitzondering. Zij zijn het resultaat van het werk van een breed team van personen dat zich heeft ingezet om iets te maken van het Zeus-display en van het poederstraalproces op zich. Ik beschouw daarom dit proefschrift als de kroon op het werk van alle betrokkenen. Ik wil hen hierbij enorm bedanken, hopende dat er nog een grotere kroon op het werk gezet zal worden, wanneer het poederstraalproces een brede toepassing vindt in de abrasieve bewerking van brosse materialen.

Een aantal personen verdienen speciale vermelding. Allereerst wil ik Henri in 't Veld bedanken voor zijn grote inzet en de positieve instelling waarmee hij het merendeel van de experimenten heeft opgezet. Mijn naaste collegae in het cluster "Breukmechanica" wil ik bedanken voor de vele discussies en de assistentie, onder andere bestaande uit het corrigeren van de verschillende publicaties. Speciaal ben ik dank verschuldigd aan Piet Bouten voor de goede samenwerking gedurende de afgelopen jaren en aan Bert de With voor de fundamentele discussies, eerst als collega en later als promotor. Alle collegae in de NatLab-diensten wil ik bedanken voor hun assistentie. In het bijzonder dank ik Jan van Laarhoven en Frans de Haas voor het onderhoud van de machines, alle experimenten die zij hebben uitgevoerd en hun rotsvaste geloof in poederstralen als proces. Mariette Geltink-Verspui, Erik Skerka, Ingrid Oomen en Martijn van Dongen hebben respectievelijk als aio, afstudeerder, stagiair en WGP-er significante bijdragen geleverd net als de overige co-auteurs van de artikelen opgenomen in dit proefschrift: Fred Touwslager en Derk Reefman, waarvoor ik hen zeer erkentelijk ben.

Promoveren heeft naast de technologische ook een sociale kant. De grote steun die ik van allerlei kanten mocht ervaren was hierbij hartverwarmend, zowel van het NatLab management als van (oudere) collegae op het NatLab en van familie, buren, vrienden en bekenden. In het bijzonder wil ik mijn zus Anja en zwager Rein bedanken voor de "begeleiding" en hun inzet bij de correctie van de opmaak en drukproef.

Curriculum Vitae

Peter Jan Slikkerveer is geboren op 19 maart 1962 in Brielle. In 1980 behaalde hij het diploma Atheneum B aan de Rijksscholengemeenschap aldaar. Aansluitend begon hij de studie Werktuigbouwkunde aan de Technische Universiteit Delft. In 1987 rondde hij de verlengde (6-jarige) studie af aan de vakgroep Stromingsleer en trad als onderzoeker in dienst bij het Philips Natuurkundig Laboratorium. Na actief te zijn geweest op een aantal andere vakgebieden, nam hij van 1994 tot 1997 deel aan een project ter ontwikkeling van het poederstraalproces tot een precisie-bewerkingstechniek. Hij was verantwoordelijk voor de wetenschappelijke ondersteuning en onderbouwing van het project. De resultaten van dit werk worden in dit proefschrift beschreven.

Peter Jan Slikkerveer was born on March 19th, 1962 in Brielle. In 1980 he obtained his diploma Atheneum B at the Rijksscholengemeenschap in Brielle. He started the studies Mechanical Engineering at Delft University of Technology. In 1987 he completed the extended program (6 years) at the department of Fluid Mechanics and joined the Philips Research Laboratories in Eindhoven. After working in a number of other fields he participated from 1994 to 1997 in a project to develop the powder blast process into a precision manufacturing technology. He was responsible for the scientific support of this project. The results of this work are presented in this thesis.

List of publications

M.A. Verspui, P. van der Velden, G. de With, P.J. Slikkerveer, *Angularity determination of abrasive powders*, Wear 199 (1996) 122-126.

H.J. Ligthart, P.J. Slikkerveer, F.H. in 't Veld, P.H.W. Swinkels, M.H. Zonneveld, *Glass and glass machining in Zeus panels*, Philips J. Res. 50 (1996) 475-499.

M.A. Verspui, P.J. Slikkerveer, G.J.E. Skerka, I. Oomen, G. de With, *Validation of the erosion map for spherical particle impacts on glass*, Wear 215 (1998) 77-82.

F.H. in 't Veld, P.J. Slikkerveer, *Towards prediction of flux effects in powder blasting nozzles*, Wear 215 (1998) 131-136.

P.J. Slikkerveer, P.C.P. Bouten, F.H. in 't Veld, H. Scholten, *Erosion and damage by sharp particles*, Wear 217 (1998) 237-250.

P.J. Slikkerveer, F.H. in 't Veld, *Model for patterned erosion*, ICEAW conference, Cambridge September 1998, accepted to Wear (1998).

M.A. Verspui, G. de With, A. Corbijn, P.J. Slikkerveer, *Simulation model for the erosion of brittle materials*, ICEAW conference, Cambridge, September 1998, accepted to Wear (1998).

P.J. Slikkerveer, M.H.A. van Dongen and F. Touwslager, *Erosion of elastomeric protective coatings*, accepted to Wear (1999).

P.J. Slikkerveer, M.A. Verspui, G.J.E. Skerka, *Erosion and damage by hard spherical particles on glass*, accepted by the Journal of the American Ceramic Society (1999).

P.J. Slikkerveer, F.H. in 't Veld, M.A. Verspui, G. de With, D. Reefman, *Alumina particle degradation during solid particle impact on glass*, submitted to the Journal of the American Ceramic Society (1999).

P.J. Slikkerveer, J.H.M. ten Thije Boonkkamp, *Mathematical modeling of erosion by powder blasting*, submitted to Surveys on Mathematics for Industry (1999).

P.J. Slikkerveer, P.C.P. Bouten, F.C.M. de Haas, *High quality mechanical etching of brittle materials by powder blasting*, Eurosensors XIII conference, Den Haag, September 1999.

Stellingen behorende bij het proefschrift

Mechanical etching of glass by powder blasting

van

Peter Jan Slikkerveer

0. De invloed van scherpe harde deeltjes in erosieprocessen is beperkt tot hun kinetische energie.
   Dit proefschrift, hoofdstuk 2.

1. De hoekafhankelijkheid van erosie is de dominante factor voor de vorm van geërodeerde profielen.
   Dit proefschrift, hoofdstuk 5.

2. Rubberachtige maskermaterialen dienen onder scherende inval gekarakteriseerd te worden op hun bestendigheid tegen erosie.
   Dit proefschrift hoofdstuk 6.

3. De richting van de corioliskracht ten gevolge van de rotatie van de aarde heeft geen invloed op het poederstraalproces.
   Dit proefschrift, appendix C hoofdstuk 2.

4. Met juist aangebrachte beschermlagen scheppen zandstormen een sfinx.

5. Het oplossen van fysische problemen per computer leidt tot een toename van het aantal op te lossen problemen.

6. Numerieke simulatie van industriële processen moet gehanteerd worden als een experimentele techniek.

7. Het is efficiënter een proefschrift op te bouwen uit publicaties dan publicaties uit een proefschrift te destilleren.

8. "Schipper naast God" krijgt een meer aardse betekenis in het zeezeilen met de toenemende afhankelijkheid van elektronische apparatuur.

9. Vuil beweegt zich naar die plaatsen waar het zich het lastigst laat verwijderen.

10. Technologisch succes vereist een (on)geduldige onderzoeker.

11. De houdbaarheid van deskundigheid gelijkt die van een appel.

12. Ook in het poederstraalproces leidt een grote mond tot een verminderd resultaat.
    Dit proefschrift, hoofdstuk 8.